CARBON DEPOSITION DURING CO-ELECTROLYSIS IN REVERSIBLE SOLID OXIDE CELLS

By

ABIGAIL LOUISE SNOWDON

A Thesis submitted to
the University of Birmingham
for the degree of
DOCTOR OF PHILOSOPHY



Centre for Fuel Cells and Hydrogen Research
School of Chemical Engineering
College of Engineering and Physical Sciences
University of Birmingham
October 2022

UNIVERSITY OF
BIRMINGHAM

University of Birmingham Research Archive

e-theses repository

This unpublished thesis/dissertation is copyright of the author and/or third parties. The intellectual property rights of the author or third parties in respect of this work are as defined by The Copyright Designs and Patents Act 1988 or as modified by any successor legislation.

Any use made of information contained in this thesis/dissertation must be in accordance with that legislation and must be properly acknowledged. Further distribution or reproduction in any format is prohibited without the permission of the copyright holder.

Abstract

Syngas production via high temperature co-electrolysis of CO_2 and H_2O is a promising pathway towards sustainable hydrocarbon fuels in a closed-loop cycle. However, the use of carbonaceous fuels in solid oxide cells (SOC) can lead to carbon deposition at the fuel electrode, particularly at the intermediate-temperature range.

One method for mitigating carbon deposition is changing the fuel electrode material away from the conventional Ni-Yttria Stabilised Zirconia (NiYSZ). Here, the benefits of Ni-Ceria-doped Scandia-Stabilised Zirconia (NiScCeSZ) SOCs are shown in terms of the superior performance at reduced temperatures and carbon resistance. Two methods of cell manufacturing are developed, both adopting the reverse aqueous tape casting technique. One method consists of a novel five-layer cell in which the GDC barrier layer and new composite layer are tape cast and sintered together. The other method incorporates a spin-coated GDC barrier layer onto a pre-sintered half cell. The cells and the properties of the starting materials are characterised by dilatometry, electron microscopy, and the performance is assessed by polarisation curves and electrochemical impedance spectroscopy (EIS). The best performance is achieved from the spin-coated cells due to a reduced ohmic and gas diffusion resistance resulting from thinner layers with less porosity. These spin-coated cells are therefore used for further co-electrolysis and carbon deposition testing.

For the first time, NiScCeSZ fuel electrode supported cells are used for the co-electrolysis

reaction to identify carbon deposition thresholds with respect to operating temperature. Identical tests are also carried out on Ni-YSZ cells for comparison. This work reveals that NiSceSZ cells can operate at up to 58% higher current densities than NiYSZ cells, with half the amount of carbon being deposited. It is important to identify these carbon deposition thresholds in order to operate within the window of safe operation to maximise syngas yield and extend the lifetime of the cells.

Acknowledgements

This PhD is a culmination of four and a half years of research, which would not have been possible without the help and support of friends, colleagues, mentors and supervisors.

A huge thank you must go to my supervisors, Prof. Robert Steinberger-Wilckens, and Dr. Artur Majewski for their support and guidance throughout the course of this research.

From the Fuel Cell group, thank you to John Hooper and Dr. Ahmad El-Kharouf for always being there to offer calm words of encouragement.

Thank you to Chyntol and Manzo for their help in fixing many things in the lab. Thank you to the whole fuel cell group, G05 and G06, we were all in it together. Special mention to Alan, Ollie and Pete for becoming brothers to me from the start. Thanks for all the memories. Thanks to Laura, Liam and Bea for making sure there were good times thrown in with the daily grind. Thank you to the whole of G06 lab, but especially Zeyu, who understands the blood, sweat and tears that go into making the perfect tape, Chris, for being the XRD hero I needed when COVID struck, Manzo and Kun for the lab support, Lois and Oujen for helping me find my feet in the early days, and Mel for the endless supply of cakes and for always making me laugh, thank you.

Thank you to Bob, without whom my cell holder of dreams would not be a thing of reality. Also thank you to Steve from Physics who did an excellent job of replicating it when I had enough sway in the lab to get two rigs on the go. Thank you to Theresa from Metallurgy and Materials for her SEM and TEM expertise.

Thank you to my examiners and chair for their time and input.

Thank you to the Engineering and Physical Sciences Research Council (EPSRC) for the financial support, without which, this research would not have been possible.

And most importantly, thank you to Rich, for your unwavering patience and belief in me. Let the adventures begin.

Contents

Abstract i

Acknowledgements iii

List of Figures vii

List of Tables xii

Abbreviations xv

1 INTRODUCTION 1
- 1.1 Background . . . 1
- 1.2 Power-to-Gas . . . 3
- 1.3 Fuel Cells . . . 4
  - 1.3.1 Solid Oxide Fuel Cells . . . 5
    - 1.3.1.1 Anode . . . 8
    - 1.3.1.2 Electrolyte . . . 9
    - 1.3.1.3 Cathode . . . 9
- 1.4 Electrolysis . . . 9
  - 1.4.1 Solid Oxide Electrolysis (SOE) . . . 11
- 1.5 Reversible Solid Oxide Cells . . . 14
- 1.6 Thermodynamics . . . 15
  - 1.6.1 Nernst Potential . . . 16
  - 1.6.2 Overpotentials . . . 17
  - 1.6.3 Polarisation Curve . . . 18
- 1.7 Fuel Flexibility . . . 19
- 1.8 Motivations . . . 20
- 1.9 Aims of the thesis . . . 21
- 1.10 Thesis Overview . . . 21

2 LITERATURE REVIEW 24
- 2.1 Manufacturing of cells: Tape Casting . . . 24
  - 2.1.1 Starting materials . . . 26
  - 2.1.2 Sacrificial Pore Formers . . . 30

2.1.3 Drying Without Defects . . . 32
2.2 Degradation in SOFCs and SOEs . . . 33
2.2.1 Deactivation of the Fuel Electrode . . . 33
2.2.1.1 Sulphur Poisoning . . . 34
2.2.1.2 Silicon Poisoning . . . 35
2.2.1.3 Chromium Poisoning . . . 36
2.2.2 Delamination of the Oxygen Electrode . . . 36
2.2.3 Redox Stability . . . 38
2.2.4 Material Transport Mechanisms . . . 39
2.2.5 Carbon Deposition . . . 41
2.3 Co-electrolysis in Solid Oxide Cells . . . 47
2.3.1 Brief history of co-electrolysis . . . 48
2.3.2 Carbon formation in co-electrolysis . . . 49
2.4 Power-to-Gas Projects using SOCs . . . 50
2.5 The First rSOCs . . . 53
2.5.1 Degradation in rSOC . . . 55
2.5.1.1 Current Cycling . . . 56
2.5.1.2 Fuel electrode degradation in rSOC . . . 57
2.6 Summary . . . 58

3 METHODOLOGY 60
3.1 Material Characterisation . . . 60
3.1.1 Particle Size Analysis . . . 60
3.1.2 Dilatometry . . . 61
3.2 Reverse Aqueous Tape Casting . . . 62
3.2.1 Slurry Preparation . . . 63
3.2.1.1 Electrolyte and Barrier Layer . . . 63
3.2.1.2 Fuel Electrode Functional Layer and Support . . . 64
3.2.2 Spin Coating GDC . . . 65
3.2.3 Half Cell Assembly . . . 66
3.2.4 Oxygen Electrode Ink Preparation . . . 67
3.3 Test Rig Set Up . . . 67
3.4 Characterisation . . . 71
3.4.1 Electrochemical testing . . . 71
3.4.2 Electrochemical Impedance Spectroscopy (EIS) . . . 72
3.4.2.1 Distribution of Relaxation Times (DRT) . . . 75
3.4.3 Scanning Electron Microscopy (SEM) . . . 77
3.4.4 X-Ray Diffraction (XRD) . . . 77
3.4.5 Temperature Programmed Oxidation (TPO) . . . 78

4 CELL MANUFACTURING **79**
4.1 Tape Casting Method . . . 80
4.1.1 Thermal Expansion Coefficient . . . 80
4.1.2 Effect of layer thickness . . . 82
4.1.2.1 Cell 101010 . . . 83
4.1.2.2 Cell 111 . . . 84
4.1.2.3 Cell 333 . . . 85
4.1.2.4 Cell 214 . . . 86
4.1.3 Effect of Sintering . . . 88
4.1.3.1 Electrolyte . . . 89
4.1.3.2 Fuel Electrode . . . 91
4.1.3.3 GDC Barrier Layer . . . 93
4.2 Spin Coating Method . . . 95
4.2.1 Effect of RPM . . . 96
4.3 Comparison of composite and spin coated cells . . . 97
4.4 Electrochemical characterisation of NiSSZ cells in fuel cell mode and electrolyser mode . . . 100
4.4.1 Beginning of Life (BoL) Cells . . . 101
4.4.2 Fuel Cell Testing . . . 102
4.4.3 Reversible Solid Oxide Cell Testing . . . 104
4.4.3.1 Effect of fuel composition . . . 104
4.4.3.2 Effect of operating potential . . . 108
4.5 Summary . . . 109

5 THERMODYNAMIC EQUILIBRIUM ANALYSIS **112**
5.1 Thermodynamics of high temperature co-electrolysis . . . 112
5.2 Chemical Equilibrium Analysis . . . 116
5.2.1 The effect of temperature change . . . 117
5.2.2 The effect of fuel inlet composition change on carbon formation . . . 119
5.3 Effect of current density on carbon deposition . . . 121
5.4 Summary . . . 123

6 CARBON DEPOSITION IN CO-ELECTROYLSIS **125**
6.1 Carbon deposition during CO_2 electrolysis . . . 126
6.1.1 Thermodynamics of carbon deposition . . . 127
6.1.2 Carbon deposition and EIS . . . 128
6.1.3 Effect of carbon on EIS spectra in co-electrolysis . . . 130
6.2 Identification of carbon deposition threshold . . . 134
6.2.1 Calculation of pCO at the outlet . . . 134
6.2.2 Comparison of theoretical and experimental carbon deposition threshold 135
6.3 Characterisation of carbon deposits . . . 139
6.3.1 Effect of temperature on amount of deposited carbon . . . 139
6.3.2 Effect of temperature on type of deposited carbon . . . 142

6.3.2.1 SEM images of carbon formed at different temperatures . . . 144
6.4 Summary . . . 148

7 CONCLUSIONS **150**
7.1 Further Work . . . 154

Appendix A Characterisation of Starting Materials **155**
A.1 Microscopy . . . 155

Appendix B Carbon Deposition Threshold Graphs **157**

Appendix C Author Contribution to Chapter Four **159**

List of Figures

Figure 1.1 Global greenhouse gas emissions per type of gas [1]. 1
Figure 1.2 Schematic diagram of a planar SOFC showing the movement of ions and electrons. 7
Figure 1.3 Schematic of an anode supported microtubular SOFC [14]. 7
Figure 1.4 Schematic diagram of the TPB reaction sites at the fuel-electrolyte interface of a NiYSZ cell with hydrogen fuel. TPB sites are identified in orange. . 8
Figure 1.5 Schematic diagram of an SOE showing the movement of ions and electrons. 11
Figure 1.6 Electrical energy input (ΔG) and total energy (ΔH) for the electrolysis of water as a function of temperature [17]. 12
Figure 1.7 Operating modes of high-temperature SOC [18]. 13
Figure 1.8 A typical polarisation curve for a fuel cell showing losses, Nernst voltage and actual cell voltage. 18

Figure 2.1 Schematic diagram of the basic principle of tape casting, using doctor blade and carrier film [35]. 25
Figure 2.2 Effects of (a) 4% PVB, (b) 10% PVB, and (c) 6% PVB on green tape [37]. 27
Figure 2.3 Stress-Strain properties of binder with and without Type I and Type II plasticisers [35]. 28
Figure 2.4 Elongation-tensilestrength curves of green tapes with different plasticisers [46]. 29
Figure 2.5 Schematic diagram of how pore formers introduce porosity to electrodes [52]. 30
Figure 2.6 Polarisation curve of Ni-YSZ ASC made with varying amount of pore former: 1.5 wt%, 2 wt%, 2.5 wt%, 3.5 wt% and 3 wt% [53]. Cells are named with the amount of pore former used. 31
Figure 2.7 SEM micrograph of extensive delamination along the electrode-elecrolyte boundary [77]. 37
Figure 2.8 EDX mapping of Zr, Ni and Ce after (a) 2,500 h, (b) 15,000 h and (c) 20,000 h of operation showing Ni depletion [100]. 40
Figure 2.9 Carbon deposition limits in the C-H-O ternary diagram [108] 43
Figure 2.10 XRD patterns of (a) 10Sc1CeSZ and (b) 10ScSZ [40]. 45
Figure 2.11 SEM micrograph of the interface between a Ni particle and the YSZ electrolyte, where filamentous carbon has formed [124]. 46

Figure 2.12 Comparison of different i-V curves for co-electrolysis, CO_2 and H_2O electrolysis [134]. 48
Figure 2.13 The trend of published work on rSOC over the past 20 years from the Scopus database. 54

Figure 3.1 Representation of a typical tape casting set up [52]. 63
Figure 3.2 The tape casting manufacturing process of fuel electrode supported SOC. 63
Figure 3.3 Sintering profile for half cells. 66
Figure 3.4 Test rig set-up showing all electrical and gas control components. 68
Figure 3.5 Schematic diagram of the cell holder. 70
Figure 3.6 Nyquist plot and equivalent RC circuit element 73
Figure 3.7 Impedance spectrum for an ASC showing the different processes occurring at the fuel electrode (red) and the oxygen electrode (blue) [189]. 74
Figure 3.8 Equivalent circuit model used for CNLS fitting of Ni-SSZ and Ni-YSz cell impedance. 75
Figure 3.9 The Nyquist plot and DRT of a fuel electrode supported cell showing how the DRT identifies the different processes occurring at the oxygen electrode (blue) and fuel electrode (red) [189]. 76

Figure 4.1 GDC layer delaminating from the electrolyte after sintering for 4 hours at 1400 ºC. 81
Figure 4.2 EDX element line scans of the cross section from (a) traditional NiYSZ cell and from (b) a new 5 layer cell. 82
Figure 4.3 SEM micrographs of composite layer for cross-section of Cell 101010. . 83
Figure 4.4 SEM micrographs of composite layer for cross-section of Cell 111. . . . 84
Figure 4.5 SEM micrographs of a composite layer from the cross-section of Cell 333. 85
Figure 4.6 SEM micrographs of composite layer for cross-section of Cell 214. . . . 86
Figure 4.7 Thermal expansion information of YSZ, SSZ and GDC pellets between 20ºC and 1400ºC. 88
Figure 4.8 SEM micrographs of ScCeSZ pellets sintered at (a) 1300ºC, (b) 1350ºC and (c) 1400ºC for four hours. 89
Figure 4.9 XRD spectra of ScCeSZ samples sintered between 1100ºC and 1400ºC for four hours. β indicates the rhombohedral phase and c indicates the cubic phase. 90
Figure 4.10 SEM micrographs of the GDC surface after sintering for 4 hours at (a) 1300ºC (b) 1350ºC and (c) 1400ºC. 94
Figure 4.11 SEM micrographs of the cross section of a half cell after applying spin coated GDC at (a) 1200 rpm, (b) 1700 rpm, and (c) 2500 rpm. 97
Figure 4.12 Polarisation curves of Ni-SSZ cells made via the composite tape casting method (grey) and the spin coated method (red) from 600ºC to 800ºC. 98
Figure 4.13 Impedance plots of NiSSZ cells made via the composite tape casting method (grey) and the spin coated method (red) at 800ºC. 99

Figure 4.14 NiSSZ full cell (a) before reduction and (b) after reduction, at BoL before electrochemical testing. 101
Figure 4.15 (a) i-V curve and (b) EIS spectra for cells made in-house (NiYSZ and NiSSZ) compared to commercial NiYSZ cells. Frequency has been labelled on the impedance plot. 102
Figure 4.16 DRT analysis showing changing internal processes when operating at different temperatures and different O_2 partical pressure. 103
Figure 4.17 Performance (i-V and EIS) of NiSSZ cells operating as rSOCs in a 0.25/0.75 H_2O/H_2 fuel mix with air on the oxygen electrode from 800ºC to 600ºC. 104
Figure 4.18 (a) DRT taken at OCV during electrolysis of 25% H_2O in H_2, and (b) a repeat of Figure 4.16 (a), with the DRT taken at OCV for the same type of cell in fuel cell mode. 105
Figure 4.19 Co-electrolysis polarisation curves taken between 0.4 V and 1.6 V at 600ºC, 700ºC and 800ºC for NiSSZ cells with a fuel mix of 25% H_2O, 25% CO_2, 25% H_2 and 25% CO. 106
Figure 4.20 Comparison of i-V curves for NiSSZ and NiYSZ cells fuelled by 25% H_2O, 25% CO_2, 25% H_2 and 25% CO. 107
Figure 4.21 Impedance and corresponding DRT taken at 800ºC at three different potentials: 0V (OCV), 0.7V (fuel cell mode), and 1.3V (co-electrolysis) for cells fuelled by 25% H_2O, 25% CO_2, 25% H_2 and 25% CO. 108

Figure 5.1 Relationships between enthalpy change (ΔH), entropy change (ΔS) and Gibbs free energy change (ΔG) of H_2O, CO_2 and co-electrolysis reactions. . . . 114
Figure 5.2 Gibbs Free Energies for the reactions taking place during co-electrolysis. 116
Figure 5.3 Effect of temperature change on gas equilibrium composition of a gas feed composition of 25% CO_2, 25% H_2O, 25% CO and 25% H_2. 118
Figure 5.4 Effect of changing the fuel inlet composition on the amount of carbon formed. 119
Figure 5.5 C-H-O ternary diagram with carbon deposition thresholds at different temperatures and the co-electrolysis gas composition region. The asterisk indicates the gas composition used in this study (25% H_2O, 25% CO_2, 25% H_2 and 25% CO). 120
Figure 5.6 C-H-O ternary diagram showing the co-electrolysis gas composition region and the markers for 50:50 H_2:CO and 50:50 H_2O:CO_2. The grey regions indicate the carbon deposition region at 800°C. 121
Figure 5.7 The H = 1 vertex of the C-H-O ternary diagram with carbon deposition thresholds at 600°C and 800°C shown. The fuel utilisation for co-electrolysis is superimposed in red. 122

Figure 6.1 Calculated Nernst potential for the CO_2 electrolysis reaction and two electrochemical carbon deposition reactions. The overpotential for the Boudouard reaction and electrochemical carbon deposition reactions are shown on the second y-axis. 127
Figure 6.2 CO_2 electrolysis galvanostatic cell test at 700ºC with 0.50/0.50 pCO2/pCO fuel mix used to identify the carbon deposition threshold. The current was increased in 10 mA steps and held for 90 minutes at each step. 129
Figure 6.3 (a) Impedance and (b) corresponding DRT spectra, taken at OCV before and after polarisation curve for CO_2 electrolysis at 700ºC. 130
Figure 6.4 (a) EIS taken at OCV and (b) corresponding DRT for NiSSZ cell at 800ºC. 131
Figure 6.5 (a) EIS taken at OCV and (b) corresponding DRT for NiYSZ cell at 800ºC. 132
Figure 6.6 Comparison of DRT spectra of NiSSZ and NiYSZ cells after co-electrolysis tests, taken at OCV at 800ºC. 133
Figure 6.7 Cell tests investigating the carbon deposition threshold at 800ºC for NiYSZ cells. The voltage becomes unstable at 1.3 V as seen in (a) and (b). Theoretical carbon deposition threshold from section 6.1.1 and experimental carbon deposition threshold have been superimposed onto (b). 136
Figure 6.8 The calculated pCO corresponding to carbon deposition for NiSSZ and NiYSZ cells operated between 800ºC and 600ºC as a function of current density. 137
Figure 6.9 Cell test showing how carbon formation causes initial increase in performance (from -0.3 Acm^2) before detrimental effect (from -0.6 Acm^2). 138
Figure 6.10 TPO peaks for (a) the three carbon black calibration standards, and (b) graphite. 139
Figure 6.11 Quantified carbon deposits from NiSSZ and NiYSZ cells tested in co-electrolysis mode between 600°C and 800°C. 140
Figure 6.12 CO_2 peaks from TPO analysis of the NiSSZ cells. 142
Figure 6.13 TPO profile from NiYSZ cells. 143
Figure 6.14 SEM images of NiSSZ cells showing different types of carbon that was deposited at operating temperatures of (a) 800ºC, (b) 700ºC, and (c) 600ºC. . . 145
Figure 6.15 SEM images of NiYSZ cells showing different types of carbon that were deposited at operating temperatures of (a) 800ºC, (b) 700ºC, and (c) 600ºC. . . 145
Figure 6.16 Locations of EDX spectra. 146
Figure 6.17 SEM images of NiYSZ cells showing different stages of carbon deposition due to operating temperature. (a) shows a BoL fuel electrode to compare to the fuel electrode of cells after co-electrolysis tests at (b) 800ºC, (c) 700ºC and (d) 600ºC. 147

Figure A.1 NiO TEM micrographs 155
Figure A.2 Tapioca starch pore former imaged by (a) TEM, and (b) SEM. 155

Figure A.3 TEM and SEM images of 10Sc1CeSZ powder from DAIICHI KIGENSO KAGAKU KOGYO CO., Ltd. (DKKK) showing (a) particles of size 0.1 μm, (b) agglomerates of the as received powder, and (c) agglomerates in the pre-calcined powder. 156
Figure A.4 TEM and SEM images of 8YSZ powder from Tosoh Ltd. showing (a) single 0.1 μm particle, and (b) agglomerates of the powder as received, and (c) agglomerates of the calcined powder. 156
Figure A.5 TEM and SEM images of 10GDC powder from Fuel Cell MaterialsLtd. showing (a) single 0.15 μm particle, (b) and (c) agglomerates of the powder. . . 156

Figure B.1 Polarisation curves at (a) 700ºC and (b) 600ºC showing experimental (grey) and theoretical (blue) carbon deposition thresholds as a vertical dashed line for NiYSZ cells. 157
Figure B.2 Polarisation curves at (a) 700ºC and (b) 600ºC showing experimental (grey) and theoretical (blue) carbon deposition thresholds as a vertical dashed line for NiSSZ cells. 158

List of Tables

Table 1.1 Different types of fuel cells. 6

Table 2.1 P2G projects that use SOC technology 52

Table 3.1 Particle sizes of the materials used in the manufacturing of Ni-ScCeSZ and Ni-YSZ cells. 60
Table 3.2 Materials and their function for electrolyte, barrier and composite layers. 64
Table 3.3 Materials used in manufacturing of fuel electrode layers of SOCs. 65
Table 3.4 LSCF ink composition 67
Table 3.5 LSCF-GDC ink composition 67
Table 3.6 Electrochemical testing fuel compositions. 72
Table 3.7 CNLS fit of impedance spectrum. 74

Table 4.1 TEC values between 298 and 1073 K for YSZ, ScCeSZ and GDC. 81
Table 4.2 Details of the differences in layers from the five-layer manufacturing technique and their corresponding OCV. 87
Table 4.3 Ni-SSZ with 1.5% pore former fuel electrode porosity before and after reduction in H_2. 92
Table 4.4 Ni-YSZ with 1.5 % pore former fuel electrode porosity before and after reduction in H_2. 92
Table 4.5 Ni-YSZ with 3% pore former fuel electrode porosity before and after reduction in H_2. 92
Table 4.6 The different programmes used to investigate GDC thickness from spin-coating method. 96
Table 4.7 Comparison of internal resistances and ASR values obtained from AC impedance at OCV for cells operated on a co-electrolysis fuel mix. 109

Table 5.1 Thermodynamic parameters for species present in co-electrolysis. ΔH and ΔS values are at standard conditions and C_p values are at 1073 K. 113
Table 5.2 Reactions potentially taking place during co-electrolysis 115

Table 6.1 Average values of pCO at which the onset of carbon formation occured for NiSSZ and NiYSZ cells across the temperature range 800ºC to 600ºC. . . . 137
Table 6.2 Average mass of carbon for NiSSZ and NiYSZ cells at different operating temperatures. 141

Table 6.3 EDX results from carbon fibre image in Figure 6.16. 147

Abbreviations

AFL	Anode Functional Layer
AEL	Alkaline Electrolysis
ASC	Anode Supported Cell
ASR	Area Specific Resistance
BoL	Beginning-of-Life
BSCF	Barium Strontium Cobalt Ferrite
BSE	Back Scattered Electron
C_p	Specific Heat Capacity (J $mol^{-1}K^{-1}$)
CSS	Cathode Supported Cell
CHP	Combined Heat and Power
ECM	Equivalent Circuit Model
EDX	Energy Dispersive X-Ray
EIS	Electrochemical Impedance Spectroscopy
EoL	End-of-Life
ESC	Electrolyte Supported Cell
FU	Fuel Utilisation
GDC	Gadolinium Doped Ceria
GC	Gas Chromatography
ΔG	Gibbs Free Energy
HHV	Higher Heating Value
ΔH	Change in Enthalpy
IT-SOFC	Intermediate-Temperature Solid Oxide Fuel Cell
LSC	Lanthanum Strontium Cobalt
LSCF	Lanthanum Strontium Cobalt Ferrite
LSGM	Lanthanum Strontium Gadolinium Manganite
LSM	Lanthanum Strontium Manganite
LHV	Lower Heating Value
MS	Mass Spectrometry
MIEC	Mixed Ionic-Electronic Conductor
NiScCeSZ	Nickel Ceria Doped Scandia Stabilised Zirconia
NiYSZ	Nickel Yttria-Stabilized-Zirconia
NOx	Nitrogen Oxides
OCV	Open Circuit Voltage
OLEV	Office of Low Emission Vehicles
ORR	Oxygen Reduction Reaction

P2G	Power-to-Gas
rSOC	Reversible Solid Oxide Cell
S/C	Steam/Carbon ratio
ScCeSZ	Ceria Doped Scandia Stabilised Zirconia
SE	Secondary Electron
SEM	Scanning Electron Microscopy
SOE	Solid Oxide Electrolyser
SOFC	Solid Oxide Fuel Cell
SSZ	Scandia Stabilised Zirconia
ΔS	Change in Entropy
TCD	Thermal Conductivity Detector
TEC	Thermal Expansion Coefficient
TGA	Thermal Gravimetric Analyser
TPB	Triple Phase Boundary
TPO	Temperature Programmed Oxidation
XRD	X-Ray Diffraction
YDC	Yttria-doped ceria
YSZ	Yttria-Stabilised Zirconia

CHAPTER ONE
INTRODUCTION

1.1 Background

The need for cleaner and more efficient energy generation and storage is essential to cope with increasing energy demand and to reduce fossil fuel consumption. A good indicator of the rise in human-induced global climate-change are carbon dioxide levels; CO_2 is produced in most industrial and domestic energy conversion processes (i.e. the burning of fossil fuels). The global greenhouse gas emissions reached 51.8 $GtCO_2$ eq in 2018, a 2% increase from the previous year as shown in Figure 1.1, and are predicted to continue to rise year on year [1], resulting in a rise in global average surface temperature, a decline in arctic sea ice, and rise of global sea-level.

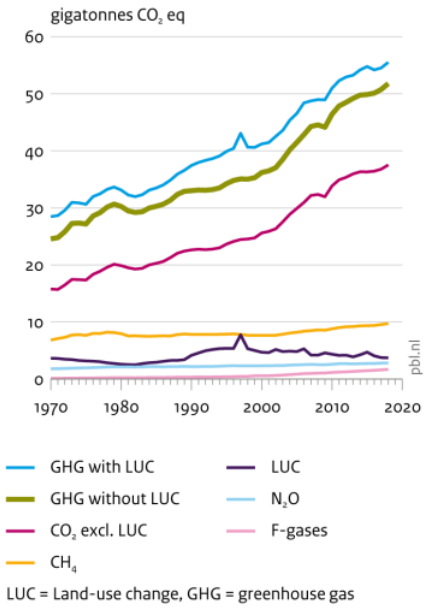


Figure 1.1: Global greenhouse gas emissions per type of gas [1].

Events and treaties such as the COP assemblies, Paris Agreement, and the UK Climate Change Act have led to a national and worldwide agreement that emissions from fossil fuels and other pollutants need to be targeted and reduced to pre-industrial levels. Not only is this important in terms of reducing pollutants in the atmosphere but also ensuring sustainability of the energy supply. Either way, a global effort is required to reshape the energy industry.

The UK is committed to reducing levels of greenhouse gases to net zero by 2050, as set out in the government's Ten Point Plan. In order to achieve this, the government has set out strategic carbon-reducing policies covering transport, agriculture, industry, power, and waste. Currently in place are policies such as; higher tax on cars that emit high levels of CO_2, regulations on air pollution from combustion plants, and funded research for carbon capture and storage (CCS) [2], hydrogen and fuel cells, among other subjects. The Committee on Climate Change collects evidence over 12 month periods, analyses, then reports to Parliament on whether or not these plans are keeping the country on track for the CO_2 emission target. There is one overarching message emerging from these reports: the previous 10 years have been a success, through the decarbonisation of electricity generation via offshore wind power, however, the reduction of emissions has slowed in the past five years and the UK is not on course to meet the next carbon budget (2023-2027). In order to reach the next target, the UK Government will need to bring forward new fully funded policies, strict enforcement on regulations and a stop to cancelling policies last minute [2].

Funding, policies and public interest in clean air technology have supported many successful developments in the hydrogen and fuel cell research area. For example, in 2004 Ceres Power patented and scaled up the production of their Steel Cell solid oxide fuel cell (SOFC) [3], and in 2017 the Office of Low Emission Vehicles (OLEV) granted ITM Power funding to boost the

creation of a hydrogen fuel infrastructure and uptake of hydrogen-powered vehicles [4]. The implementation of solar PV, onshore and offshore wind has brought the cost of renewable power down significantly. New renewable capacity is not only increasingly cheaper than new fossil fuel-fired capacity, but undercuts the operating costs alone of existing coal-fired power plants [5]. However, these types of renewable energy present considerable fluctuations in power production due to their dependence on weather conditions. In order to stabilise the energy supply and ensure full grid resilience, storage of excess energy generated in particularly windy or sunny times is vital. This is where power-to-gas (P2G) technology connects renewable electricity and energy storage to help the UK achieve its net zero carbon emission targets.

1.2 Power-to-Gas

The P2G concept converts electricity specifically from renewable energy such as wind or solar (power), to drive electrolysers to produce methane or hydrogen (gas). This gas can either be stored in the gas grid for later use, added into the gas network directly, or converted to other synthetic fuels for direct use. Producing gas in this way and storing it for later use recognises the ability to decarbonise heat, utilises the existing natural gas distribution infrastructure, and enables the de-coupling of variable energy supply from demand. There are a number of P2G projects throughout the world converting wind energy to hydrogen, each with their own limitations [6–8]. Adding hydrogen to a gas network designed for natural gas (predominantly methane) can result in degrading durability of end use appliances, therefore there is a limit on the hydrogen blend concentration (typically in the range of 5 to 25%, varying with country and pipeline network) [9]. At the beginning of 2020, the UK's first grid-injected hydrogen trial began at Keele University, injecting 20% hydrogen into the gas grid to cut CO_2 emissions without the need to change appliances [10]. This type of project will pave the way for further oppor-

tunities to de-carbonise the gas network within the UK, potentially reducing CO_2 emissions by 6 million tonnes a year (approximately 1.7% of the UK total CO_2 emissions), if the entire UK gas network were to use this 20% hydrogen blend.

1.3 Fuel Cells

In 1839, a number of scientists first explored the reaction of hydrogen with oxygen to generate current. William Grove and Christian Friedrich Schönbein independently published their findings in The London and Edinburgh Philosophical Magazine and Journal of Science at similar times, however, it is Schönbein who is credited with the discovery, and Grove who further developed the first basic fuel cell [11].

When describing fuel cells it is easy to consider the fundamentals and compare them to batteries. Both are devices that convert chemicals into energy using an electrochemical reaction, however, batteries use the chemicals stored within them so they must be replaced or recharged, whereas fuel cells are supplied with an external source of fuel for a continuous supply of energy. There are three fundamental advantages of fuel cells, which make them an attractive choice for energy generation:

Efficiency: In comparison to conventional energy from combustion engines, fuel cells can be more than twice as efficient. A typical combustion-based power plant exhibits efficiencies of approximately 35%, whereas fuel cells usually have efficiencies up to 60%, which can be even higher when the heat is also utilised [12].

Simplicity: There are no moving parts so they have very little maintenance and operate silently, making them ideal for use within buildings. The operating times are also much longer than conventional batteries, and since hydrogen can be produced anywhere there is water and electrical power, they can help build decentralised power grids.

Emissions: By avoiding combustion reactions, fuel cells produce near zero amounts of nitrogen oxides (NOx) and particulates, the only by-products are heat and water (for a hydrogen powered fuel cell), which means fuel cells are essentially emission free. Considering SOFCs fuelled by hydrocarbons such as natural gas or biogas, there are some emissions in the form of CO_2 and CO, however not on the scale of those from combustion conversion due to the higher efficiency. It is also important to consider the production of hydrogen from which fuel cells get their energy; steam methane reforming being the most popular method. This method produces CO_2, staining fuel cells' zero emission reputation.

There are a number of different types of fuel cells, all of which are energy conversion devices, that differ in the materials used, the operating temperature, and the type of fuel. Different types of fuel cells are outlined in Table 1.1 below. Fuel cells are typically named depending on the type of electrolyte used, for example, a Polymer Electrolyte Fuel Cell (PEFC) utilises a thin polymer which conducts hydrogen ions across it, whereas a Phosphoric Acid Fuel Cell (PAFC) uses a liquid phosphoric acid as the electrolyte, that also conducts hydrogen ions.

1.3.1 Solid Oxide Fuel Cells

An SOFC consists of two porous electrodes separated by a dense, ceramic electrolyte. Oxygen is reduced to oxygen ions at the cathode (Equation 1.1) and the electrolyte conducts the oxygen ions from the cathode to the anode by the difference in oxygen chemical potential. Simultaneously, the fuel is ionised at the anode, then oxidised with the migrated oxygen ions (Equation 1.2). These reactions take place at the triple phase boundary (TPB) between the electronic conductor material, the ionic conductor material and the porous network throughout the electrode. The half cell reactions that take place within an SOFC fuelled by hydrogen are thus outlined in Equations 1.1 to 1.3.

Table 1.1: Different types of fuel cells.

Name	**Operating Temperature (°C)**	**Fuel**	**Application**
Polymer Electrolyte Fuel Cell (PEFC)	50 - 90	high purity H_2	Portable power
Alkaline Fuel Cell (AFC)	90 - 100	H_2	Transport, stationary power
Direct Methanol Fuel Cells (DMFC)	40 - 80	CH_3OH	Portable power
Phosphoric Acid Fuel Cells (PAFC)	150 - 200	H_2	Stationary power
Molton Carbonate Fuel Cells (MCFC)	600 - 700	H_2, CH_4, CH_3CH_2OH, C	Stationary power
Solid Oxide Fuel Cell (SOFC)	700 - 850	H_2, CH_4, CO,	Stationary power

$$Cathode : O_2 + 4e^- \longrightarrow 2O^{2-} \tag{1.1}$$

$$Anode : 2H_2 + 2O^{2-} \longrightarrow 2H_2O + 4e^- \tag{1.2}$$

$$Overall : 2H_2 + O_2 \longrightarrow 2H_2O \tag{1.3}$$

There are two different geometries of an SOFC; planar and tubular. The planar geometry is illustrated in Figure 1.2, this is the most common geometry as it provides much higher power density over tubular designs and is less expensive to manufacture [13]. Planar cells can be circular button cells of varying diameter or square cells of varying sizes. Tubular or microtubular cells are manufactured with the same materials and components as previously described, differing in the processing, which results in a tube shaped cell, as illustrated in Figure 1.3.

Within the two geometries, are three different types of cells; anode supported cells (ASC),

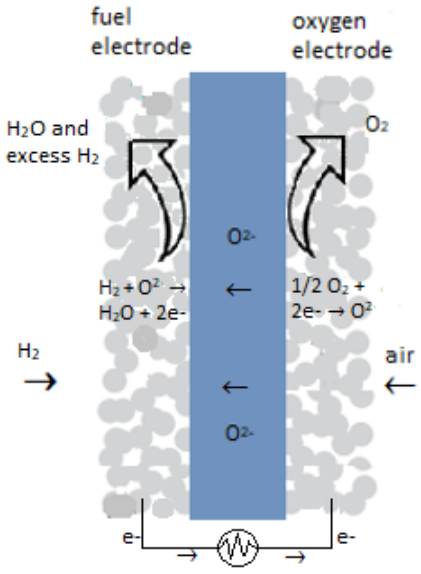


Figure 1.2: Schematic diagram of a planar SOFC showing the movement of ions and electrons.

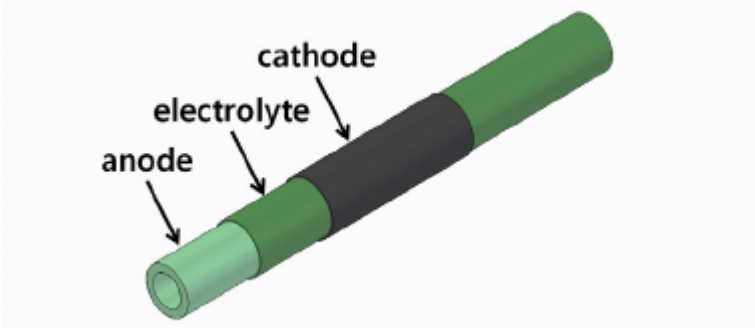


Figure 1.3: Schematic of an anode supported microtubular SOFC [14].

electrolyte supported cells (ESC) or cathode supported cells (CSC). ASC consist of a thick anode support and a thin electrolyte, which minimises ohmic losses and makes them ideal for reduced temperature operation. ESC utilise thin electrodes and a thicker, dense electrolyte, which reduces diffusion resistance and enhances sealing of the cell. The thick electrolyte results in higher ohmic losses so high temperatures must be used. CSC are the least common type; they provide a thin anode and electrolyte so reductions in common degradation mechanisms are seen. This research focuses on the manufacturing and testing of planar anode supported button cells.

1.3.1.1 Anode

The purpose of the anode is to provide many reaction sites (TPB sites) for the oxidation of the fuel. The TPB, illustrated in Figure 1.4, is a network of electronically conductive material to carry the produced electrons, ionically conductive material to carry the oxygen ions, and pores to facilitate the percolation of the gaseous fuel. The microstructure of the anode is therefore porous, with the optimal porosity values between 25 and 40% [15]. Ni is a typical anode material used for its catalytic activity, high electronic conductivity, and relatively low cost. Yttria-stabilised zirconia (YSZ) is a common electrolyte material due to its high ionic conductivity, and low electronic conductivity. YSZ is usually combined with Ni to make a composite anode (cermet), which increases the TPB reaction sites and reduces the thermal expansion mismatch between the two materials. This research will focus on the use of YSZ and another electrolyte material, ceria-doped scandia-stabilised zirconia (ScCeSZ).

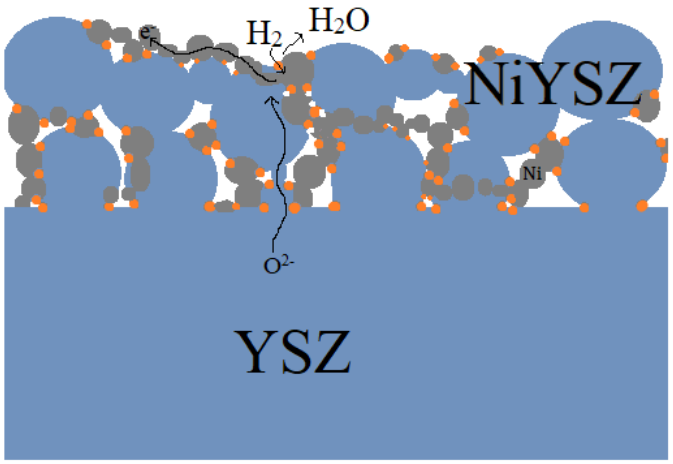


Figure 1.4: Schematic diagram of the TPB reaction sites at the fuel-electrolyte interface of a NiYSZ cell with hydrogen fuel. TPB sites are identified in orange.

1.3.1.2 Electrolyte

The main features of a good electrolyte are; dense microstructure to stop gas cross-over, high ionic conductivity to facilitate the movement of oxygen ions, very low electronic conductivity to ensure no short-circuits, and a thin layer to reduce ohmic resistances within the cell (if using ASC or CSC). Like the electrodes, the electrolyte must have similar thermal expansion coefficient (TEC) to the surrounding material to minimise any thermal stresses upon heating and cooling.

1.3.1.3 Cathode

Similarly to the anode, the cathode must have a porous microstructure which provides TPB sites for the oxygen reduction reaction (ORR) to take place. The material must be stable in an oxidising environment, have high electronic conductivity and be thermally and chemically compatible with the electrolyte. Lanthanum strontium manganite (LSM) is a common material choice which operates well at high temperatures. At lower temperatures its performance decreases, so other materials such as lanthanum strontium cobalt ferrite (LSCF) are used. However, LSCF is not chemically compatible with YSZ electrolytes therefore an additional layer of gadolinium doped ceria (GDC) is required as a barrier layer.

1.4 Electrolysis

The majority of the world's hydrogen production comes from steam methane reforming (Equation 1.4), a reaction involving the breakdown of natural gas into syngas (synthetic gas); a mixture of hydrogen and carbon monoxide. There are also numerous subsequent steps to purify the hydrogen until it is ready for transportation. Other ways of producing hydrogen via natural gas

include partial oxidation (Equation 1.5), authothermal reforming (ATR) (Equation 1.6), or coal gasification. These methods still rely upon fossil fuels and produce large quantities of carbon monoxide and carbon dioxide, a disadvantage that comes with the high efficiencies (60-85%) [16].

$$CH_4 + H_2O \longrightarrow CO + 3H_2 \tag{1.4}$$

$$CH_4 + \frac{1}{2}O_2 \longrightarrow CO + 2H_2 \tag{1.5}$$

$$2CH_4 + \frac{1}{2}O_2 + H_2O \longrightarrow 2CO + H_2 \tag{1.6}$$

Another, cleaner way of producing hydrogen is from water electrolysis, which splits water into its constituent components, hydrogen and oxygen, using electricity. The benefit of using electrolysis to produce hydrogen is clear; the only emissions are oxygen and, when coupled with electricity from renewable energy sources, for example solar or wind, the process does not produce greenhouse gases. The reaction in an electrolysis cell (Equation 1.9) is the exact reverse of that in a fuel cell (Equation 1.3). Water is the fuel, which gets reduced to H_2 and O^{2-} ions at the cathode (SOFC anode) as shown in Equation 1.7, the O^{2-} ions migrate across the electrolyte where they are evolved at the anode (SOFC cathode) as O_2 (Equation 1.8). Figure 1.5 shows the directions of ions and electrons, and the reactions that occur within an SOE fuelled by water. The direction of ion transport reverses, so the anode and cathode swap in comparison to an SOFC.

$$Cathode : 2H_2O + 4e^- \longrightarrow 2H_2 + 2O^{2-} \tag{1.7}$$

$$Anode : 2O^{2-} \longrightarrow O_2 + 4e^- \tag{1.8}$$

$$Overall : 2\,H_2O \longrightarrow 2\,H_2 + O_2 \tag{1.9}$$

There are two types of low-temperature electrolysis: Alkaline Electrolysis (AEL) and Polymer Electrolyte Membrane (PEM) electrolysis, which operate at temperatures from 50 to 90ºC. The drawbacks to low-temperature electrolysis are the low current density of the alkaline electrolysers and, in the highly corrosive nature of PEM electrolysers.

1.4.1 Solid Oxide Electrolysis (SOE)

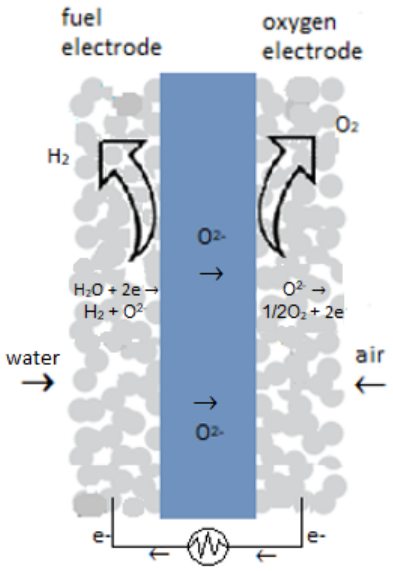


Figure 1.5: Schematic diagram of an SOE showing the movement of ions and electrons.

Another type of electrolyser is the high-temperature solid oxide electrolyser (SOE), which operates between 600 and 900 ºC. Like in SOFC, SOE do not require any precious metal catalysts due to the elevated temperatures. The argument in favour of high temperature SOE lies in the relationship between enthalpy, temperature and entropy (Equation 1.10); it is thermodynamically advantageous to run an electrolyser at an elevated temperature, as illustrated in Figure

1.6.

$$\Delta G = \Delta H - T\Delta S \tag{1.10}$$

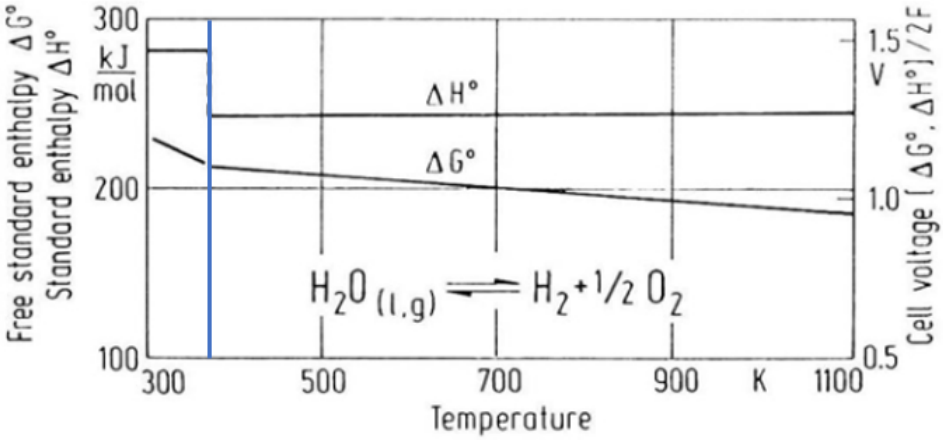


Figure 1.6: Electrical energy input (ΔG) and total energy (ΔH) for the electrolysis of water as a function of temperature [17].

Figure 1.6 shows how with increasing the temperature of the electrolysis reaction, the electrical energy input (ΔG) steadily decreases whilst the overall energy (ΔH) stays almost constant. This diagram is often cited as the motivation for high-temperature electrolysis versus low-temperature electrolysis. The blue line at 100ºC indicates the phase change from liquid water to steam, where ΔH decreases from 285.83 kJ mol^{-1} to 241.83 kJ mol^{-1}. By operating water electrolysis at elevated temperatures, the production cost of hydrogen can be significantly reduced, especially if the heat supplied to the system comes from a waste heat source from industrial processes such as steel plants. However, the elevated temperatures also cause thermal stresses within the cell, and the materials used in these high temperature environments can be expensive. Furthermore, the high degradation rate in SOE is another challenge that has to be overcome before widespread SOE commercialisation.

High-temperature electrolysis of water can occur exothermally, endothermally or thermoneu-

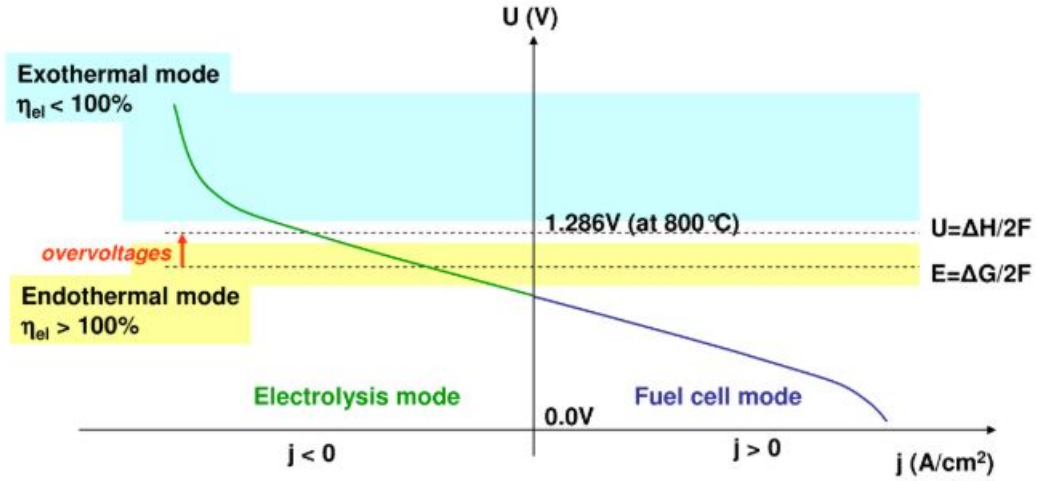


Figure 1.7: Operating modes of high-temperature SOC [18].

trally, depending on the operating voltage, as depicted in Figure 1.7. When the electrical energy input is below ΔH the electrolysis reaction is endothermic and requires heat to be supplied to the reaction. Operating in this region gives electrical efficiencies of over 100% and low degradation rates due to its low current density region. In exothermal mode, the electrical energy input is greater than ΔH, which generates heat from the cell. In this region, electrical efficiencies are below 100% and can result in higher degradation due to the high current density. The thermoneutral voltage (V_{th}) is defined as the voltage at which ΔG = ΔH. The heat demand for the reaction (TΔS) equals the heat released by the electrochemical and ohmic losses within the cell, resulting in a conversion efficiency of 100%, with no heat loss to the surroundings. The (V_{th}) can be calculated from Equation 1.11, and has a value of 1.29 V for a cell operating at 800ºC.

$$V_{th} = \frac{\Delta H}{nF} \tag{1.11}$$

1.5 Reversible Solid Oxide Cells

Due to the reversible nature of the water splitting reaction, the combination of an SOFC and SOE in one is in a cell or stack capable of switching between power generation mode (fuel cell) and fuel generation mode (electrolysis) in one system. This Reversible Solid Oxide Cell (rSOC) is an attractive technology that has a lot of potential for the storage and conversion of fluctuating renewable energy sources in the future energy mix. In electrolysis mode, electrical energy from wind or solar can be converted into chemical energy and stored as H_2 or syngas (mixture of H_2 and CO), from the co-electrolysis of H_2O and CO_2. This can then be further processed by Fischer Tropsch or methanation reactions into synthetic fuels, which can also be used in transportation or stored. Alternatively, the converted H_2 or syngas can be used directly in the rSOC to produce electricity when wind or solar energy isn't available. The efficiencies of such systems can reach 80%, especially when the heat produced in fuel cell mode is recovered in electrolyser mode [19].

The anode is defined as the electrode where electrons are generated and the cathode is defined as the electrode where electrons are used. Therefore, in a fuel cell, the anode is where the hydrogen fuel is fed and the cathode is where the oxygen is fed. In the reverse reaction (electrolysis) the anode becomes the cathode and vice versa. Hence, when discussing rSOCs, the electrodes are referred to as the oxygen electrode and the fuel electrode [20–23].

One of the benefits of rSOCs is that the same cell or stack can be used in two different modes, which eliminates the need for two sets of balance-of-plant (BoP) components, reduces costs, and allows for a simpler system architecture. The rSOC is traditionally based on the more developed SOFC materials set (Ni-YSZ fuel electrode, YSZ electrolyte, and perovskite oxygen electrodes such as LSM or LSCF), and, consequently, when the rSOC is run in electrolysis

mode, a considerable degradation is observed, generally higher than in fuel cell mode.

1.6 Thermodynamics

The electrochemical half reactions for the electrode reactions in rSOCs fuelled by H_2, H_2O, CO_2 and CO are given below. The oxygen electrode reaction is stated in Equation 1.12, where the forward reaction is oxygen reduction in fuel cell mode and the reverse reaction is oxygen evolution in electrolysis mode.

$$\frac{1}{2}O_2 + 2e^- \rightleftharpoons O^{2-} \tag{1.12}$$

The fuel electrode reaction is given in Equation 1.13 where the forward reaction is the hydrogen oxidation in fuel cell mode and the reverse reaction is hydrogen evolution in electrolysis mode.

$$H_2 + O^{2-} \rightleftharpoons H_2O + 2e^- \tag{1.13}$$

When fuelled by CO_2 or CO, the fuel electrode reaction becomes Equation 1.14, where the forward reaction is carbon monoxide oxidation in fuel cell mode and the reverse reaction is carbon monoxide evolution from CO_2 electrolysis.

$$CO + O^{2-} \rightleftharpoons CO_2 + 2e^- \tag{1.14}$$

The theoretical amount of voltage available from a fuel cell can be derived by the half reactions in Equations 1.13 to 1.14 and the equations below. Equation 1.13 shows that in the formation of one mole of H_2O, one mole of H_2 and oxygen ions, and two moles of electrons ($2N_A$ where N_A is Avogadro's number) are required. Considering the charge (Q) on one electron (e), Q = $2N_Ae$ is the charge involved in the reaction. Faraday's constant (F) is defined as the

magnitude of electric charge on one mole of electrons, or F = eN_A. Substituting gives

$$\mathrm{Q} = 2\mathrm{N_A e} = 2\mathrm{F} \tag{1.15}$$

The potential difference (E) is defined as the work done (W_{elec}) per unit charge (Equation 1.16).

$$W_{elec} = EQ \tag{1.16}$$

Assuming the reaction in the fuel cell is reversible with no energy losses, then the Gibbs free energy is fully converted into electrical work (W_{elec}):

$$\Delta G = W_{elec} = EQ \tag{1.17}$$

Combining Equation 1.15 and Equation 1.17, the standard potential (E^0) can be calculated from the Gibbs free energy of formation of water from pure H_2 and O_2 at a certain temperature (Equation 1.19). The Gibbs free energy is calculated by the well-known equation:

$$\Delta G = \Delta H - T\Delta S \tag{1.18}$$

$$E^0 = \frac{\Delta G}{2F} \tag{1.19}$$

For example, the Gibbs free energy of formation at 298 K is -237.15 kJ mol^{-1}. By substituting this value into Equation 1.19, the reversible voltage, E^0, of a H_2 fuel cell is determined as:

$$E^0_{298K} = \frac{237,150 J mol^{-1}}{2(96,485) C mol^{-1}} \tag{1.20}$$

$$E^0_{298K} = 1.23 \text{ V}$$

1.6.1 Nernst Potential

The Nernst Equation (Equation 1.21) is an expression of the maximum open-circuit voltage as a function of temperature and pressure; it provides the cell equation under non-standard

conditions.

$$E = E^0 + \frac{RT}{nF} ln \frac{a_{reactants}}{a_{products}} \tag{1.21}$$

Where R is the gas constant and a is the species activities, assuming the gases are ideal, the a of the gases equal their partial pressures and the a of water is unity, for a H_2 fuel cell the Nernst Equation then becomes:

$$E = E^0 + \frac{RT}{2F} ln \frac{P_{H_2} . P_{O_2}^{0.5}}{P_{H_2O}} \tag{1.22}$$

1.6.2 Overpotentials

Irreversible losses, or overpotentials, due to fuel crossover through the electrolyte, internal currents from electron leakage and contaminants cause a voltage drop from the Nernst potential to the actual cell voltage. As the cell starts drawing current, three main regions dominate the polarisation curve, each denoting a particular type of overpotential:

- Activation losses: caused by slowness of reactions and reactants to move away from the electrode (part of the voltage is used for transport),
- Ohmic losses: current passing through electrodes and electrolyte,
- Mass transport losses: when the balance of reactants and products in the Nernst Equation (Equation 1.22) tilts towards products.

These losses are the same for electrolysis and fuel cell mode. In electrolysis, the losses cause an increase in cell voltage, whereas in fuel cell mode they cause a decrease in cell voltage.

1.6.3 Polarisation Curve

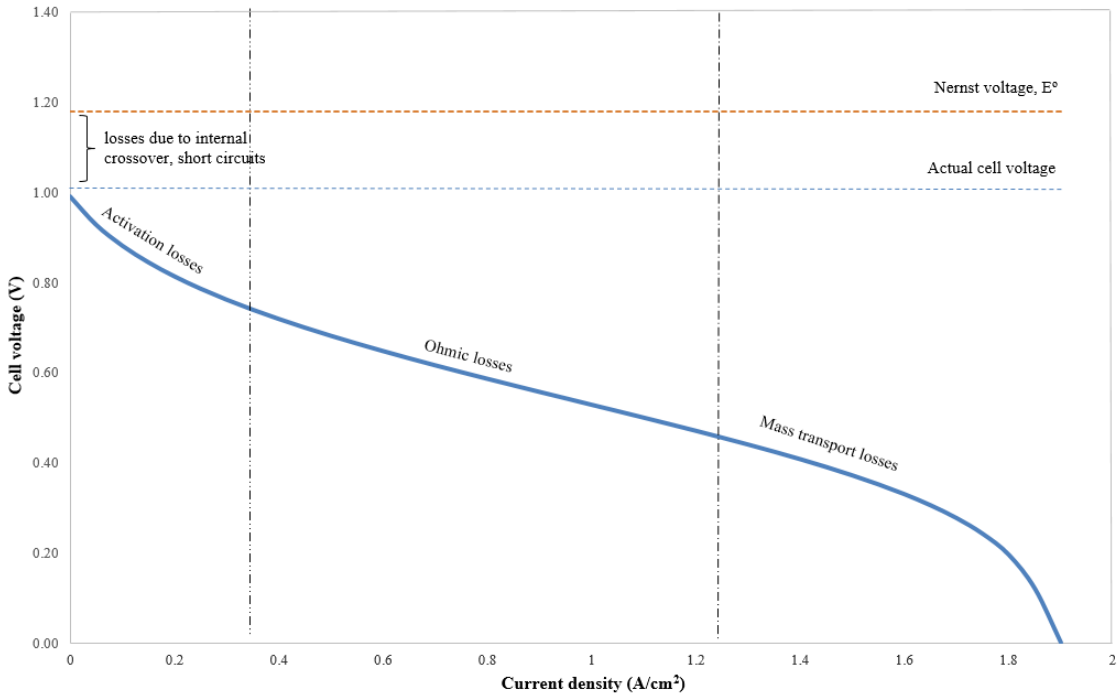


Figure 1.8: A typical polarisation curve for a fuel cell showing losses, Nernst voltage and actual cell voltage.

Polarisation curves, or current-voltage ($i-V$) curves, are used to describe fuel cell and electrolyser electrochemical performance and stability. Figure 1.8 illustrates a typical polarisation curve for a fuel cell, showing how losses (activation, ohmic and mass transport) reduce the theoretical voltage to the actual operating voltage shown. These polarisation curves are used to compare different cells by inspecting the shape of the curve (what losses are dominant), the current density (which relates to the power produced by the cell), and the open circuit voltage (OCV), which indicates how well sealed the cell is, how gas tight the electrolyte is, and whether or not there are internal leak currents. Area specific resistances (ASR) can be read from polarisation curves by calculating the gradient of the slope in its linear region. rSOC polarisation curves are usually dominated by ohmic losses, therefore they tend to be almost linear from the

OCV, until transportation limitation begins.

1.7 Fuel Flexibility

As previously mentioned, SOFC and SOE benefit from high operating temperatures, which eliminate the need for precious metal catalysts, promote internal reforming, increase fuel flexibility, and produce high quality by-product heat for CHP systems. In a conventional SOFC, H_2 is oxidised to form H_2O, heat and electricity. Advantageously, hydrocarbons such as CH_4, CO, ethanol or biogas, can also be used as a fuel in an SOFC to produce H_2 and CO_2 in an internal reforming reaction. In CH_4 fed fuel cells, there are three types of internal reforming reactions that can occur; partial oxidation (POx), dry reforming (DR), and steam reforming (SR), shown in Equations 1.23, 1.24 1.25, respectively.

$$CH_4 + 0.5\,O_2 \longrightarrow 2\,H_2 + CO \tag{1.23}$$

$$CH_4 + CO_2 \longrightarrow 2\,H_2 + 2\,CO \tag{1.24}$$

$$CH_4 + H_2O \longrightarrow 3\,H_2 + CO \tag{1.25}$$

One consequence of using hydrocarbons in SOFCs is the higher rates of degradation, in particular carbon build up and sulphur poisoning of the fuel electrode [24]. In an attempt to inhibit this, much research has gone into optimising electrode materials, fuel composition and electrode doping.

SOEs can also utilise the high temperatures and hydrocarbon fuel sources; CO_2 electrolysis (Equation 1.26) is used in CO_2 capture and utilisation (CCU) systems [25]. Co-electrolysis, the simultaneous reduction of CO_2 and H_2O (Equation 1.27), produces high quality syngas (mix-

tures of predominantly H_2 and CO) [26, 27]. As mentioned in Section 1.4, these electrolysis reactions also thermodynamically benefit from operating at high temperatures, due to a larger proportion of the energy requirement coming from heat rather than electricity.

$$CO_2 \longrightarrow CO + 0.5\,O_2 \tag{1.26}$$

$$CO_2 + H_2O \longrightarrow CO + H_2 + O_2 \tag{1.27}$$

1.8 Motivations

rSOCs have been a topic of interest in the energy industry for some years now due to their ability to produce fuel for storage in electrolysis mode and consume this fuel to produce electricity in fuel cell mode in one single unit, potentially reducing costs. However, one of the primary issues hindering their widespread commercialisation is the degradation of the cell, which can significantly reduce the lifetime. These effects, such as electrode poisoning, air electrode delamination, and fuel electrode redox stability, have been investigated extensively in the literature for SOFC and SOE [28–31] separately, yet there is little understanding of how cycling between the two modes affects the different types of degradation.

This research focuses on the degradation phenomena of carbon deposition when operating rSOCs on carbon-containing fuels, specifically in co-electrolysis. By using low cost manufacturing techniques, cells of differing anode and electrolyte material have been manufactured and their performance and durability as SOCs examined. In doing so, the main challenge was to examine the material degradation and reduce electrode poisoning via carbon build up whilst using carbon-containing fuels.

1.9 Aims of the thesis

1. Manufacture planar fuel electrode supported Ni/YSZ and Ni/ScCeSZ cells via reverse aqueous tape casting technique, adapting the method from [32] to incorporate LSCF oxygen electrode and a GDC barrier layer.

2. Test the electrochemical performance of each cell in fuel cell and electrolyser mode. Test the cell reversible performance using a fuel mixture of CO_2, H_2O, H_2, CO and O_2.

3. Investigate how the Ni/ScCeSZ cells perform in comparison to conventional Ni/YSZ cells when using carbonaceous fuels, such as gas mixtures for co-electrolysis of CO_2 and H_2O. Identify and compare the threshold of carbon formation during co-electrolysis across different temperatures, including the intermediate-temperature range, for Ni/ScCeSZ and Ni/YSZ cells.

1.10 Thesis Overview

As outlined in the aforementioned chapter, Chapter 1 gives context to this research by outlining how more research into clean air technologies are needed to mitigate the negative effects of climate change, and where solid oxide cells (SOCs) can sit within policy, society, and technology, in order to contribute to a more sustainable future. This chapter also introduces the basic principles behind fuel cells, electrolysers and power-to-gas systems, detailing the typical materials used for each component of a SOC. By highlighting the benefits of high-temperature cells over low-temperature cells, and the challenges faced with this technology, the objectives of this thesis was set out.

Chapter 2 contains a review of the literature surrounding SOC manufacturing via tape cast-

ing. Then there is a discussion on types of degradation found in SOFCs and SOEs, and what has been done previously to minimise the degradation rate and extend the lifetime of the cells. The discussion moves onto degradation when these cells are operated in reversible mode (RSOCs). The literature review then addresses the operating window where carbon deposition is likely to form, the types of carbon formed and previous mitigation strategies found in the literature. This chapter also looks at previous research surrounding the co-electrolysis reaction in SOCs and the carbon forming window with respect to current density. This sets the stage for the following chapters on carbon forming during co-electrolysis in RSOCs.

Chapter 3 describes the methods that were implemented in this thesis. A library of information is given for all of the materials used in this research, including the material characterisation that was carried out. The two methods for cell manufacturing are outlined; reverse aqueous tape casting using a novel composite layer, and a spin coated layer. The testing schedule is detailed and the fundamentals of the electrochemical testing and post-mortem analysis is explained.

Chapter 4 focuses on the optimisation of the manufacturing technique, and consists of the published paper 'Five-layer reverse tape casting of IT-SOFC'. This chapter details the process of manufacturing cells based on previous work in the same research group. It was necessary to adapt this method to incorporate the GDC barrier layer and LSCF oxygen electrode, which allowed for good performance during SOFC and SOE mode at the intermediate temperature range. Two types of cells were manufactured and their performance assessed against each other and commercial cells to determine the optimal manufacturing technique. Cells were testing in SOFC mode, SOEC mode and RSOC mode on a variety of fuel compositions. The cell's material set is Ni-ScCeSZ/ScCeSZ/GDC/LSCF-GDC/LSCF ("NiSSZ") and reference cell Ni-YSZ/YSZ/GDC/LSCF-GDC/LSCF ("NiYSZ").

Chapter 5 provides a look into the thermodynamics of the co-electrolysis reaction, in particular carbon formation during this reaction, with respect to operating temperature, fuel composition, and current density. This chapter identifies the theoretical operational window whereby carbon should not form, providing a benchmark for the experimental section in the following chapter.

Chapter 6 brings all previous chapters together by identifying the experimental carbon deposition thresholds for the in-house manufactured cells and reference cells. Carbon deposits are analysed and measured for each intermediate-temperature operation, enabling the NiSSZ' performance in comparison to the NiYSZ reference cells to be quantified. Chapter 7 therefore concludes the benefit of using NiSSZ material as a carbon forming mitigation strategy in SOCs during co-electrolysis.

CHAPTER TWO

LITERATURE REVIEW

This chapter discusses the different approaches to manufacturing SOC, specifically the tape casting method, and the types of degradation that are exhibited in fuel cell, electrolyser and reversible mode, with a special emphasis on SOE operation. The materials primarily used in this study, and which will mainly be referenced in the following, were a Ni-ScCeSZ fuel electrode, a ScCeSZ electrolyte, a GDC barrier layer and an LSCF-GDC/LSCF double layer oxygen electrode. To compare performance, the Ni-ScCeSZ cells were tested alongside conventional Ni-YSZ cells consisting of a Ni-YSZ fuel electrode, a YSZ electrolyte, a GDC barrier layer and an LSCF-GDC/LSCF double layer oxygen electrode.

2.1 Manufacturing of cells: Tape Casting

Tape casting is a well-established, cost effective method of producing homogeneous green tapes. A 'green tape' refers to an unsintered, flexible tape that will typically be sintered to achieve a solid, thin specimen, such as a tile or substrate. The first documented use of tape casting was over 70 years ago by Howatt who used it to rapidly produce mica capacitors during World War II [33]. Nowadays, it is the preferred method for mass production of thin ceramic tapes or sheets due to the ability to produce layers with a range of thicknesses in a continuous process. Ap-

plications of thin ceramic sheets include multilayered capacitors, electronic substrates, porous membranes, and fuel cells. Single thin layers can be used directly or they can be laminated to make multilayer materials, which can be used as multilayer ceramic capacitors (MLCC), multilayer ceramic packages (MLCP) from both high temperature and low temperature ceramics, ceramic multi-chip modules (MCM), functionally graded materials, and ceramic fuel cells (SOFC and MCFC) [34]. It is possible to make a thin tape out of nearly any powder material,

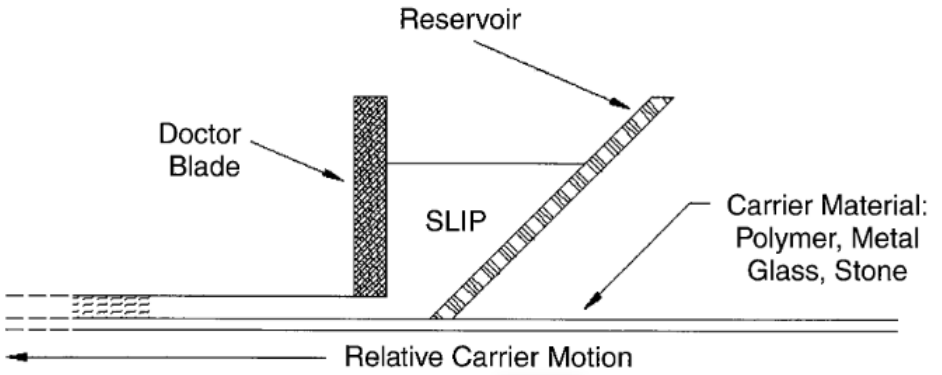


Figure 2.1: Schematic diagram of the basic principle of tape casting, using doctor blade and carrier film [35].

by first turning it into a slurry or slip by adding solvent, binder and other additives, then spreading it across a flat surface using a doctor blade. Typically, the slurry is poured into a reservoir behind the doctor blade and the carrier film of polymer, stone, glass or metal starts to move, releasing the slurry as it does, as illustrated in Figure 2.1. The cast tape is then introduced to a heated chamber where it dries. Variables such as gap height between the doctor blade and the carrier film, traverse speed and slurry viscosity are all considered in order to obtain a well defined thickness of the thin film. For large-scale operations, the carrier film is attached to a moving belt and the doctor blade is stationary, however, for smaller applications, such as the work carried out here, the doctor blade is automatically pushed along the stationary carrier film, and the film is then dried separately. This section reviews how researchers approach the tape

casting technique to produce thin multi-layer ceramic sheets.

Tape casting can be divided into two categories; aqueous-based and organic-based. The difference lies in the type of solvent used to dissolve the additives. Organic-based tape casting uses solvents such as ethanol, methanol, methyl ethyl ketone (MEK), amongst others, and is the more 'traditional' and more widely used method in industry due to the wider choice of additives, shorter drying times and therefore higher productivity. However, these organics are usually harmful to health and the environment, which is why there has been an increasing interest in aqueous-based tape casting. Zhou explains how aqueous-based tape casting is more affordable but has added complexity due to the high dielectric constant of water and high forces of attraction between particles, making it more challenging to form a well dispersed slurry [36]. Organic-based tape casting typically leads to tapes that are more dense and show less defects than the water-based alternative. Finally, there are fewer additives available for aqueous-based slurries compared to organic-based, and the drying time is longer as the vapour pressure of water is lower than for organic solvents [35].

2.1.1 Starting materials

In order to create a tape that is free of cracks and flaws, it is important to choose components that all work together. The first thing to identify is the powder morphology, then a binder that will encase the powder, then a solvent that can dissolve the binder and other additives [35]. The pairing of binder and additives to the solvent is an important step because the solvent must effectively dissolve all of the additives. Sometimes two solvents are used (dual solvent systems) to ensure complete dissolution. The type, amount, and order of addition of additives and powders to the slurry all influence the characteristics of the final tape; its density, porosity, thickness, strength, and homogeneity.

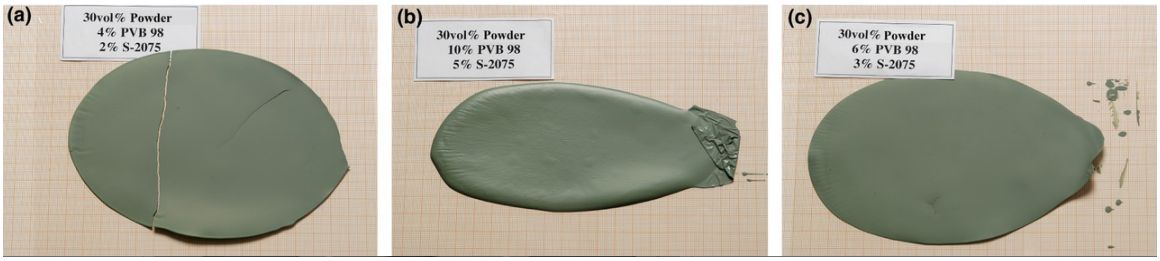


Figure 2.2: Effects of (a) 4% PVB, (b) 10% PVB, and (c) 6% PVB on green tape [37].

The binder is the continuous phase within the slurry that holds all of the particles in place until the green tape is sintered. The amount of binder affects the strength, flexibility and smoothness of the green tape. Common binders include poly vinyls [36, 38], acrylics [39], or cellulose [40]. The binder is burned off in the presence of oxygen at high temperatures during sintering, leaving behind the solid ceramic. The quantity of binder in the tape is critical; too much results in a tape with more tensile strength but lower green density, and too little results in a dense green tape that is too brittle and cracks upon drying [41]. Schafbauer et al. [37] identified a range for binder quantity in the slurry. Adding large amounts (10 wt%) of poly vinyl butyral (PVB) led to high viscosity which caused poor de-gassing and pinholes to form in the dried green tape (Figure 2.2 (b)). Low amounts (4%) led to cracking of the green tape (Figure 2.2 (a)). Similarly, cellulose binders exhibit poor de-gassing and viscous qualities and so prove more difficult to obtain a defect free green tape [42]. Most researchers agree that using approximately 5 wt% binder results in a smooth, flexible tape [36, 37, 41, 43].

The plasticisers allow the tape to bend and flex so that cutting, laminating and punching will not result in cracking. Type I plasticiser softens the polymer, lowering the stress/strain curve of the binder. Type II plasticiser increases the flexibility before failure. The addition of both type I and type II plasticiser is displayed in Figure 2.3. Types of plasticisers include (poly)Ethylene (PE) [43], glycerin, polymethyl methacrylate (PMMA) [44], dioctyl phthalate

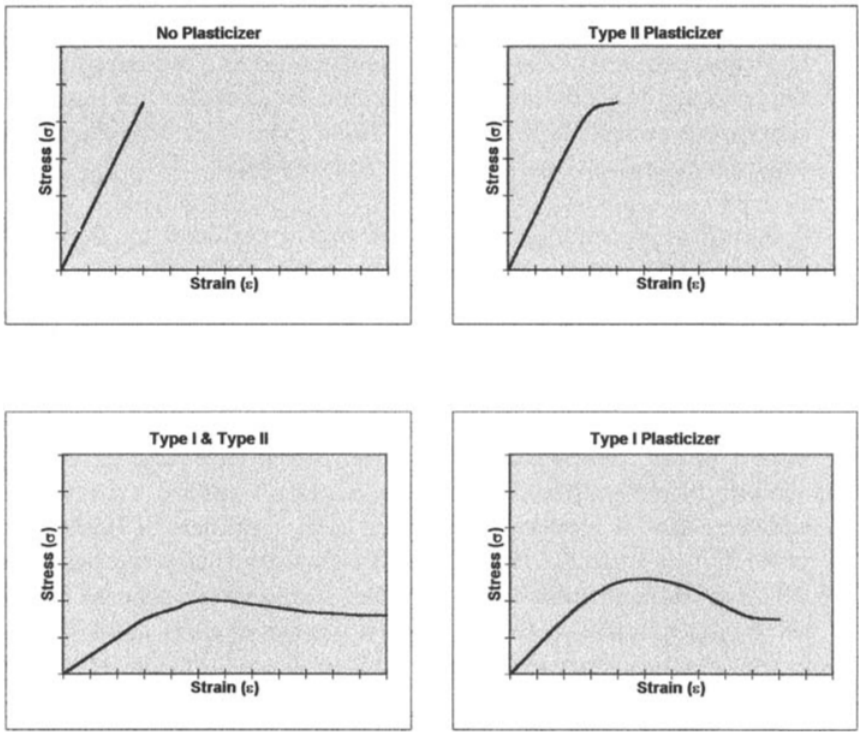


Figure 2.3: Stress-Strain properties of binder with and without Type I and Type II plasticisers [35].

(DOP) [45]. Plasticisers with low molecular weight result in tapes that have better bendability due to the higher mobility of the smaller polymer chain. Kim et al. [46] studied the effect of different plasticisers including PEG 400 and PEG 1350, and their effect on the bendability of green tapes. Figure 2.4 illustrates how the tapes exhibit more elongation when a low molecular weight plasticiser was used.

The role of the solvent is to contain all the different components within the slurry, ensuring they can be dissolved and evenly distributed in order to work effectively. The amount of solvent used alters the viscosity of the slurry and therefore its application onto the carrier film. It must be able to evaporate quickly, which is why many researchers prefer to use organic solvents as they dry much faster than aqueous-based solvents [47, 48]. Wang [49] has compared the use of aqueous-based tape casting with solvent-based tape casting and concluded both are suitable for producing uniform microstructure and homogeneous distributions, with the only notable

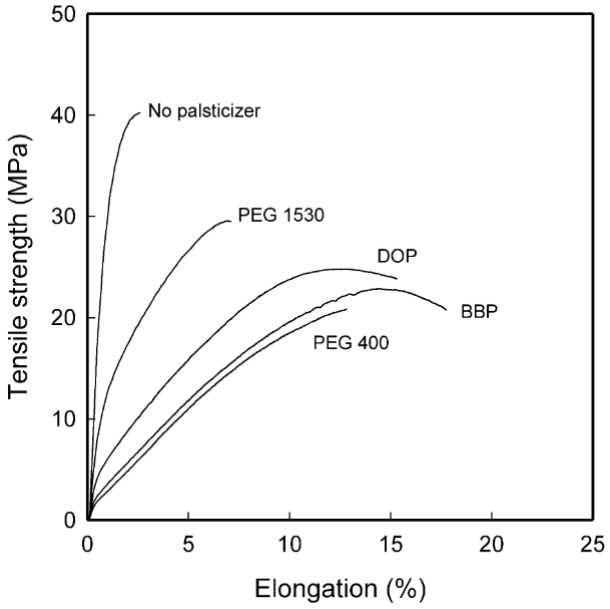


Figure 2.4: Elongation-tensilestrength curves of green tapes with different plasticisers [46].

difference being the drying times, and more difficulty de-foaming the aqueous-based tape. Both tapes produce similar electrical properties. Similarly, Nahass et al. [50, 51] found that the only difference in using aqueous solvent versus non-aqueous was that the aqueous process was more sensitive to process changes such as drying and film thickness.

Dispersants ensure all of the powder particles are held in place without risk of sedimentation. Goulart et al. [39] carried out ageing studies on YSZ electrolyte slurries using ammonium polyacrylate and found that the slurries were stable for several days before flocs began to form. Schafbauer et al. [37] carried out similar sedimentation tests and found the addition of 1.5 wt% dispersant was the optimum concentration for prolonged dispersion of particles. The dispersant has the lowest wt% of all additives in the slurry, and in some cases it is left out all together. This is because some of the other additives have dual effects, for example the binder can display certain dispersing and plasticising qualities and in some cases can outweigh the dispersing action of the dispersant itself [35].

The one component of starting materials not under control during the manufacturing process

is the properties of the powders. These variables include, but are not limited to, surface area, particle size, density and moisture content. Each batch of powders has slight variances in these parameters, which can greatly affect the bulk green density of the dried tape [50]. Keeping a library of as many of these variables as possible is important to track changes in slurry and tape manufacturing outcomes.

2.1.2 Sacrificial Pore Formers

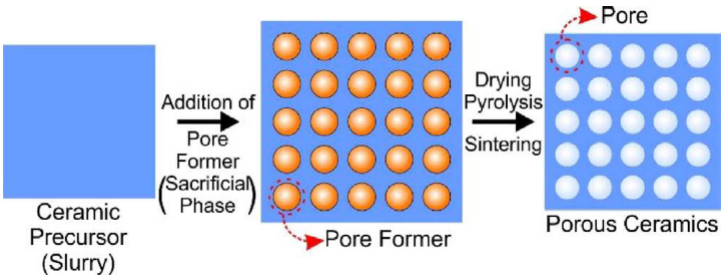


Figure 2.5: Schematic diagram of how pore formers introduce porosity to electrodes [52].

Being able to control the porosity and microstructure of the electrodes is important in minimising concentration polarisation and manufacturing high-performing SOCs. Porosity is introduced to the system in three ways: through the reduction of NiO to Ni, from the burnout of the additives during sintering, which is limited but still influences overall density, and/or by the addition of a pore former, which is also burnt off, leaving pores behind. Pore formers can be synthetic organics such as polymer beads, or natural polymers such as starch and cellulose, or metallics such as graphite, carbon and nickel. Sarikaya et al. [45] investigated the pore forming effects of flaked graphite, spheroidal graphite, PMMA, sucrose, and polystyrene on the microstructural development of tape cast ceramics to find that both types of graphite do not require a slow heating profile for a defect-free burnout stage. Graphite-based pore formers also yield the highest bulk porosity irrespective of their morphology.

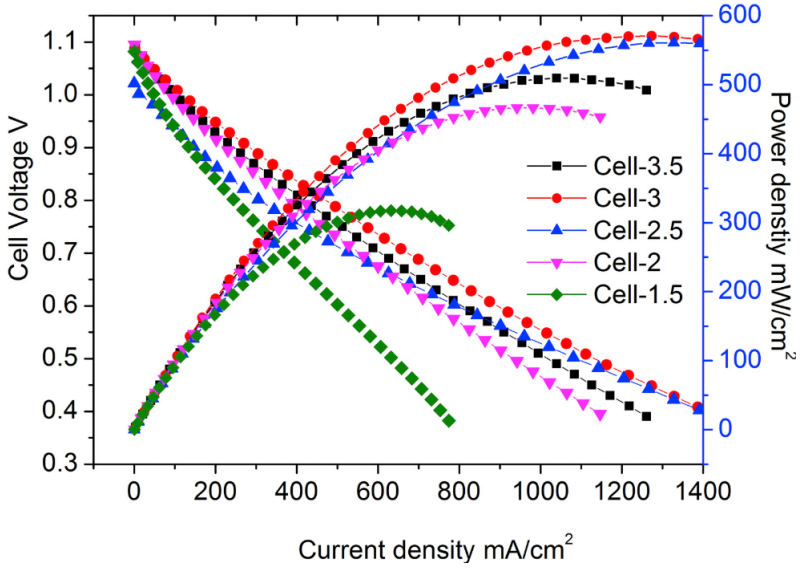


Figure 2.6: Polarisation curve of Ni-YSZ ASC made with varying amount of pore former: 1.5 wt%, 2 wt%, 2.5 wt%, 3.5 wt% and 3 wt% [53]. Cells are named with the amount of pore former used.

In terms of optimal electrode microstructure, there is a trade off between gas diffusion to the TPBs, and the loss of the TPB network, and therefore electrical and ionic conductivity, with too many pores. Most SOFC studies use a fuel electrode porosity of 30%, within the range of 25% to 35%, to yield low diffusion resistances and increased cell performance. Zhou et al. [53] found that the electrochemical performance of aqueous-based tape cast anode supported cells (ASC) increased with increasing potato starch content up to 2.5 wt%, beyond which it gave worse performance due to break-down of the TPB percolating network, as can be seen in Figure 2.6. In another study, Sanson et al. [54] used four different pore formers to reveal that the morphology of the pore formers affects the sintered porosity and the green density. For smaller particles (ie. carbon black), more solvent and binder is required to optimise the microstructure accordingly. In terms of rSOC microstructure, there is a gap in the literature in terms of optimal microstructure in the different operational modes. Nevertheless, the different requirements have been briefly identified by Ebbesen et al. [24] and Hanifi et al. [55]. In fuel cell mode, diffusion resistances are unchanged at high current densities, however, in electrolysis mode, high current

densities result in a significant increase in diffusion resistances. Increasing the porosity in the fuel electrode support influences both the diffusion resistance and the concentration resistance at high current density in electrolysis mode. This work suggests a more porous fuel electrode would see an increased performance in rSOCs.

2.1.3 Drying Without Defects

The drying process of a tape is make or break; if it is not done correctly defects form and the tape is unusable. During the drying process the solvent moves up through the tape to the surface where it evaporates off in a one-sided drying process. As previously mentioned, a non-aqueous solvent dries quickly leaving behind a smooth, defect free, and dense green sheet. On the other hand, using aqueous-based tape casting means an increased drying time to minimise risk of cracks or bubbles forming. Nevertheless, this does not require a fume cupboard.

In the majority of cases, tapes are dried overnight at room temperature [36, 47, 56], and the minority dry tapes in a closed system at elevated temperatures [57]. Spauszus et al. [50] observed that during aqueous tape casting humidity is key. Ensuring sufficient relative humidity whilst drying and a residual humidity of 2 to 5 wt% in the dried green tapes avoids fragility and breakages. It is important to consider the geographical location and time of year of where the tapes are being manufactured as this will effect the humidity of the air and the ability to dry at 'room temperature'. Generally, a slow drying rate minimises the risk of drying defects, which calls for a well controlled drying environment. [57]. Drying too quickly results in deformations such as mud cracks, crow's foot cracks, or orange peel deformation [35].

2.2 Degradation in SOFCs and SOEs

SOCs not only have to be thermally and mechanically stable at high temperatures, but also have a certain tolerance to poisoning, be able to withstand certain levels of thermal cycling and possibly re-oxidation. It is important to understand how degradation mechanisms work and under what conditions they are prevalent so as to avoid them and increase the lifetime of the SOCs. This section will discuss the key degradation mechanisms that occur during electrochemical testing and how the materials, temperature, humidity, current density, and fuel composition affect cell performance and stability.

When comparing the literature on SOFCs and SOEs it becomes clear that much more research has gone into SOFCs than SOEs, meaning when interest grew in SOEs, initially, the same materials were used without considering the different requirements for fuel cell and electrolyser mode. This resulted in much higher degradation rates in electrolyser mode than fuel cell mode, seen by an increased area specific resistance (ASR), and delamination of the oxygen electrode [58–60].

2.2.1 Deactivation of the Fuel Electrode

One of the great advantages SOCs have over lower temperature cells is their ability to oxidise a variety of fuels; hydrogen, carbon dioxide, natural gas, etc. This makes them applicable to a wide range of industries such as the steel industry, gasification plants, pyrolysis plants, or anywhere that produces large amounts of exhaust H_2 and CO. However, running SOFCs on hydrocarbon fuels means fuel electrodes are susceptible to poisoning from contaminants in the fuel such as sulphur. Sulphur is found in small quantities in natural gas, biogas and other methane-containing fuels. In addition to contaminants in the fuel supply, other contaminants

include silicon, which originates in the glass sealant typically used to ensure gas tightness, and chromium, which originates in the stainless steel interconnects used in stacks. All of these impurities can be found on the ppb and ppm scale, and if left to build up, can deactivate the cell.

Carbon deposition, or coking, can occur on the fuel electrode when using carbonaceous fuels such as CH_4, CO_2 or CO. Whilst it is not considered a contaminant, carbon deposition can have the same negative affects as the previously mentioned contaminants, by building up and blocking TPBs until the cell deactivates. This section will discuss the effects these contaminants and coking have on the fuel electrode.

2.2.1.1 Sulphur Poisoning

Sulphur is present in small quantities in almost all hydrocarbon fuels, usually as H_2S, and Ni is particularly sensitive to sulphur. Sulphur poisoning causes a decrease in cell voltage and an increased polarisation resistance and can be identified by two phases of degradation: at first there is a rapid performance loss over a short period of time, this is then followed by a more gradual degradation [61, 62]. The extent of sulphur poisoning is dependent on sulphur concentration, operating temperature, cell voltage and current density, and can have both reversible and irreversible contributions [63].

Work by Tokyo Gas in 2000 revealed that performance loss due to sulphur poisoning increased with decreasing temperature, and is governed by total sulphur content rather than partial pressure [63]. This is agreed by Cheng et al.[64], who detected sulphur on the Ni surface at temperatures below 500ºC and none on cells operated between 500 to 800ºC. In another paper by the same authors, they argue that in order to assess the degree of sulphur poisoning accurately, we must look at anode polarisation resistance, not power output as previously thought [65]. Ebbesen et al. [66] carried out H_2O, CO_2 and co-electrolysis tests on Ni-YSZ and revealed

a significant performance improvement after simply cleaning the inlet gases, revealing the high sensitivity of these cells to impurities. Skafte et al. [67] tested similar cells in CO_2 electrolysis and found that sulphur poisoning would occur at ppb levels during CO_2 electrolysis, whereas in fuel cell mode, the sensitivity changed to ppm levels.

Several authors have shown how the use of Ni-ScCeSZ as electrolyte and/or component in the anode produces higher tolerance to H_2S than with Ni-YSZ cells, even when exposed to higher concentrations and for an extended period of time [62, 68]. One method of removing these impurities is to operate at high current densities, and therefore produce more water, which apparently facilitates removal of small quantities of sulphur [69].

2.2.1.2 Silicon Poisoning

Silicon impurities can originate from externally applied glass sealant or as a contaminant in the electrode and electrolyte material. It forms insulating phases at electrolyte grain boundaries, resulting in reduced conductivity and poor electrochemical performance. Hauch et al. [70] have investigated how silicon deposition onto the fuel electrode caused a degradation of 2%/1000 hrs during long-term (1316 h) electrolysis testing, but interestingly, this could be partly reversed by changing to fuel cell mode. In another study, Hauch et al.[66] found silicon was contained to the fuel electrode and the surrounding innermost microns, but it is when the impurities migrate to the TPBs that a drop in performance is seen. They speculated that in SOE mode, the driving force of the impurities is towards the TPB whereas in fuel cell mode the driving force is away from the TPB, which explains the more detrimental effect in SOE mode. Interestingly, and in direct contrast to expectations, it has been found that the doping of LSCF with silicon to make $La_{0.6}Sr_{0.4}Co_{0.8(1-x)}Fe_{0.2(1-x)}Si_xO_{3-\delta}$ largely improves the conductivity. It is thought that the adverse effects of silicon are due to its being a secondary phase, rather than when it is

incorporated into the perovskite structure [71].

2.2.1.3 Chromium Poisoning

Chromium contamination [72] originates from the stainless steel interconnects in between cells within an SOFC stack. In order to reduce the effect of these impurities, coatings such as manganese cobalt spinel oxide (MCO) have been applied to the interconnects [73]. In 2010, Sohal et al.[74] showed how the movement of chromium changes depending on the operational mode: fuel cell or electrolyser mode. This is due to the change in direction of oxygen movement at the electrolyte-electrode boundary. In another publication regarding chromium, it was highlighted how chromium poisoning occurs to a lesser extent in SOE mode than it does in SOFC mode [75].

2.2.2 Delamination of the Oxygen Electrode

The term delamination describes the physical separation of the oxygen electrode from the electrolyte, and is usually observed in electrolysis mode. One of the more widely accepted understandings of the degradation mechanism at the oxygen electrode is Virkar's [76], which explains how high internal oxygen partial pressure at the oxygen electrode-electrolyte boundary can cause stress in the microstructure, micro-cracks and eventually, full delamination of the electrode. Virkar suggests introducing some electronic conductivity to the electrolyte, such as ceria, to limit this increase of pressure, meaning that traditional materials for electrolytes such as YSZ may not be the best for use in SOE.

Materials such as LSM [77–79], lanthanum strontium ferrites (LSF) [77, 78], LSCF [78, 80, 81], and LSC [80] have been investigated extensively for their resistance to delamination. In 2007, the U.S. Department of Energy (DoE) commissioned extensive tests on LSCF, LSF

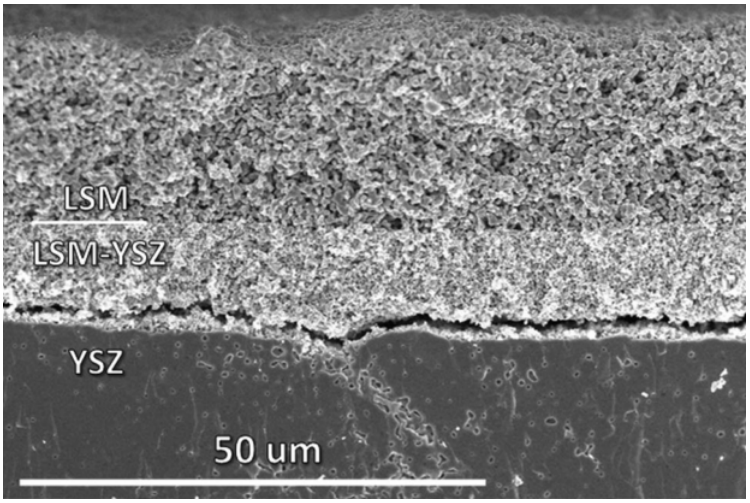


Figure 2.7: SEM micrograph of extensive delamination along the electrode-elecrolyte boundary [77].

and LSM/YSZ for reversible operation, and found that LSCF was most appropriate for rSOC due to its stability in both modes. They also investigated microstructure and found thinner electrodes made from smaller particles performed better than thicker electrode layers, reducing the electrolysis degradation from 8000 to 200 mΩcm ^{2}/1000 hrs. Ultimately, this DoE project demonstrated a 10-cell rSOC stack which operated over 1000 hours in alternating mode [78]. In another attempt to reduce delamination further, Vibhu et al. [82] infiltrated LSCF with LSC to increase the ionic conductivity in the electrode-electrolyte region. This resulted in a reduced polarisation resistance and no delamination after two weeks of operation for the infiltrated electrode, whereas the LSCF reference cell did present some delamination. They speculated that the addition of LSC modified the microstructure and facilitated the movement of oxide ions at the electrode/electrolyte interface.

Researchers at EIfER have done extensive research on SOE since 2004, in particular looking at LSM and LSCF electrode materials in cells and short stacks. Early publications show interest in LSM-YSZ electrode material [83], then 2010 sees the first use of LSCF in a comparative study against LSM-YSZ in short stacks from Risø and ECN [84], work that illustrates the

compatibility of composite air electrodes in comparison to MIEC materials. By 2012, EIfER were using Ni-YSZ/YSZ/LSCF ASCs from Jülich, a cell that reached a lifetime of over 9000 h with no sign of delamination [85, 86].

Researchers have all agreed that in order to preserve materials, focus must be on process optimisation and microstructure, for example developing a composite electrode [70], utilising a MIEC such as LSCF [87], using nanoparticles that act as superoxide ion conductors (nano-GDC) or oxygen diffusion promoters (such as Pd) to reduce oxygen partial pressure build-up [88, 89]. Due to the MIEC properties of LSCF, the region of oxygen reduction is extended through the electrode, which improves the ORR kinetics at lower temperatures (less than 800ºC), making them ideal materials for intermediate temperature solid oxide fuel cells (IT-SOFC) [90]. Furthermore, this larger reaction area reduces oxygen pressure at the interface, making LSCF more resistant to delamination than purely electronic conducting electrodes [91]. The ability of LSCF to perform well at low temperatures and its resistance to delamination determined its selection as an oxygen electrode material in this thesis.

2.2.3 Redox Stability

SOC stacks are expected to experience between 25 and 100 reduction and oxidation (redox) cycles throughout their lifetime due to system failures or high fuel utilisation. With each cycle comes the expansion and contraction of the Ni oxidising to NiO and reducing to Ni metal again [92]. Over a period of time these thermomechanical stresses cause irreversible, microstructural damage which leads to cracks, gas leakage and in some cases, total cell failure [93].

According to Klemensø et al. [92], redox stable fuel electrodes must have ceramic network strength and must restrict Ni relocation and coarsening. It is the re-oxidation of the Ni that results in a change in volume compared to the original reduced state, which in turn introduces

local stresses. Researchers at UCL have recently managed to quantify the damage done by redox cycling by investigating the Young's modulus, hardness and TPB density. After 20 cycles, a Ni-YSZ cell TPB density diminished from 4.63 μm^{-2} to 1.06 μm^{-2} [94]. Interestingly, the electrode polarisation resistance decreased systematically after each re-reduction due to transient Ni nanoparticles, however, Ni agglomeration dominated, causing an overall increase in polarisation resistance, increased pore size and fractures.

Several attempts have been made to alleviate the effects of redox cycles on SOCs. Waldbillig et al. [95] tested the redox stability of SOFCs and concluded that cells made with coarser microstructure experienced no cracking upon redox cycling, whereas the finer structured samples expanded after oxidation, resulting in cracks. They also found that reducing the Ni content, whilst staying within the percolation threshold, decreased volume expansion for the finer structured cells, confirming the link between Ni content and stability.

Grahl-Madsen et al. [96] investigated the electrical conductivity of Ni-YSZ cells reduced at different temperatures and their stability to redox cycling. They found the relationship between reduction temperature and conductivity was almost linear, and speculated that at the higher temperature the newly formed Ni was redistributed to form a continuous Ni network, improving the electrical conductivity and also the redox stability.

The redox of Ni in the fuel electrode can lead to significant microstructural changes, ultimately leading to a drop in performance. The types of microstructural changes and the conditions where they develop are outlined in the following section.

2.2.4 Material Transport Mechanisms

There are three main phenomena which describe the change of morphology of the Ni in the fuel electrode at high temperatures; nickel coarsening, Ostwald ripening, and agglomeration.

Coarsening is inherent to high-temperature sintering, and is identified by a change in surface morphology of the grains via simultaneous grain growth and reduction in the number of grains, while the total grain volume remains unchanged [97]. This increase in grain size decreases surface area and TPB sites, causing polarisation resistances to increase [98]. Ostwald ripening is the process by which, over time, smaller particles, in this case, Ni, migrate and redeposit onto larger particles due to the smaller particles having higher surface energy, and therefore higher Gibbs energy, than the larger particles [99]. Agglomeration is the process when Ni particles cluster together to form fewer, larger Ni particles, ultimately disrupting the Ni-Ni network and decreasing the electrical conductivity. These mechanisms are highly dependant on process parameters such as temperature, humidity and microstructure. Figure 2.8 shows SEM micrographs of an SOFC after long-term operation. The Ni is seen to be agglomerating as the duration of the tests go on, with the final image at 20,000 h showing that the Ni migrates away from the electrolyte/fuel electrode boundary until the Ni network is broken [100].

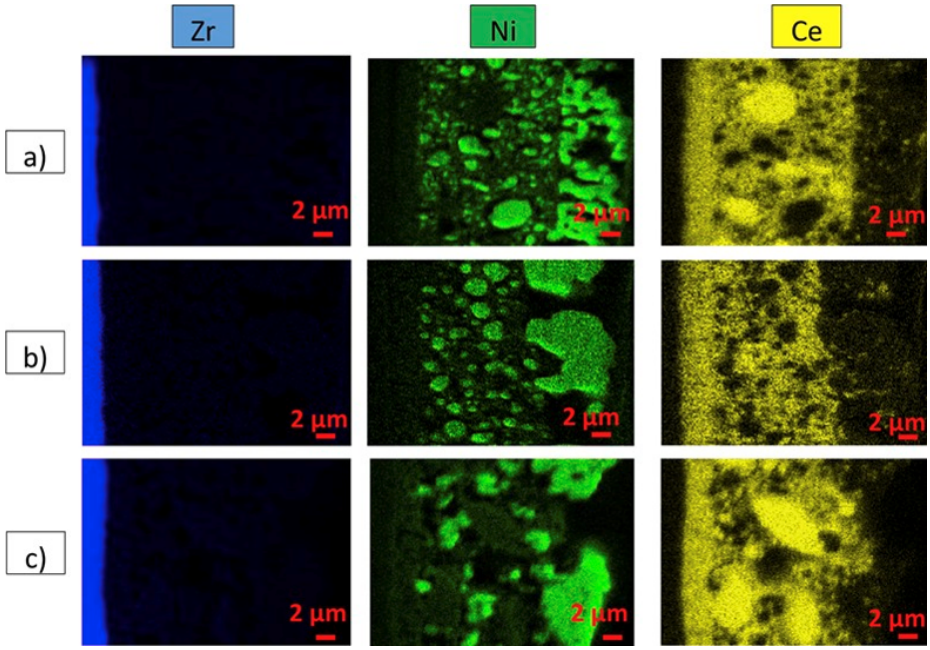


Figure 2.8: EDX mapping of Zr, Ni and Ce after (a) 2,500 h, (b) 15,000 h and (c) 20,000 h of operation showing Ni depletion [100].

Holzer et al. [101] tested the effects of both humid and dry H_2 on Ni grain growth and migration in SOFCs. In humid (60 vol% H_2O) fuel, Ni had a growth rate of 140%/100 h, whereas in dry H_2 fuel the growth rates were only 1%/100 h. They comment on the Ni coarsening being the dominant degradation mechanism, however, in humidified fuel the evaporation of volatile Ni species ($Ni(OH)_2$) leads to Ni reorganisation, with some areas enriched and others depleted. Early work by Gubner et al. [102] provides strong evidence to suggest the concentration of volatile $Ni(OH)_2$ species is proportional to the O_2 activity in the fuel and increasing temperature.

When it comes to SOEs, typical conditions are high steam partial pressure and high temperatures, which are perfect conditions for Ni migration and coarsening. Without changing the material completely, controlling the electrode stability of SOEs tends to result in microstructure alterations. In 2016, Hauch et al. [103] presented work which contradicts earlier findings; the cells that were most resistant to Ni migration had finer, denser structures and well dispersed and size matched particle size distributions. It seems clear that there is an optimal microstructure, Ni content and fuel composition for SOFCs and a different optimal microstructure, Ni content and fuel composition for SOEs, which means there must be a middle ground which suits both operation modes. The author suspects it would tend to a slightly lower Ni content, in alignment with Klemensø's work [92], seeing as the degradation caused in electrolysis mode is more severe and dominant.

2.2.5 Carbon Deposition

One of the drawbacks to using hydrocarbon fuels is that Ni, which is present in the fuel electrode, catalyses carbon formation via the Boudouard reaction under certain conditions (Equation. 2.2). Carbon growth comes in the form of either carbon fibres, amorphous carbon or

graphite [104]. The carbon deposits onto the Ni surface, coating and deactivating it by blocking the TPB sites. There are two widely accepted carbon forming mechanisms; the solid catalysed reaction and the gas-phase pyrolysis. The former produces filamentous carbon, and the latter produces the graphitic form. Filamentous carbon has been attributed to causing internal stresses and, eventually, cracking, whereas the graphitic carbon is formed on the surface of the Ni, not leading to destruction of the Ni network [105]. The carbon groups can be removed by oxidising them with O_2, H_2O or CO_2 but this can also lead to formation of carbon clusters [106]. Continual build-up of carbon, or 'coking', will eventually deactivate the whole cell by by blocking the surface of the catalyst. In order to efficiently use carbonaceous fuels in SOFCs, it is vital that new materials, or moderated materials, with higher tolerance to carbon replace the conventional Ni-YSZ [43].

$$CH_4 \longrightarrow C + 2H_2 \tag{2.1}$$

$$2CO \longrightarrow CO_2 + C \tag{2.2}$$

$$H_2 + CO \longrightarrow C + H_2O \tag{2.3}$$

Possible carbon-forming reactions that take place within SOCs are methane cracking (Equation. 2.1), the Boudouard reaction (Equation. 2.2) and the reverse coal-gas reaction (Equation. 2.3). The Boudouard reaction is an exothermic reaction. However, due to its reduction in entropy, the carbon producing reaction becomes more favourable at lower temperatures.

Carbon can be deposited when certain thermodynamic conditions are met. These conditions include reduced temperatures and higher carbon/oxygen ratios. Ternary phase diagrams (such as the one in Figure 2.9) are often used to illustrate where this carbon forming 'window' is, and are useful indicators for the operational regions that will avoid carbon deposition. Current

research surrounding the reduction of operating temperature down to 500ºC, for benefits in degradation and cost, means that modern SOCs will be more vulnerable to carbon deposition via the Boudouard reaction. Therefore, it is important to incorporate effective intermediate and low-temperature materials for use in SOCs to enable the conversion of electricity into competitive, CO_2 neutral fuels, and vice versa [107].

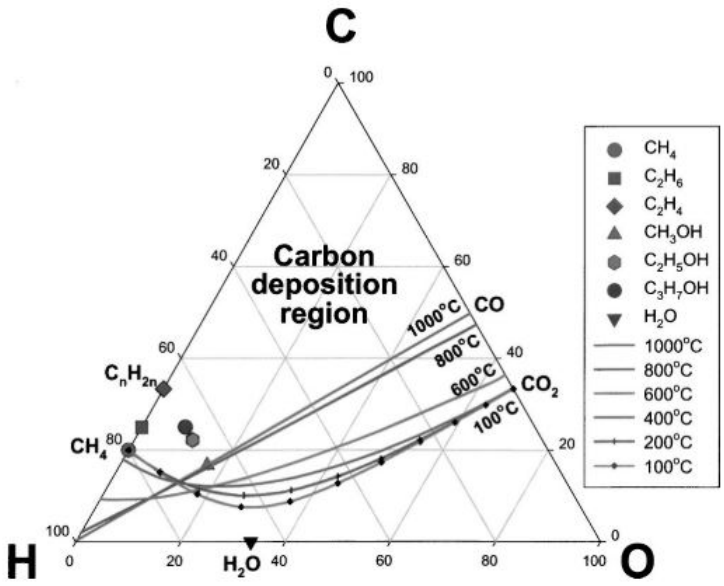


Figure 2.9: Carbon deposition limits in the C-H-O ternary diagram [108]

There are numerous ways to adapt the fuel electrode to combat coking; surface modification [109–111], alloying [112], and substitution and doping [113, 114], to name but a few. Despite all this, there is also research suggesting how conventional fuel electrode-supported Ni-YSZ cells can be operated directly with humidified methane and natural gas, to produce high power densities with no carbon deposition [115]. These researchers state there is a narrow window of temperature in which carbon can be removed, a method that was proved in the laboratory, however may not be practical upon scale up.

Interest has grown in the suitability of barium oxides, specifically $BaZrO_3$ (BZY), and $BaZr_{0.1}Ce_{0.7}Y_{0.1}Yb_{0.1}O_3$ (BZCYYb) [109–111] for surface modification of Ni. Similarly, the

alloying of metals such as Au to Ni increases the coordination number of adjacent Ni atoms, which lowers the surface energy of the Ni for methane processing [112]. Rh or Sn have also been proven to hinder the formation of C-C and C-O bonds in this way [113, 114].

A different method is to completely substitute the Ni for Cu or MEIC based anodes. This has proven to minimise carbon formation, however these materials still suffer from low mechanical strength, poor activity towards hydrogen oxidation, and unsuitable TEC [116, 117]. He et al. [118] demonstrated the use of Cu-CeO_2 fuel electrodes as having an added benefit to their carbon tolerance: superior sulphur-tolerance.

In alignment with doping strategies, Ni-ScCeSZ fuel electrodes have been proven to reduce coking when using hydrocarbon-based fuels. Ceria-doped scandia-stabilised zirconia (ScCeSZ) cermet fuel electrodes have gained in interest for IT-SOFCs due to their increased ionic conductivity at lower temperatures, and tolerance to carbon and sulphur [40, 104, 119, 120]. Upon heating, the conductive cubic phase of SSZ transforms to the less conductive rhombohedral phase unless 1% of CeO_2 is added, giving the more stable ScCeSZ [121]. The larger ionic size of Ce^{4+} (0.97 Å) compared to Zr^{3+} (0.84 Å), stabilises the the cubic fluorite structure, and reduces the tendency to transform into low symmetry phases at elevated temperatures [122]. XRD scans of both SSZ and ScCeSZ are shown in Figure 2.10, showing the rhombohedral peaks for SSZ and cubic for ScCeSZ. (λ = 1.5406 Å).

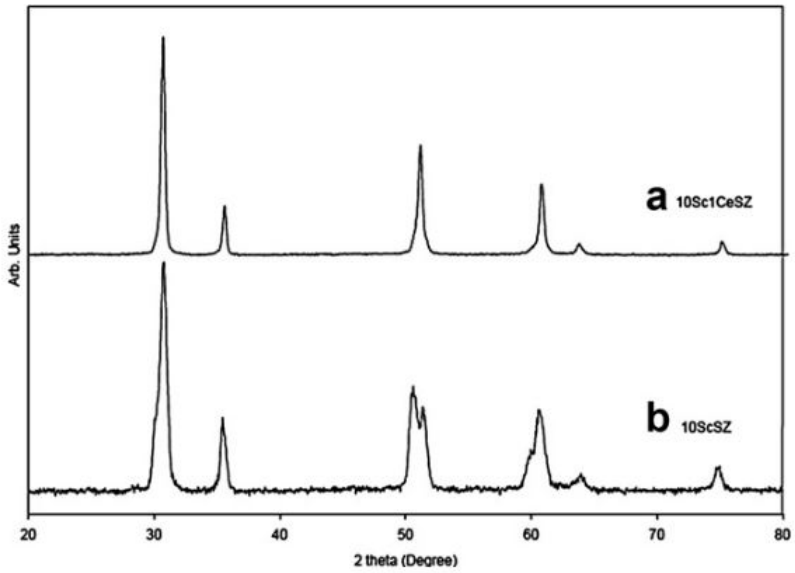


Figure 2.10: XRD patterns of (a) 10Sc1CeSZ and (b) 10ScSZ [40].

Much of the research surrounding carbon formation and Ni-ScCeSZ electrodes comes from Sumi et al.[104] from Kyoto University. In 2004, this group compared Ni-YSZ and Ni-ScCeSZ in humidified methane at low steam/carbon ratio for 250 h. The Ni-ScCeSZ cells had no performance degradation and post-mortem analysis revealed some surface graphite, whereas the Ni-YSZ cells showed significant degradation and amorphous carbon was found on the Ni particles. In similar work in 2011, Somalu et al. [40] compared the ability of Ni-ScCeSZ cells and Ni-YSZ cells to resist carbon deposition, showing that at a high steam/carbon ratio of 0.8 the Ni-ScCeSZ cells had the best electronic conductivity, polarisation resistance and lowest amount of deposited carbon (the ratio, mg-carbon / mg-catalyst x 100, of deposited carbon was 0.28 % for Ni-ScCeSZ cells compared to 0.35 % for Ni-YSZ cells). It has also been shown that ScCeSZ is stable and performs well as an electrolyte when used in SOEs [123]. Whilst a fair amount of research on the use of Ni-ScCeSZ in SOFCs is available in the literature, its high cost is the main reason it is not used in industry or extensively within the research community [107]. However, there is the argument of decreasing price with increasing use and interest in

the material.

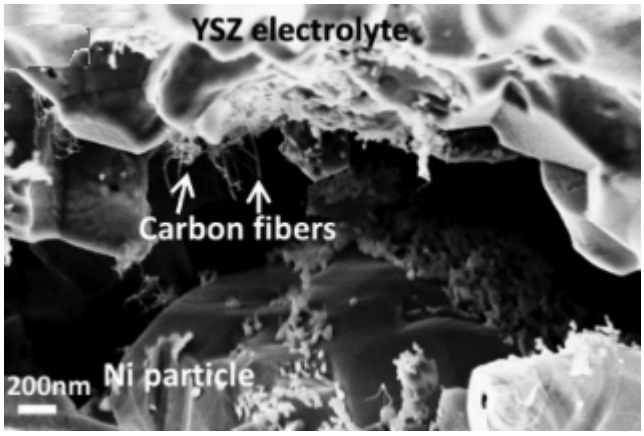


Figure 2.11: SEM micrograph of the interface between a Ni particle and the YSZ electrolyte, where filamentous carbon has formed [124].

In 2008, Pomfret et al.[125] demonstrated the ability to use in-situ Raman spectroscopy to identify the types of carbon and characterise graphite formation. They concluded that of the three fuels they tested (methane, ethylene and propylene), methane forms small amounts of highly ordered graphite that has little impact on cell performance. It is the disordered carbon deposits from ethylene and propylene that cause detrimental electrochemical performance. Chen et al. [126] also identified different types of carbon formation; filamentous carbon was deposited when a Ni-YSZ cell operated between 400 and 600 ºC, and when the temperature increased to 700 to 800 ºC, flake carbon formed. Sumi et al.[119] recognised that after re-reduction of the Ni-ScCeSZ fuel electrode, new, finer Ni particles had been deposited around the original Ni grains and it was from these new Ni particles that the carbon deposition occurred. Further analysis revealed that different types of deposited carbon have different oxidation behaviour, due to the morphology and crystallinity.

Several researchers have pointed to the relationship between carbon deposition and oxide species. In 2011, Yoshinaga et al. [127] carried out Raman spectroscopy on Ni-YSZ, Ni-

ScCeSZ and Ni-GDC cells after carbon treatment. Graphite deposits were found on Ni-YSZ and, to a lesser extent, Ni-ScCeSZ, however none were found on Ni-GDC. They speculated that more water might be generated on the Ni-GDC, mitigating carbon deposits, but nothing was confirmed. This could be the same reasoning behind the carbon tolerance of Ni-ScCeSZ, however more studies into the conditions when carbon forms are necessary.

2.3 Co-electrolysis in Solid Oxide Cells

The ability to reduce global CO_2 emissions by either capturing the CO_2 or converting it into a more useful material is realised in the process of co-electrolysis. The co-electrolysis reaction (Equation 2.4) describes the simultaneous reduction of H_2O and CO_2 to produce a mixture of H_2 and CO, also known as synthesis gas (syngas). Syngas is a useful synthetic fuel as it can be further processed using Fischer-Tropsch synthesis, can be methanated to produce synthetic natural gas (SNG) or be used in the production of ammonia, methanol and other chemicals [26].

$$CO_2 + H_2O \longrightarrow CO + H_2 + O_2 \tag{2.4}$$

$$H_2O + CO \longrightarrow H_2 + CO_2 \tag{2.5}$$

There are many benefits to using high-temperature SOCs for co-electrolysis, one being the need for only one reactor, whereas in traditional syngas production a separate reactor is necessary for the water gas shift (WGS) reaction (Reaction 2.5) to boost H_2 yield. The production of fuels from CO_2 is more environmentally and economically advantageous than the production of chemicals from CO_2 in terms of volume of CO_2 converted and market share [128]. Furthermore, the syngas can also be used as a fuel to create power in the same SOC in fuel cell mode [129]. Further details on the thermodynamics of co-electrolysis will be outlined in Chapter 5.

2.3.1 Brief history of co-electrolysis

Interest in co-electrolysis began as a way to regenerate oxygen from CO_2 for spacecraft in the 1960s, eliminating the need for large, heavy O_2 tanks on board. In 1978, Ash wrote about using the CO_2-rich atmosphere on Mars in a co-electrolysis reactor to produce O_2 or mixtures of CH_4 and O_2 for propellant [130]. This is still being used today in the MOXIE Mars Rover launched in 2020 [131]. In the early 2000s there was a renewed interest in co-electrolysis, this time for the production of syngas. This was assisted by the drive towards reducing CO_2 emissions and the production of sustainable fuels, which led to an onset of economic feasibility studies and modelling of co-electrolysis reactors [132, 133].

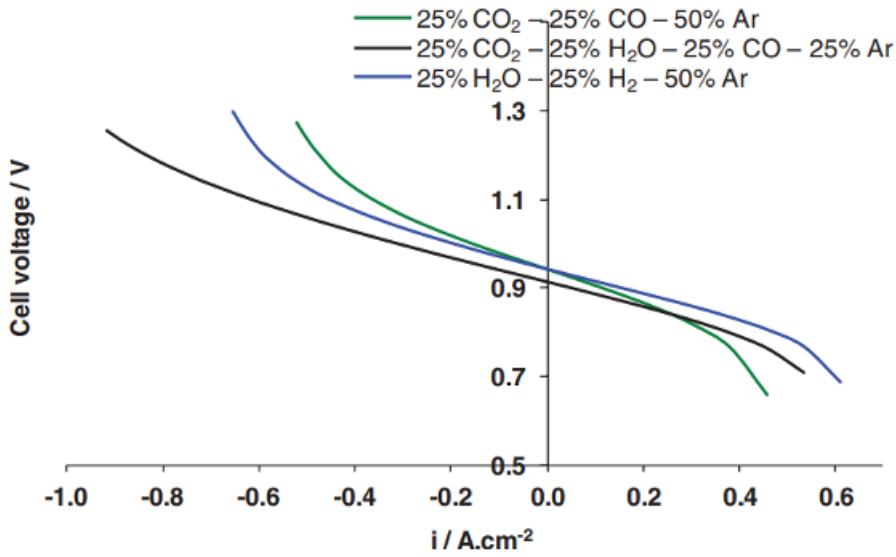


Figure 2.12: Comparison of different i-V curves for co-electrolysis, CO_2 and H_2O electrolysis [134].

Much of the early research was done by the Mogensen group at Risø National Laboratory, who carried out durability tests on NiYSZ/LSM cells over 1000 hours [29]. They showed that these cells could work reversibly in CO_2, H_2O, H_2 (4:4:1) mixtures. At a similar time, Zhan et al. [135] were studying the performance of NiYSZ/GDC-LSCF cells on 25% H_2 25% CO_2 50%

H_2O mixtures. Both of these studies show how the performance of co-electrolysis, in terms of EIS and i-V curves, is closer to that of H_2O electrolysis than CO_2 electrolysis, indicating that the reverse water gas shift (RWGS) reaction is more active than CO_2 electrolysis in producing CO.

2.3.2 Carbon formation in co-electrolysis

Whilst publications on carbon deposition in fuel cells are abundant, and it is thermodynamically possible for carbon to form on the fuel electrode during electrolysis of CO_2 or co-electrolysis of CO_2 and H_2O, carbon build up in rSOC cells and stacks has not been widely reported. It would be expected that any carbon formed during electrolysis operation would oxidise with any available O_2 or H_2O, thus minimising coking risk. However, as the current density is proportional to the O^{2-} flux across the electrolyte according to Faraday's Law, at high current densities a more reducing environment at the fuel electrode may aid in carbon formation.

Carbon formation in co-electrolysis was first observed in 2014 by Tao et al. [124] on Ni-YSZ cells of varying porosity. They found carbon deposits on the cells with denser microstructures after testing at high (2.0 A cm^{-2}) current densities. Similarly, researchers at DTU and Haldor Topsoe [136], created a model to predict carbon formation from the Boudouard reaction during CO_2 and co-electrolysis. Conditions that are favourable for carbon formation are created due to diffusion limitations in the low porosity microstructure, causing high CO concentrations. To the author's knowledge there are no investigations into carbon formation during reversible operation of Ni-ScCeSZ SOCs operating on fuels such as CO_2, H_2O, CO and H_2. Considering that carbon is more likely to form at reduced temperatures, and ScCeSZ is a typical intermediate-temperature material that has carbon resistant properties, it would be interesting to see how a Ni-ScCeSZ/ScCeSZ/GDC-LSCF cell compares to a conventional Ni-

YSZ/YSZ/LGDC-LSCF cell under these co-electrolysis conditions.

2.4 Power-to-Gas Projects using SOCs

The term Power-to-Gas (P2G) comes under the umbrella term Power-to-X, X being either methane, methanol, syngas or other chemicals. It involves the use of renewable electricity to power electrolysers, which run on a variety of fuels to produce the product of interest (H_2, syngas etc.). Wang et al. [137] discussed the thermodynamic performance of different Power-to-X systems, including hydrogen, syngas, methane, methanol and ammonia. Roundtrip efficiency for these systems was ranked methane (47.5%), syngas (43.4%), hydrogen (42.6%), methanol (40.7%) and ammonia (38.6%). Round trip efficiency combined both power-generation efficiency and power-storage efficiency of these reversible systems.

The key requirements for successful scale-up of SOCs are acceptable electrode performance, reversibility, stability, and efficient and stable cyclic operation, in addition to those specified for SOFC/SOE individually [129]. The vast majority of large-scale P2G systems are based on the well-established technology of alkaline electrolysis, which has been used at megawatt scale since the 1940s [138]. The use of solid oxide technology in this area is still considered in its infancy. However, as efficiencies in fuel cell and electrolysis mode increase, degradation rates decrease, and more simulation/modelling data is published, it is becoming a more feasible option for commercial co-generation of power and fuel. These points are identified in two publications from 2018 and 2019, which comment on the mix of technology as approximately half alkaline and the other half PEM electrolysers with only a handful of SOE [139, 140]. Hauch et al.[141] build on this discussion in their review of SOC technology, highlighting the major developments and improvements that SOCs have seen in the past decade. These benefits being more than a double in performance, long-term durability improvement by a factor of 100, as

well as other benefits such as scalable production and integration with downstream synthesis processes.

The capital expenditure (CapEx) for SOC technology is reported at over 2000 \$ $kWel^{-1}$, whereas for larger scale alkaline and PEM systems it is approximately 300 \$ $kWel^{-1}$ and 400 \$ $kWel^{-1}$, respectively[142]. Cost estimates for SOE are expected to reduce with production scale-up over the next 10 years, meaning they will become a more important part of the P2G technology mix. Even though both alkaline and PEM electrolysers have a lower CapEx, and SOE will never be able to compete here, if manufacturers harness the heat from SOE, or pair it with an industrial process, for example use co-electrolysis to produce syngas, a superior efficiency is achievable and SOE benefits can be recognised.

Projects from around the world that incorporate SOC technology in P2G applications are listed chronologically in Table 2.1. Projects are categorised by country or city of location, by commissioning date or project start date, and the size of the SOE or *'n.s.'* ('not stated') if no record was found.

Table 2.1: P2G projects that use SOC technology

Project Name	Location	Start up	Capacity	Reference
MINERVE	France	2013 - 2016	n.s.	[143]
US Navy microgrid	California	2014	50 kW - 400 kW	[20]
HELMETH (FCH-JU)	Germany	2014 - 2018	15 kW	[18]
Power-to-liquids	Dresden	2014	150 kW	[144]
HYPOS rSOC	Germany	2015	180 kW	[140]
BALANCE (FCH-JU)	Europe	2016 - 2019	cell/stack level	[145]
GrInHy (FCH-JU)	Salzgitter	2016 - 2019	150 kW	[146]
Upgraded Biogas	Foulum	2016	50 kW	[147]
H2Mobility	Karlsruhe	2017	n.s.	[148]
CH2P (FCH-JU)	Europe	2017 - 2020	125 kW	[149]
REFLEX (FCH-JU)	Italy	2018 - 2020	120 kW	[21]
Sunfire SYNLINK	Germany	2018	10 kW	[150]
Synfuel	Denmark	2019	n.s.	[151]
GrInHy 2.0 (FCH-JU)	Salzgitter	2020	720 kW	[146]
NewSOC (FCH-JU)	Europe	2020 - 2022	cell/stack level	[152]
E-CO_2Met	Germany	2021 - 2022	1 MW	[153]
MultiPLHY (FCH-JU)	Rotterdam	Projected	2.6 MW	[154]

Seventeen projects were found in six different countries, with the majority of them (nine) located in Germany. The projects found incorporated both laboratory cell and short stack level testing (e.g. BALANCE) to pilot plant demonstrations (e.g. REFLEX and GrInHy) and large scale commercial applications (e.g. US Navy Microgrid). The Fuel Cells and Hydrogen Joint Undertaking (FCH-JU) is a public private partnership that funds collaborative projects on topics covering fuel cells and hydrogen energy technologies within Europe. Eight of the 17 SOC P2G projects are in partnership with the FCH-JU and have been identified in the table, whilst the other 10 have industrial partners, for example Sunfire, Haldor Topsøe and Elcogen.

The FCH-JU project GrInHy 2.0 was a follow-on project from GrInHy, and had aims to increase the electrical power input from 150 kW to 720 kW, and to have been in operation for at

least 13,000 hours. Although it didn't quite reach the 13,000 h system operating hours, GrInHy came to a successful conclusion at the end of 2022 and managed to reach a record breaking 84 $\%\text{el}_{LHV}$ (corresponding to an energy requirement of only 39.7 $\text{kWh/kg}H_2$).

NewSOC is another FCH-JU project, however at a smaller scale utilising large cells and short stacks in close collaboration with industry. The project aims to improve performance, durability, and cost competitiveness by addressing twelve different concepts. This project has links to the work carried out in this thesis, as it focuses on manufacturing techniques of materials that have a large potential for improvement, and rSOC operation rather than SOFC operation.

Sunfire's latest projects, E-CO_2Met and MultiPLHY, which are both megawatt-scale high-temperature electrolysers, in partnership with Total in Eastern Germany and Neste in Rotterdam, respectively. Currently, MultiPLHY is entering commissioning phase and when fully operational, will be the world's first multi-megawatt scale SOE.

2.5 The First rSOCs

By combining SOFC and SOE technology it is possible to make a reversible solid oxide cell (rSOC) that is able to produce power and fuel in one system and is capable of connecting to the grid, switching from electrolysis to power production and vice versa, depending on load and grid fluctuations. rSOCs demonstrate high efficiencies when the heat produced in fuel cell mode is recovered in electrolyser mode. This section will discuss how to optimise SOCs for reversible operation, looking at the degradation, techniques used to slow down degradation, and optimal materials for specific rSOC use.

Whilst the early research on low-temperature fuel cells and electrolysers gained momentum in the 1950s, the first publications concerning reversible operation of solid oxide cells only emerged at the beginning of the 1980s. In 1981, Isenberg from Westinghouse Electric demon-

strated the ability of fuel cells and electrolysers in one co-generation systems, using tubular cells to overcome the steep temperature gradients [155]. This was swiftly followed by similar publications in Germany in 1985 from Dornier GmbH and Lurgi GmbH [156–158]. The first patent regarding reversible operation of solid oxide cells came from Hsu at MIT in 1984 who later founded Ztek Corporation, manufacturing SOFC stacks [159]. NASA showed some early interest in rSOC, publishing a system design of an rSOC coupled with photovoltaics in 1987 [160]. Early research surrounding rSOCs was based on electrode supported geometries with power densities at approximately 0.24 Wcm^{-2}. Research moved on to increasing the power density by reducing electrode polarisation, minimising the thickness of the electrolyte, and optimising ceramic processing techniques to reduce costs [157].

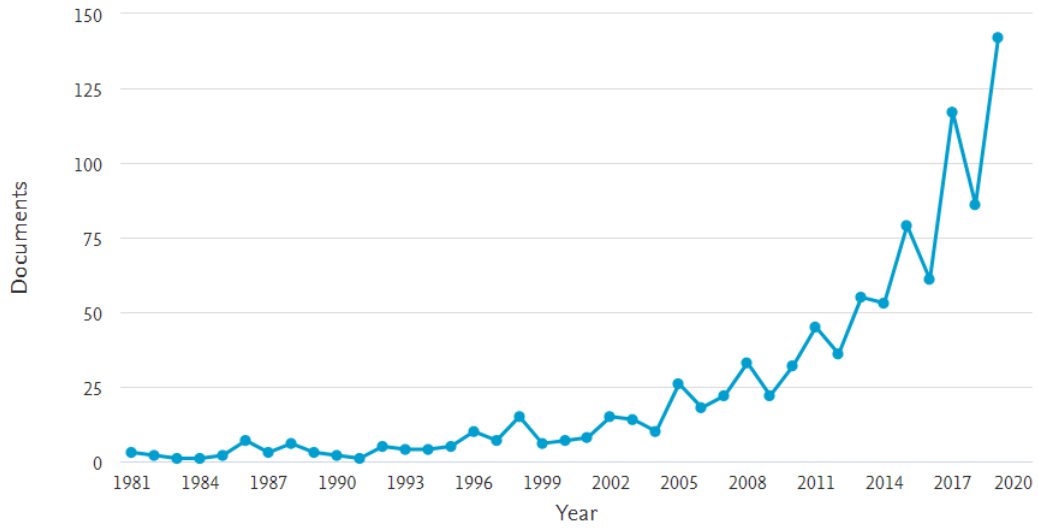


Figure 2.13: The trend of published work on rSOC over the past 20 years from the Scopus database.

After this initial peak of research and development, publications diminished until the new millennium, as seen in Figure 2.13, where interest in hydrogen production spiked due to the promise of an idyllic 'hydrogen economy' by the automotive industry and Canadian fuel cell company Ballard Power. However, the inadequate commercialisation of rSOC systems meant

the hype subsided before the technology was ready [161]. Most of the research published around this time was from Risø National Laboratory, Denmark and the U.S. DoE in partnership with National Laboratories, academic institutions and industrial partners. Early research focused on the ability of typical SOFC electrode materials to cope in SOE mode, monitoring degradation in terms of percentage change of voltage over time (%/kh). The main takeaways were that the standard Ni-YSZ electrode was prone to agglomeration in SOE mode, Ni-YSZ wasn't as active in SOE mode compared to SOFC mode, the significant performance degradation in SOE mode due to oxygen electrode deterioration, and the importance of electrode microstructure [70, 162–165].

Techno-economic modelling and analysis of rSOCs was fundamental in the 2010s, with the key research groups in Colorado School of Mines, DTU and the University of St. Andrews. These groups designed electrical energy storage systems that focused on operating conditions to maximise roundtrip efficiency and cell/stack lifetime [23, 166–169]. Two main aspects of rSOC models focus on systems that can either inject H_2 into the gas grid [170] or store H_2 temporarily [171], or more recently, utilise chemical methanation [22]. The general trend of modelling and simulation work is moving onto hydrocarbon reactions such as methanation [22, 172], co-electrolysis of CO_2 and H_2O to produce green syngas [173], CH_4-assisted rSOCs [166] and flexible energy storage technologies [174, 175].

2.5.1 Degradation in rSOC

By the time rSOCs had been conceptualised, it was recognised that the degradation in electrolysis mode dominated the rSOC system. The build-up of oxygen partial pressure leads to the risk of delamination of the electrode and a substantial drop in performance or complete failure. As of 2020, fuel cell degradation rates were approximately <0.1%/kh [176], and electrolysis

had been proven at 0.4%/kh [177]. This difference can be associated with two things: the more severe degradation at the oxygen electrode in electrolysis mode, but also the disproportionate amount of research into overcoming degradation in SOFCs. It was mentioned previously how in the early 1990s research into SOFCs dominated the literature, so it is unsurprising that lower degradation rates were achieved. SOE degradation rates from EIfER in 2012 were at 5%/kh, and more recently this had been reduced down to 0.4%/kh by focusing on optimising the oxygen electrode [177, 178]. If these competitive SOE rates keep decreasing to SOFC levels, we will see a rise in large-scale commercialised rSOC systems within the decade. An echo of this view is seen in the elicitation study by Schmidt et al. [179], in which professionals from academia and industry were interviewed about their thoughts on the future of fuel cells. Some of the experts envisage that SOEC technology could be favoured by 2030, by which time the cost and lifetime of this technology would reach that of PEM and AEC systems. The paper highlights the importance of research and development funding on SOEC systems, as well as PEM and AEC, to facilitate the development of this technology.

2.5.1.1 Current Cycling

It is possible to tackle the degradation and lifetime issues of rSOCs by the usual techniques; optimising microstructure, or modifying materials by doping or alloying, as we have seen in the SOFC and SOE literature. In addition to this, lifetime tests for rSOCs can also involve cycling with periodic changing between SOFC and SOE mode. Current cycling has been used in the literature for durability testing for many years, with some researchers using it for accelerated testing [180], or others demonstrating the significance of periodically reversing the current to slow the degradation process [77]. In 2014, it was shown that electrolysis induced degradation, which was previously thought to be irreversible, can be eliminated by reversing the

current and operating the cell in fuel cell mode. No microstructural damage at the oxygen electrode/electrolyte interface was observed after cycling between electrolysis and fuel cell modes for 1 hour and 5 hours, respectively, for an overall time of 4000 hours [60].

The U.S Navy microgrid project mentioned in Section 2.2.2, demonstrated the largest commercial, fully autonomous hydrogen rSOC system to date. In the associated publication by Mermelstein et al. [20], it is reported that more than 150 full cycles had been tested, showing a slightly higher degradation rate than under steady-state conditions. An average voltage degradation of 0.009% per cycle was calculated with an overall degradation rate of 0.6%/kh. The system has also operated through seven thermal cycles. Similarly, researchers at Jülich have carried out long-term (4,000 h) tests in cyclic operation. They also recorded a 0.6 %/kh degradation rate in fuel cell mode and nearly no degradation at -0.3 Acm^{-2} in electrolysis, which increased with the current density [181]. Both research groups were studying Ni-YSZ/YSZ/LSCF cells.

2.5.1.2 Fuel electrode degradation in rSOC

Instead of using low or no humidity at the fuel electrode to minimise Ni coarsening and agglomeration, rSOCs must be equipped to deal with higher water content in order to reach a reasonable efficiency when in electrolyser mode. Shin et al. [182] studied the effect of humidity on the performance of a fuel electrode-supported SOC. They used varying fuel humidity from 3% up to 70% and found the largest resistance was for the lowest humidity (3%) seen by large mass transport losses. Similarly, Hubert et al. [183] looked into the impact of Ni agglomeration on H_2/H_2O rSOC in a series of tests spanning 1000 to 9000 hours at high temperatures (750 to 850ºC). They theorised that degradation associated with Ni agglomeration and coarsening was approximately 30% of total degradation in fuel cell mode, which decreases to approximately 25% in electrolyser mode. This is in agreement with other similar studies, which reported 18

to 41% degradation due to the fuel electrode [184]. Similarly, Graves et al. [29] studied the oxidation and reduction of mixtures of CO_2, H_2O, H_2 and CO and identified that at low current densities the fuel electrode degradation dominated, whereas at high current densities it was the oxygen electrode.

In 2022, it was shown via EIS and DRT analysis that the major contributing factor towards rSOC degradation was from the charge transfer process at the fuel electrode [185]. This increase in charge transfer resistance indicated that degradation of the Ni-YSZ triple phase boundary had occurred, in the form of nickel agglomeration, loss of Ni-Ni connections or contamination.

rSOCs are still susceptible to the same impurities and contamination that SOFC and SOE are, and there are not many ways to fully mitigate this issue. In addition to cycling benefiting overall degradation, Hauch et al. [70] demonstrated how the degradation that occurred due to silicon poisoning could be partly reversed by operating the cell in fuel cell mode. A few years later, Tang et al. [186], also carrying out research on contaminants, reported <4%/kh in SOE mode with no delamination, no contamination from Cr, and no Ni coarsening after 8,000 hours of reversible testing, conditions which would usually incite this type of degradation.

2.6 Summary

To facilitate the commercialisation of SOCs, and therefore implement more sustainable pathways for chemical manufacturing and energy storage, then the challenges addressed in this literature view need to be considered. Specifically, the degradation rate needs to be reduced for SOE and rSOC systems by investigating different material sets other than the conventional Ni-YSZ, and manufacturing techniques need to be cost effective for short stack and whole systems. In Chapter 4, it will be shown that tape casting is a suitable low-cost technique for manufacturing single cell SOCs, however, this may not be appropriate for larger cells and stacks where

inconsistencies in the tape could be more frequent.

Typical degradation phenomena have been explored, with particular focus on carbon deposition. One of the benefits of high temperature SOCs is their ability to utilise carbonaceous fuels, so focusing research on how to mitigate potential carbon deposition within the fuel electrode will help push this technology to become a legitimate alternative to lower temperature options. One of the challenges that comes with using carbonaceous fuels is identifying the carbon deposition thresholds for that fuel mix, which ultimately provides an acceptable window of operation. This will be discussed further in Chapter 6. Amorphous, graphitic, and fibrous carbon deposits have been described, alongside their operating mechanisms and effects on cell performance. This provided useful information on how different operating temperatures cause different deposits and how some carbon deposits are more destructive than others, which can help design operating schedules for rSOCs to reverse the signs of early carbon deposition.

Mapping SOC research projects across the world has highlighted that there is a growing interest into SOCs and the advantages these large-scale systems can bring especially when paired with industrial processes to boost efficiencies. Many of the early projects were at the cell/stack or few hundred kW scale, whereas more recently we are seeing MW scale electrolysers being commissioned, proving that it is indeed an exciting time to be in this industry.

The focus of rSOCS should be the benefits the technology brings; higher efficiencies and the ability to utilise carbonaceous fuels. This needs to happen in conjunction with more typical research surrounding decreasing degradation to improve lifetime. Once economies of scale comes into play and the cost of SOC reduces, these benefits will be the reason for industries choosing SOCs over other lower temperature technologies.

CHAPTER THREE

METHODOLOGY

This chapter will describe the manufacturing techniques used to produce circular planar fuel electrode supported cells with a diameter of 30 mm, including; powder preparation, tape casting, co-sintering, sintering and ink preparation. All materials, laboratory equipment, test rig set up and characterisation techniques are outlined.

3.1 Material Characterisation

Initial characterisation of the powders confirmed the particle size (d_{50}). It is important to identify the powder properties of the starting materials as they decisively influence the properties of the green tape when tape casting, and consequently the full cell.

3.1.1 Particle Size Analysis

Table 3.1: Particle sizes of the materials used in the manufacturing of Ni-ScCeSZ and Ni-YSZ cells.

Material	**Formula**	**Supplier**	**d_{50} Particle Size (μm)**
NiO	NiO	Hart Materials, UK	0.997 ± 0.0214
10Sc1CeSZ	$(Sc_2O_3)_{0.1}(CeO_2)_{0.01}(ZrO_2)_{0.89}$	DKKK, Japan	0.892 ± 0.0393
8YSZ	$(Y_2O_3)_{0.08}(ZrO_2)_{0.92}$	Tosoh, Japan	1.264 ± 0.0101
GDC	$Gd_{0.1}Ce_{0.9}O_{1.95}$	Fuel Cell Materials, UK	0.768 ± 0.0185
LSCF	$La_{0.6}Sr_{0.4}Fe_{0.8}Co_{0.2}O_{3-\delta}$	Praxair, USA	0.897 ± 0.0193
Tapioca Starch	n/a	Whole Foods, UK	12.82 ± 0.0128

During particle size analysis, a laser beam is passed through the sample holder and as the light passes through the particles in the sample the beam is scattered. An array of detectors measure the intensity of the light scattered at particular angles in order to calculate the size of the particles in the dispersion, using laser diffraction and Mie theory. To get a good representation of the sample, each sample run takes approximately 2000 'snapshots', each taking 1 ms and the average result is reported in a normal distribution [187].

0.25 g of sample powder was mixed with distilled water, three drops of dispersant and agitated in a sonic bath for 15 minutes before being added to the mastersizer's sample holder and dispersion unit. A Malvern Mastersizer 2000 particle sizer was used to determine the average particle sizes (d50) for each of the starting powders. Characterisation of the starting materials is important as it establishes a library of information to track changes in tape manufacturing. Purchasing different batches of powders results in small variations in particle size, which cause a larger effect on slurry preparation and tape manufacturing than mostly expected.

The average particle sizes of NiO, 10Sc1CeSZ, 8YSZ, 10GDC, LSCF and pore former are shown in Table 3.1.

3.1.2 Dilatometry

Dilatometer analysis is a thermo-analytical method that uses a push rod inside a small furnace to measure the changes in sample length or volume as a function of temperature or time. The atmosphere within the Netzsch 402 C push rod dilatometer furnace can be controlled to only allow certain gases. In this work, air was sent through the furnace at 100 mL/min to simulate the sintering process. The shrinkage and expansion behaviour of the materials were examined and the thermal expansion coefficient (TEC) was calculated.

An Al_2O_3 rod of 6 mm diameter and 3 mm length was used as a calibration/reference stan-

dard. To prepare samples, powders were uniaxially pressed at 2 tonnes and held for 2 minutes to form pellets with diameter 6 mm, then sintered and polished to make smooth surfaces free of cracks. To calculate the TEC of each material, the pressed samples were first sintered at 1400ºC using the heating profile shown in Figure 3.3, then the sintered pellets were placed in the dilatometer sample holder and heated from room temperature to 1400ºC at 5 ºC/min in 100 mL/min air. The theoretical alpha value (TEC) was calculated between 25ºC to 800ºC using the initial sample length at room temperature, *L*, and the temperature, *T*, as expressed in Equation 3.1.

$$\alpha = \frac{\left(\frac{\mathrm{dL}}{\mathrm{dT}}\right)}{\mathrm{L}} \tag{3.1}$$

To measure the shrinkage and expansion behaviour of the materials, the pellets were made in the same way as outlined above, but heated to 900ºC for 4 hours. The partially-sintered pellets were then placed in the dilatometer sample holder and heated from room temperature to 1400ºC at 5 ºC/min in 100 mL/min air.

3.2 Reverse Aqueous Tape Casting

To produce a thin green tape, an MTI Corporation Compact Tape Casting Coater (MSK-AFA-III-220) with vacuum chuck and micrometer adjustable doctor blade applicator was used. The speed over the carrier film and the gap height of the doctor blade were variable to allow for different thickness of green tapes. A thin polyester film was placed onto the vacuum chuck and the doctor blade height set and placed on top of the polyester film. To obtain the desired layer, a prepared slurry suspension was dispensed into the applicator and the traverse speed set to facilitate the movement of the applicator across the polyester film, as illustrated in Figure 3.1.

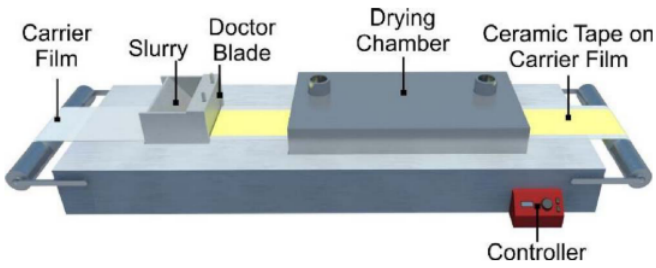


Figure 3.1: Representation of a typical tape casting set up [52].

3.2.1 Slurry Preparation

The cells manufactured and tested in this work were manufactured using NiO (Pi-Kem, UK) and YSZ (Tosoh, Japan), or NiO and ScCeSZ (DKKK, Japan) for the fuel electrode, ScCeSZ or YSZ for the respective electrolyte, and a double layer LSCF-GDC/LSCF (Praxair, USA) oxygen electrode. GDC (Fuel Cell Materials, UK) was used to form a barrier layer between the electrolyte and oxygen electrode. Ni-ScCeSZ cells were manufactured to test their ability using hydrocarbon fuels, and Ni-YSZ cells were manufactured to compare results, as cells made from Ni-YSZ were considered to be a reference material set.



Figure 3.2: The tape casting manufacturing process of fuel electrode supported SOC.

3.2.1.1 Electrolyte and Barrier Layer

The additives used in the electrolyte and barrier layer slurry preparation (binder, dispersant, antifoam, plasticiser) were all purchased from Polymer Innovations, USA. The solvent (water),

dispersant, binder, anti-foam, and plasticiser were mixed together at 120 rpm for 24 hours using spherical and cylindrical ZrO_2 beads. More binder, de-foamer and the corresponding powder (YSZ or ScCeSZ for the electrolyte layer, and GDC for the barrier layer) were added and homogenised for at least 4 h at 120 rpm. To eliminate any air bubbles, the slurries were filtered and degassed for 1h. Layers were tape cast individually, drying each layer in between casting at 60ºC before applying the next layer. The description of all materials, where they were purchased from and their function are listed in Table 3.2.

Table 3.2: Materials and their function for electrolyte, barrier and composite layers.

Material	Function	Composition (wt%)		
		Barrier Layer	Composite Layer	Electrolyte
10Sc1CeSZ or 8YSZ	Ionic phase	-	24.9	49.8
GDC	Barrier layer	49.8	24.9	-
DI water	Solvent	28	28	28
DS001	Dispersant	2.0	2.0	2.0
DF002	Defoamer	0.4	0.4	0.4
PL005	Plasticiser	0.5	0.5	0.5
WB4101	Binder	19.3	19.3	19.3

3.2.1.2 Fuel Electrode Functional Layer and Support

During high-temperature sintering, the green tape becomes more dense as the additives, solvent and binder are burned off, and the cell shrinks in all directions. The NiO layers shrink more than the electrolyte layer, causing concave cell curvature towards the fuel electrode [57]. To reduce this effect, pre-calcining anode powders has previously been used. During pre-calcination, the YSZ or SSZ powders are heat treated to a temperature less than their sintering temperature, which reduces the powder's particle size. This significantly affects the particle microstructure and sintering ability and, in this case, results in reduction of cell curvature. In this work, YSZ

and SSZ were pre-calcined at 800ºC and 900ºC, respectively, for 5 hours. The fuel electrode support cermet consisted of pre-calcined 8YSZ or 10Sc1CeSZ, with as-received NiO powder in a weight ratio of 65:35 (NiO:ceramic).

Solvent (water) and dispersant (Dispex, BASF) were mixed together with the cermet powders and, in the case of the support slurry, tapioca starch pore former (Whole Food Online, UK) was also added, then homogenised at 120 rpm for 24 hours. Binder (PVA, Sigma Aldrich), plasticisers I and II (PEG 400 and glycerol, respectively) and anti-foam (Sigma Aldrich, UK) were added to the slurry and mixed for a further 12 h at 70 rpm. To eliminate any air bubbles, both slurries were filtered and de-gassed in a vacuum desiccator followed by 50 rpm slow-roll for 2 hours to ensure a homogeneous mixture. The functional layer was tape cast onto the electrolyte, dried at 60ºC, then the support was tape cast on top of the dried functional layer and dried for a final time at 30ºC for 24 hours.

Table 3.3: Materials used in manufacturing of fuel electrode layers of SOCs.

Material	Function	Composition (wt%)	
		AFL	AS
NiO	Electronic phase	35.8	35.8
10Sc1CeSZ or 8YSZ	Ionic phase	19.3	19.3
DI Water	Solvent	35.4	29.9
PVA	Binder	4.1	5.4
Dispex Ultra 4404®	Dispersant	1.0	1.0
PEG MW 400	Plasticiser I	2.7	3.45
Glycerol	Plasticiser II	1.4	3.45
Antifoam	Minimise bubbles	0.2	0.2
Tapioca Starch	Pore Former	-	1.5

3.2.2 Spin Coating GDC

For the cells in which the GDC was applied via spin coating rather than tape casting as outlined previously, the following protocol was followed. The half cell consisting of the fuel electrode

and electrolyte was tape cast in the same way as before, and sintered at 1350ºC for ScCeSZ and 1400ºC for YSZ. The sintered half cell was placed into the sample holder within the spin coater, and a micro pipette was used to dispense 200 µl of the GDC slurry onto the electrolyte. One cycle of the spin coater programme was conducted, which involved a rotation at 2500 rpm for 20 seconds, resulting in a deposited layer thickness of 2.80 µm.

3.2.3 Half Cell Assembly

A hydraulic press and metal puncher were used to cut button cells of diameter 40 mm out of the flexible, dried green tape (step four in Figure 3.2). These cells were then placed in a furnace under a 10 g alumina load, and sintered at 1400ºC for four hours with organic burn-off stages at 300ºC and 600ºC, and a dwell stages at 1000ºC and 1200ºC, which minimised the effects of expansion/contraction of the call layers. During sintering, the cells became dense and shrunk to the desired 30 mm. The sintering profile is shown in Figure 3.3.

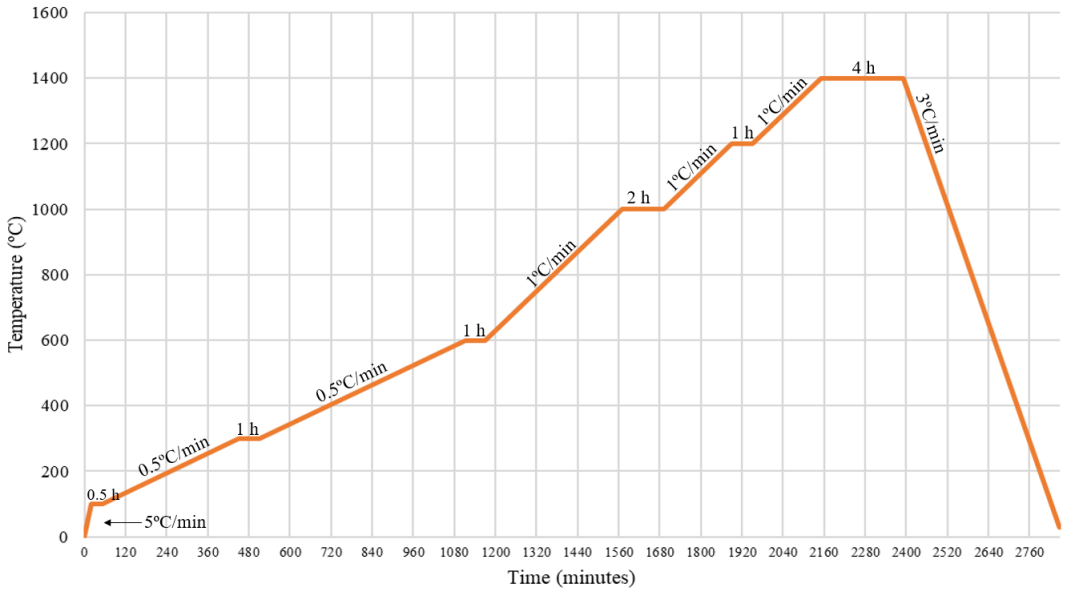


Figure 3.3: Sintering profile for half cells.

3.2.4 Oxygen Electrode Ink Preparation

Ink preparation consisted of mixing powders with the ink vehicle using a three-roll mill machine (Exakt, USA). The composition of the ink is shown in Tables 3.4 and 3.5, and wase adapted from MacDonald et al. [188]. This resulted in solid loadings of 67 wt% for LSCF ink, and 65 vol% for LSCF-GDC ink.

Starting with the oxygen electrode active layer, LSCF-GDC was painted onto the GDC barrier layer, sintered at 1080ºC for three hours at a rate of 3ºC/min with burn-off stages at 300ºC and 600ºC. Next, the LSCF ink was painted onto the dry LSCF-GDC, and sintered at 1080ºC for three hours at a rate of 3ºC/min with burn-off stages at 300ºC and 600ºC. This process resulted in a cell with active area of 3.0 cm^2.

Table 3.4: LSCF ink composition

Material	**Wt.%**
LSCF (Praxair, USA)	65.3
V-737 (Haraeus)	32.7

Table 3.5: LSCF-GDC ink composition

Material	**Wt.%**
LSCF (Praxair, USA)	30.77
GDC (Fuel Cell Materials, UK)	30.77
V-737 (Haraeus)	38.46

3.3 Test Rig Set Up

At the beginning of this project, there was no testing station available that had all of the necessary components to test button cells in both SOFC and SOE mode within the laboratory. As a result, the test rig that was used in this work was designed and built in-house. This included a high-temperature vertical furnace, mass flow controllers (MFC) for gas and water, pre-heaters,

MFC power supply, gas delivery, controlled evaporator mixer (CEM), exhaust system, temperature monitoring system, cell holder, and reactor.

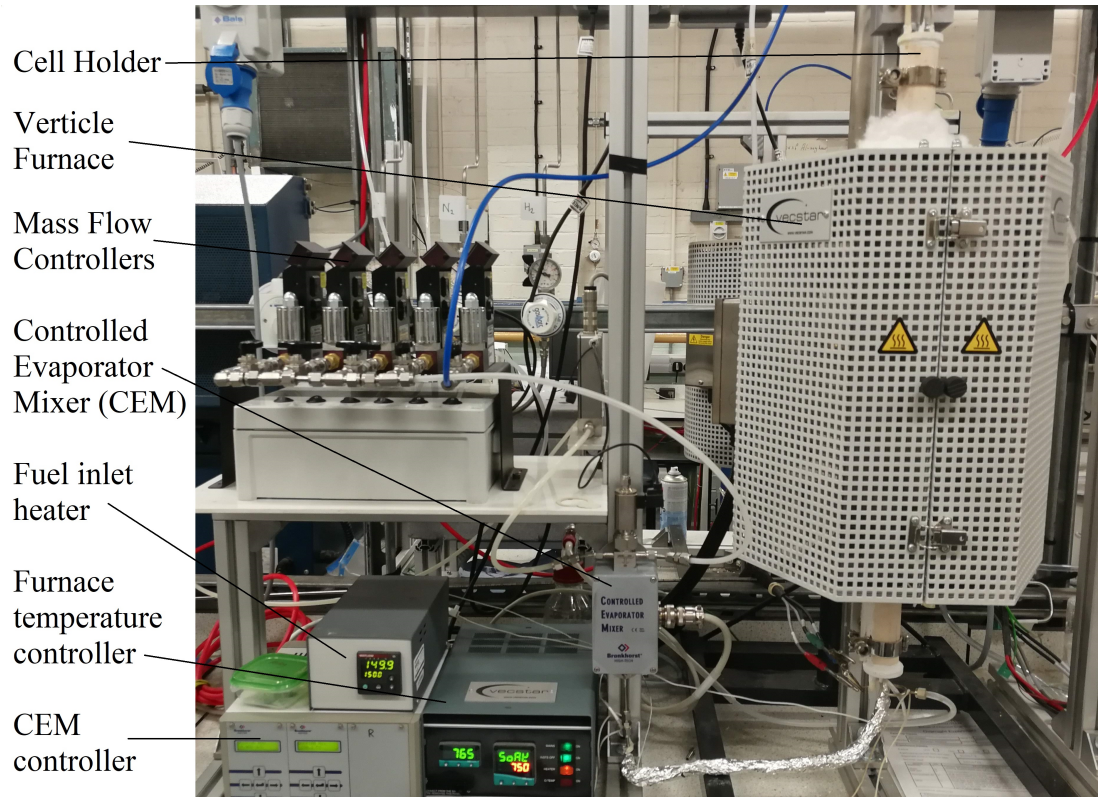


Figure 3.4: Test rig set-up showing all electrical and gas control components.

A common problem encountered with single cell SOC testing is sealing the cell onto the cell holder to ensure a gas tight joint. Any gas crossover due to poor sealing around the edges of the cell results in a reduction in the OCV due to the change in reactant partial pressures, therefore affecting the OCV voltage according to the Nernst equation. A vertical split furnace (Vecstar) was chosen over a horizontal furnace in order to obtain better sealing of the cell, as applying a vertical force is more efficiently done than with a horizontal force. A split furnace was chosen to ensure facile access to the cell holder.

Gold current collector mesh and wire (Fiaxell, Switzerland) were connected to the cell on the electrodes by porous conductive silver paint. The gold mesh design was chosen so to re-

use the current collectors and minimise any changes in contact resistance or resistance of the wires from test to test. Cells were mounted in-between two vertical cylindrical alumina tubes (Pi-Kem, UK) of diameter 40 mm within a macor cell-holder using Thermiculite 870 gaskets (Flexitallic, USA) to seal the cell in place. The alumina tubes were held under load via a spring and weight system to ensure good sealing of the cell holder. Thermiculite 870 is a compression sealing material designed for SOFC and SOE cell testing. The introduction of gas to the cell was via a smaller alumina tube of outside and inside diameter 6.0 mm and 4.0 mm, respectively, held inside the 40 mm diameter alumina tube. The gold wires from the cell were connected to terminals on a Solartron 1247 test station for electrochemical performance measurements.

The cell holder was mounted into a vertical split furnace (Vecstar, UK) and the fuel inlet pipes connected in series via Mass Flow Controllers (Aalborg) to a CEM (Bronkhorst). Any unreacted fuel or by-product was exhausted through a pipe, shown in Fig. 3.5, and vented outside of the laboratory. The air inlet was connected to the top half of the test rig (oxygen electrode) and the lower half was exposed to various gas mixtures; hydrogen, nitrogen, carbon dioxide, or carbon monoxide. The exhaust could also be connected to a Shimazdu Gas Chromatographer GC2014 for analysis of the anode off gas.

Commercial button cells purchased from the Ningbo SOFCMAN Energy Technology Co. Ltd, a spin off company from the Ningbo Institute of Material Technology and Engineering (NIMTE), were purchased and tested on the rig to ensure that all of the components of the test rig were set up correctly and were gas tight.

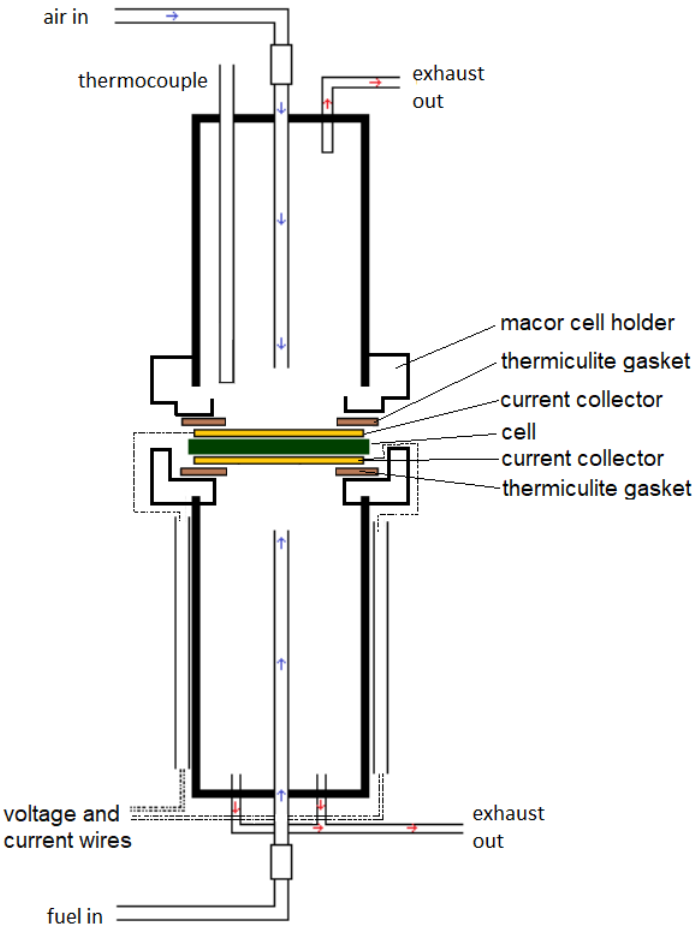


Figure 3.5: Schematic diagram of the cell holder.

3.4 Characterisation

3.4.1 Electrochemical testing

Once the cell was mounted in the cell holder, the furnace temperature was increased to 800ºC at 3ºC/min, then held at this temperature for the reduction of NiO to Ni. Once at 800ºC, N_2 was introduced to the fuel electrode chamber at 10 ml/min to create an inert environment on the fuel electrode. H_2 was then introduced to the fuel electrode in 10 ml/min increments up to 60 ml/min and left for 12 h for the NiO to reduce.

A set of initial tests were run in fuel cell mode to check the cell sealing and performance. This included measuring OCV for 1h, a polarisation curve via a decrease in potential from OCV to 0.4 V and back to OCV, using a step size of 25 mV and a hold time of 60 seconds per step. This was followed by a galvanostatic measurement at OCV for 30 minutes and impedance measurements at OCV using a frequency sweep from 100,000 Hz to 0.01 Hz at an amplitude of 10 mA, with 10 steps per decade.

Cells were electrochemically tested at temperatures from 600ºC to 800ºC in fuel cell and electrolyser mode. The actual temperature of the test rig was measured using a K-type thermocouple placed 2 mm away from the cell, in the alumina cell housing. Each time the temperature was changed, it was held for 2 hours to stabilise before starting measurements. Polarisation curves for electrolysis and co-electrolysis were taken from OCV to 1.6 V and back down to OCV at 25 mV steps with a 60 s hold time at each step. Polarisation curves for rSOC started at OCV, were taken down to 0.4 V, brought up to 1.6 V and back down to OCV. For impedance measurements, the conditions were held for at least 30 minutes before each impedance measurement, to allow for stabilisation. Impedance measurements for rSOC were taken at OCV using a frequency sweep from 100,000 Hz to 0.01 Hz at an amplitude of 10 mA, with 10 steps

per decade.

Table 3.6: Electrochemical testing fuel compositions.

Mode	Gas Flow Rate (ml/min)					
	H_2	H_2O	CO	CO_2	N_2	Air
SOFC	60	0	0	0	10	200
rSOC	60	20	0	0	0	200
	30	30	30	30	0	200

3.4.2 Electrochemical Impedance Spectroscopy (EIS)

The theory of EIS is based on Ohm's Law (Eqn. 3.2) and the electrical resistance found in a circuit, such as an SOC. Ohms law states that the voltage (E) of an electrical circuit is proportional to the current (I) and inversely proportional to the resistance (R). Impedance (Z) is similar to the resistance in Ohms Law, but it is governed by more factors than just the ohmic resistance, and also delivers the phase difference between current, I, and voltage, V, allowing it to identify more complex properties.

$$\mathrm{R} = \frac{\mathrm{E}}{\mathrm{I}} \tag{3.2}$$

EIS works by applying a sinusoidal AC potential or current in a range of frequencies and examining the phase shift and amplitude of the resulting AC current or potential through the cell. Different processes or reactions will be perturbed at different frequencies, allowing for the separation of these processes based on their characteristic time constant and frequency response.

$$\mathrm{Z} = \frac{\mathrm{E}_t}{\mathrm{I}_t} = \frac{\mathrm{E}_0 \sin(\omega \mathrm{t})}{\mathrm{I}_0 \sin(\omega \mathrm{t} + \phi)} = \mathrm{Z}_0 \frac{\sin(\omega \mathrm{t})}{\sin(\omega \mathrm{t} + \phi)} \tag{3.3}$$

Where E_t is the potential at time t, ω is the radial frequency, E_0 is the amplitude of the signal and ϕ is the phase shift of the response signal. The expression for impedance is repre-

sented by a complex number with a real (Z') and imaginary (Z'') component. The plot of Z'' versus Z' is called a Nyquist plot and is commonly used in SOC characterisation to illustrate internal cell resistances. It is important to know that Nyquist plots do not show the corresponding frequency. Bode plots are another way of representing impedance information, in this case showing the frequency dependence. It is common to see both Nyquist and Bode plots presented together. The different reactions or processes that take place within an SOC can be described by

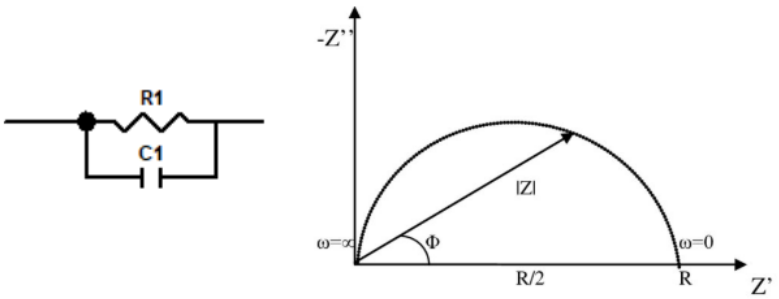


Figure 3.6: Nyquist plot and equivalent RC circuit element

an equivalent circuit model (ECM) consisting of elements such as resistors, capacitors, constant phase elements and inductors combined in series. When an equivalent circuit representing the cell has been established, tools such as complex non-linear least squares (CNLS) are used to fit the ECM and deconvolute the plot to obtain the magnitudes of each of the elements, and therefore each of the internal processes. The types of processes that are modelled include; gas diffusion in the electrodes, electronic charge transfer in the electrodes, ionic charge transfer in the electrodes and electrolyte, O_2 surface exchange kinetics and O^{2-} diffusivity. The Nyquist plot of a singular time constant looks like a semi-circle, as seen in Figure 3.6. This plot is a result of a simple equivalent circuit of an electrode: a capacitor (C1) and resistor (R1) in parallel. Electrochemical impedance plots of SOCs usually contain multiple reactions or processes, ergo multiple time constants, which results in partially overlapping semi-circles in the Nyquist plot,

as seen in the example shown in Figure 3.7. This illustrates how the summation of the magnitudes of all of the processes equate to the overall cell resistance. Each process is described in Table 3.7.

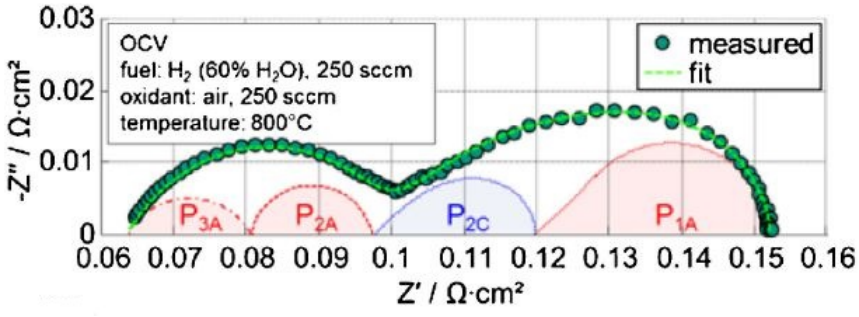


Figure 3.7: Impedance spectrum for an ASC showing the different processes occurring at the fuel electrode (red) and the oxygen electrode (blue) [189].

Table 3.7: CNLS fit of impedance spectrum.

Process	Frequency range	Origin
1C	0.01 to 0.001 Hz	Gas diffusion (only significant in low pp O_2)
2C	5 to 0.01 Hz	O_2 surface exchange kinetics and O^{2-} diffusivity
1A	5 to 50 Hz	Gas diffusion in the fuel electrode
2A and 3A	100 to 10 kHz	Coupled process: gas diffusion coupled with charge transfer and ionic transport

The ohmic resistance (R_s) is taken as the high frequency intercept of the x-axis and includes the ohmic contribution of the electrolyte and electrodes, the contact resistance between the electrodes and electrolyte and the wire connections. The polarisation resistance (R_{pol}) is the difference between the R_s and the low frequency intercept and represents the overall cell resistance.

To measure the total resistance of the cell in this work, EIS measurements using a Solartron 1247 potentiostat were taken at OCV in SOFC and SOE mode. The frequency sweep for each test was from 100,000 Hz to 0.01 Hz at an amplitude of 10 mA. The ECM used to analyse the Nyquist plot by CNLS fitting consisted of an inductor, resistor, two RQ elements (resistor

and constant phase element in parallel) in series, a Gerischer element in series and another RQ element (Figure 3.8). Similar models have been used by other researchers [182, 190].

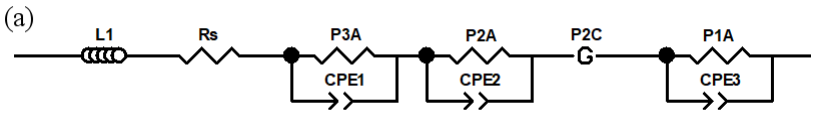


Figure 3.8: Equivalent circuit model used for CNLS fitting of Ni-SSZ and Ni-YSz cell impedance.

The ECM was constructed from referencing models in the literature for similar ASC and by analysing the Distribution of Relaxation Times (DRT). DRT analysis is used in impedance to identify the different processes based on their differing time constants. This will be explained further in Section 3.4.2.1.

3.4.2.1 Distribution of Relaxation Times (DRT)

In order to extract accurate physical quantities from EIS data, the data set must be of high quality, meaning the system must exhibit linearity, stability and causality [191]. A system is linear when the applied AC amplitude is small enough that the measured response is linear. The stability relates to a system which is not changing while the measurement is taking place, and a causal system is one in which the measured AC response is directly related to the applied AC stimulus, with no interference from external sources.

The distribution of relaxation times (DRT) is a technique used to deconvolute complex EIS data to gain further insight into electrical properties of the materials being studied. DRT analysis allows the identification of processes with similar time constants or relaxation frequencies that would otherwise have been overlapped in Nyquist plots. By gathering impedance data whilst changing parameters such as the temperature, fuel and oxygen partial pressures, it is possible to build up a catalogue of information on each process in the DRT, to help identify them as either

anode or cathode processes.

In this work, the DRT is calculated by a Tikhonov regularisation using the free online tool, DRTtools, from the Ciucci group [192]. When using this tool, the input parameters are the frequency range, the real and imaginary values of the impedance, and the chosen analysis options were a Gaussian method of discretisation, a regularisation parameter of $1x10^{-3}$, and a first order regularisation derivative, with inductance data disregarded. The regularisation parameter, γ, determines the smoothness of the DRT. The higher the γ value, the stronger the penalty to the sum of squares for fitting, meaning a smoother DRT profile. Figure 3.9 shows a Nyquist plot for an ASC at OCV, with the four individual processes identified, and the corresponding DRT plot with the same processes identified as peaks with individual frequency responses. In this work, DRT is used to identify the different processes within the cell and to see how degradation affects these processes.

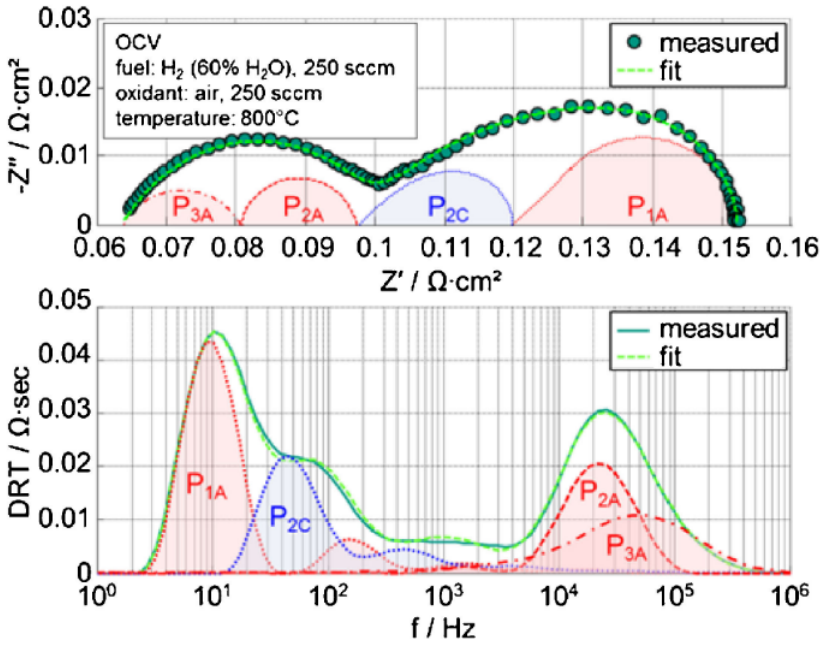


Figure 3.9: The Nyquist plot and DRT of a fuel electrode supported cell showing how the DRT identifies the different processes occurring at the oxygen electrode (blue) and fuel electrode (red) [189].

3.4.3 Scanning Electron Microscopy (SEM)

SEM is a type of electron microscope which uses a beam of electrons to scan the surface of a sample. The electrons interact with the sample and are reflected, either as secondary electrons (SE) or back scattered electrons (BSE), towards detectors which use the information in the reflected electrons to build up an image of the microstructure and morphology of the sample. SE interact with the sample surface and contain topographic information, whereas BSE interact with the sample atom nucleus and contain atomic information which is used to show elemental contrast. Samples were either mounted on a support or held in epoxy resin and both the BSE and SE were detected. In this work, SEM was used to analyse the microstructure of manufactured cells, measure the thickness of each tape cast layer, and identify any deposits of carbon on the fuel electrode-electrolyte interface on cells tested with carbonaceous fuels.

A subsection of SEM is energy dispersive X-ray (EDX) or energy dispersive spectroscopy (EDS). When bombarded with electrons, the material in question can emit X-rays that are characteristic of that element, meaning elemental identification is possible. In this work EDX was used to confirm the elemental distribution in layers after manufacturing, to identify carbon deposits, and to monitor any elemental diffusion after testing at high temperatures.

Two microscopes were used for SEM anaylsis, a Hitachi Table Top TM3030Plus and a Philips XL-30 for higher resolutions. The EDX software used was QUANTAX and INCA for the Hitachi and Philips SEM, respectively.

3.4.4 X-Ray Diffraction (XRD)

In XRD, a sample is bombarded with X-rays and a detector measures the diffracted X-rays at different angles of 2θ around the sample. The X-ray pattern produced by the sample are

characteristic of the crystal lattice structures present in the sample, so XRD can be used to identify different phases within the crystal by comparison with XRD libraries. XRD data was collected on a Bruker D2 diffractometer fitted with a Co radiation source (λ = 1.5406 Å). Diffraction was conducted between a 2θ of 20º and 100º. To identify the peaks, the diffraction peaks were matched against the database available from the International Centre for Diffraction Data (ICDD).

3.4.5 Temperature Programmed Oxidation (TPO)

Temperature Programmed Oxidation (TPO) is a characterisation technique used to measure the oxidation behaviour of a sample. An oxidising gas is passed over a sample whilst being heated by a furnace, and an in-line Mass Spectrometer (MS) measures any gases that evolve from the sample. TPO was used in this work to quantify the carbon deposition on tested SOCs. The temperature at which the carbon is oxidised gives information on the strength of the interaction of the carbon with the material, and how easily it may be removed during fuel cell operation.

Four known amounts of carbon black ranging from 0.3 to 1.2 mg were used to create a calibration curve, and repeated in triplicate. A quartz tube of outside diameter 10 mm and inside diameter 6 mm was placed inside a horizontal split furnace with one end connected to a mass flow controller set to 20 ml/min air, and the other end connected to a MS. Samples were prepared for TPO by crushing the SOCs in a pestle and mortar to increase the surface area for oxidation and so as to fit inside the quartz glass tube. Quartz wool was placed on either side of the crushed sample to hold it in place within the quartz tube. The furnace was programmed to increase temperature at 5ºC/min to 900ºC and held for 1h to ensure complete oxidation of any deposited carbon. An MKS Cirrus Mass Spectrometer was used to analyse the gases evolved with particular interest in gases with mass 44 (CO_2) and mass 28 (CO).

CHAPTER FOUR

CELL MANUFACTURING

Parts of this chapter are based on the publication:

A. L. Snowdon, Z. Jiang, R. Steinberger-Wilckens,

Five-layer reverse tape casting of IT-SOFC, Int. J. of Appl. Ceram. Technol. (2021) 1-10

doi: 10.1111/ijac.13911

Author contributions can be found in Annex C.

Recent advances in solid oxide cell technology have been focusing on adapting the material set so that the same power capability is achieved at a reduced operating temperature. This will minimise thermal stresses and potentially reduce the need for expensive high-temperature materials. This chapter therefore focuses on how to adapt the method of manufacturing SOCs via reverse aqueous tape casting using the intermediate-temperature materials discussed in Chapter 2; NiO/10Sc1CeSZ (NiSSZ) fuel electrode, 10Sc1CeSZ (SSZ) electrolyte, and La0.6Sr0.4Co0.2Fe0.8 Oxide (LSCF) oxygen electrode, with a Gd0.2Ce0.8 Oxide (GDC) barrier layer. Once the method was established, the cells were tested in fuel cell mode as an initial performance check and the i-V curves and impedance spectra analysed and compared to cells purchased from

Ningbo SOFCMAN. The NiSSZ and NiYSZ cells manufactured in house were also compared to each other in order to investigate the effect of the material selection. Tape casting was chosen as the method of production because of its simplicity, affordability and the instruments accessibility, meaning every step of the process could be controlled in-house. Two methods of manufacturing were explored; the first involved tape casting five layers of the cell (the two fuel electrode layers, the electrolyte, the barrier layer and a composite layer). The second method utilised tape casting for the fuel electrode and the electrolyte, and had a spin-coated barrier layer.

In the rest of this work, the author will refer to NiSSZ being cells made from NiO/10Sc1CeSZ fuel electrode, 10Sc1CeSZ electrolyte, 10GDC barrier layer and LSCF oxygen electrode, and refer to NiYSZ as being cells made from NiO/8YSZ fuel electrode, 8YSZ electrolyte, 10GDC barrier layer and LSCF oxygen electrode.

4.1 Tape Casting Method

4.1.1 Thermal Expansion Coefficient

The cells manufactured and tested in this work were based on a previous method development by Arifin et al.[43]. It was necessary to modify this method in order to incorporate both the LSCF oxygen electrode and the required GDC barrier layer, which prevents the formation of an insulating $SrZr_2O_3$ layer between Zr in the electrolyte and Sr in the oxygen electrode. Initially, a GDC barrier layer was tape cast along with the original electrolyte and fuel electrode layers. However, due to thermal expansion coefficient (TEC) mismatch, the GDC barrier layer tended to delaminate from the electrolyte layer upon high temperature sintering, as can be seen in Figure 4.1. Changes to the GDC layer thickness, sintering time and temperature did not prevent

the delamination.



(a) Visible delamination. **(b)** SEM image of delaminated boundary.

Figure 4.1: GDC layer delaminating from the electrolyte after sintering for 4 hours at 1400 ºC.

TEC is a temperature-dependant property that describes a material's change in length, volume, density, and area with temperature, excluding phase transitions. Sintered pellets of GDC, SSZ and YSZ were used to measure the TEC during the sintering stage at 1400ºC. The results are presented in Table 4.1. The difference in TEC between the electrolyte layer (YSZ or ScCeSZ) and the barrier layer (GDC) is 3.12 x10^{-6} K^{-1} between YSZ and GDC, and 2.96 x10^{-6} K^{-1} between ScCeSZ and GDC. The large difference in these TEC values explains the delamination seen upon high temperature sintering. TEC values are similar for the two zirconia structures, YSZ and ScCeSZ, which explains why this delamination is seem for both Ni-YSZ and Ni-ScCeSZ cells.

Table 4.1: TEC values between 298 and 1073 K for YSZ, ScCeSZ and GDC.

Material	**TEC x10^{-6} K^{-1}** 298 - 1073 K
8YSZ	10.72
10ScCeSZ	10.88
10GDC	13.84

To mitigate the mismatch in TEC and delamination of GDC, the addition of a new composite layer consisting of electrode-barrier layer material was manufactured. To this effect, the reverse tape casting technique was used to manufacture fuel electrode supported cells using a novel five-layer technique; GDC barrier layer, new composite layer, electrolyte layer, fuel electrode functional layer, and fuel electrode substrate. The composite layer allowed for a gradual transition from electrolyte to barrier layer eliminating the harsh step-change present in previous manufacturing attempts and, therefore, avoiding delamination upon sintering. Figure 4.2 shows the SEM line scans of (a) before and (b) after the addition of the new composite layer, where the benefit of a graduation transition from electrolyte to GDC can be seen.

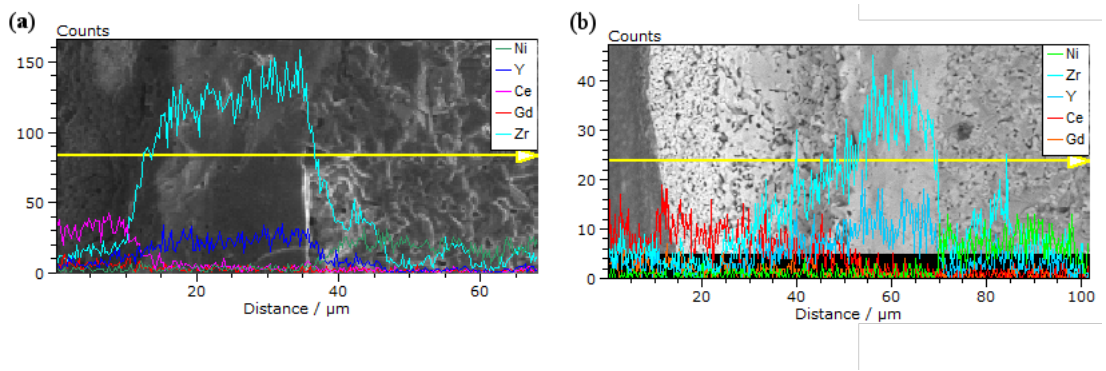


Figure 4.2: EDX element line scans of the cross section from (a) traditional NiYSZ cell and from (b) a new 5 layer cell.

4.1.2 Effect of layer thickness

Controlling the thickness of each tape cast layer needs to take into account the viscosity of the slurry, the traverse speed of the tape caster, and the applied gap height, which is the distance between the carrier film and the doctor blade. In this section the gap height was varied to investigate how the addition of another layer would effect the performance of the cells. The slurry viscosity and the traverse speed were kept constant as the gap height was varied. This was the most effective way to identify the effects of changes in layer thickness. The thickness

was optimised to produce cells which were dense enough to stop gas cross-over between the two electrodes and also small enough to result in a minimal increase in ohmic resistance (R_s) compared to cells without the composite layer. The limit of the tape casting equipment was identified in terms of manufacturing a homogeneous layer that sintered effectively.

Cells were named according to the gap height used for each layer (barrier:composite:electrolyte). For example, Cell 115 represents a cell with a gap height of 10 µm for the barrier layer, 10 µm for the composite layer and 50 µm for the electrolyte layer. The adjustable film applicator had an accuracy of ±10 µm.

4.1.2.1 Cell 101010

In order to establish the theory behind the method of a composite layer, cells were first manufactured with a large gap height (100 µm) for each layer. It was expected that these cells would not be suited for electrochemical testing due to the large ohmic resistance that would result from having a greater thickness. Figure 4.3 shows an SEM micrograph of these half cells, it is clear to see the dense electrolyte and the gradual transition to the barrier layer, with no cracks or delamination from the GDC barrier layer present after sintering.

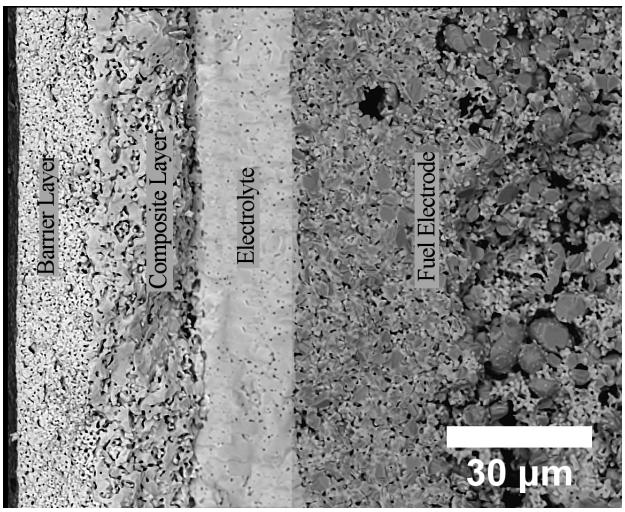


Figure 4.3: SEM micrographs of composite layer for cross-section of Cell 101010.

4.1.2.2 Cell 111

In order to test the limits of the tape casting equipment, the slurry preparation and reverse tape casting process was repeated whilst the thickness of each layer was changed to 10 µm, the smallest measurement of the film applicator. Figure 4.4 shows the SEM micrograph of the five layers after high-temperature sintering, which resulted in an overall electrolyte-composite-barrier layer thickness of 15 µm, 6.3 µm of this being the electrolyte. Even though the tape casting equipment had been able to produce cells with acceptable layer thickness, Cell 111 resulted in poor performance and a reduced OCV value due to an inconsistent electrolyte layer thickness, causing gas crossover and leakage during operation. Pinholes could be seen in the electrolyte layer, which indicated poor degassing stage in the manufacturing leading to an increased porosity.

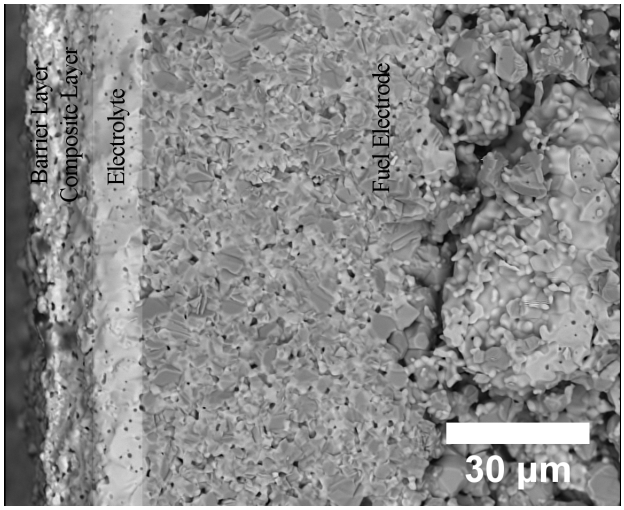


Figure 4.4: SEM micrographs of composite layer for cross-section of Cell 111.

The GDC barrier layer stops the formation of $SrZrO_3$ insulating layers forming between the Zr of the electrolyte and the Sr of the oxygen electrode. Figure 4.4 shows some level of porosity in the GDC barrier layer. However, the porosity of the GDC layer does not influence its effectiveness, it is rather the formation of a dense GDC/YDZ interface, which is depleted of Zr, that prevents the reaction between Sr and Zr. This Zr-depleted layer increases with increasing

GDC sintering temperature up to 1400ºC, improving the effectiveness of the barrier layer [193].

4.1.2.3 Cell 333

It was noted that when tape casting at the minimum gap height of 10 µm, holes in the tape appeared, most probably due to surface tension between the polyester carrier film and the slurry, explaining the gas-crossover in Cell 111. After testing each gap height of the tape caster, it was concluded that these holes were less likely to appear when using a gap height of 20 µm, and were completely absent when using a gap height of 30 µm. Therefore, Cell 333 was manufactured without the appearance of holes in the layer. Figure 4.5 shows Cell 333 with each layer having a thickness of approximately 7.0 µm after sintering. It was also noted that these holes were more likely to form when casting directly onto the carrier film and not when casting the second layer onto the first layer. This is in agreement with the surface tension theory. Consequently, casting a thicker 30 µm GDC layer first, followed by a 10 µm layer would not result in any holes.

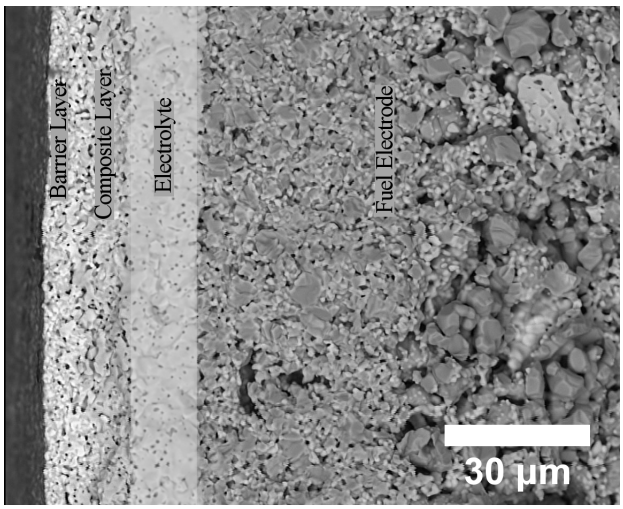


Figure 4.5: SEM micrographs of a composite layer from the cross-section of Cell 333.

4.1.2.4 Cell 214

The requirement of the composite layer was to act as a transition layer between the electrolyte and the barrier layer, therefore, it was not required to be completely dense or of a particular thickness. In fact, this composite layer was required to be as thin as possible to minimise additional ohmic resistance in the cell. To overcome previous limitations in the electrolyte, this layer was increased in thickness to prevent gas crossover. Hence, Cell 214 was manufactured with the lowest gap height for the composite layer and optimised GDC layer thickness for the tape casting equipment. Figure 4.6 reveals the dense electrolyte, thin composite and GDC layers of Cell 214 after sintering.

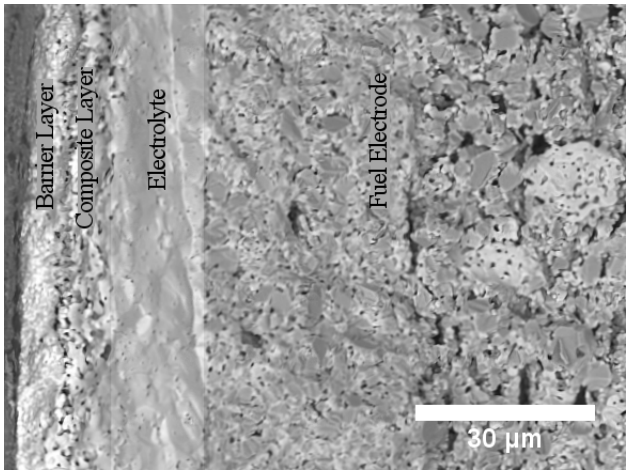


Figure 4.6: SEM micrographs of composite layer for cross-section of Cell 214.

Table 4.2 illustrates the tape casting process of each layer and its relative thickness. All cells have an anode functional layer and anode substrate layer thickness of approximately 30µm and 500µm, respectively. The OCV of each type of cell is also shown, which indicates the effectiveness of the solid electrolyte, if the cell is completely sealed within the cell holder.

The average thickness of fuel electrode supported cell electrolytes was in the range of 10 to 15µm [194]. As can be seen in Table 4.2, Cell 101010 layers are too thick, which will result

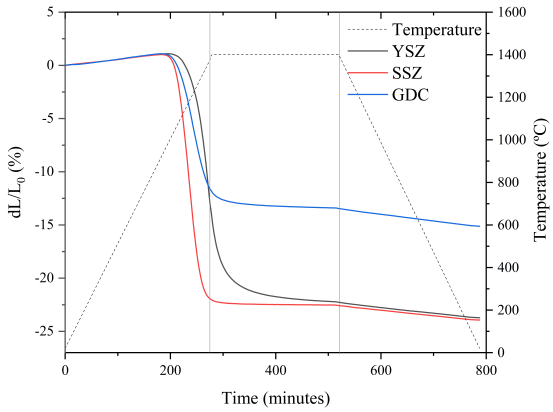
in large ohmic and polarisation resistances. This cell was not electrochemically tested as it was only manufactured to prove the method. Cell 111 proved that 4µm was the thinnest layer achieved after sintering that the tape casting equipment could produce, which was useful for the composite layer, however resulted in a drop in OCV due to gas cross-over if used for the electrolyte. Cell 333 produced an electrolyte that was thinner than the average values given in literature, however, a good OCV was obtained. The slight reduction in OCV value from the theoretical could be attributed to insufficient cell sealing within the housing. Cell 214 resulted in a dense electrolyte with no pinholes, which was reflected in the good OCV, however, the overall thickness of the three layers was still quite high, resulting in an increased ohmic resistance of the cell. As seen in Table 4.2, Cell 214 (32.3 µm) has a total thickness that is greater than Cell 333 (21.5 µm), which should not be the case if following the methodology outlined above. For Cell 333 the doctor blade gap height was not changed before each layer was cast, however for Cell 214 the doctor blade gap height was changed for each layer, increasing the uncertainty each time. This discrepancy in sintered layer thickness highlights the poor overall uncertainty of the tape casting equipment and associated doctor blade and should be taken into account when considering cell manufacturing techniques.

Table 4.2: Details of the differences in layers from the five-layer manufacturing technique and their corresponding OCV.

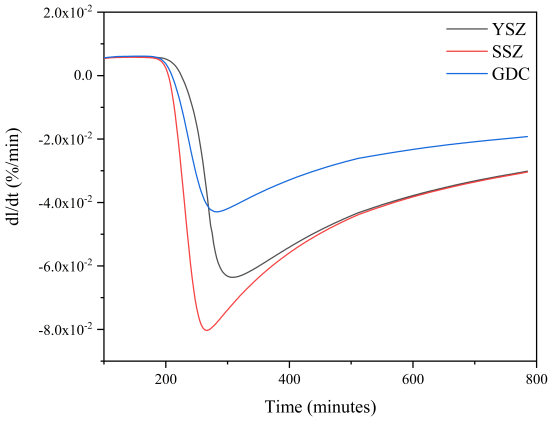
Name	**GDC**	**Composite**	**Electrolyte**	**Total**	**OCV**	R_s
	µm	**µm**	**µm**	**µm**	**(800°C)**	Ωcm^2
Cell 101010	15.1	28.2	21.3	64.6	n/a	n/a
Cell 111	4.5	4.2	6.3	15.0	0.89	n/a
Cell 333	7.0	7.0	7.5	21.5	1.01	2.7
Cell 214	8.1	6.0	18.2	32.3	1.09	0.89

4.1.3 Effect of Sintering

In order to find out the behaviour of each material during sintering, pellets of GDC, SSZ and YSZ were made and the shrinkage-expansion of the materials during sintering was investigated using dilatometry. Figure 4.7 (a) shows the graph of length change over time as the temperature increased from 20ºC to 1400ºC. As the temperature increased, all materials gradually expanded, until approximately 1000ºC, where SSZ and GDC started to sinter, indicated by a sudden change in dL/L_0 to negative. YSZ began to sinter at a higher temperature of approximately 1100ºC. YSZ and SSZ both had a much larger length change compared to GDC, 23.72 % and 23.93%, compared to 15.11%, respectively. From looking at the sintering rates in Figure 4.7 (b), SSZ had the highest sintering rate, and even though GDC began to sinter before YSZ, YSZ sintered at a much faster rate.



(a) Shrinkage-Expansion graph of YSZ, SSZ and GDC pellets during sintering profile.



(b) Sintering rates as a function of time for YSZ, SSZ and GDC pellets.

Figure 4.7: Thermal expansion information of YSZ, SSZ and GDC pellets between 20ºC and 1400ºC.

The difference in length change of the GDC compared to the zirconia materials in Figure 4.7 indicate that the GDC did not sinter as much as the SSZ and YSZ. GDC shrunk by approximately 10% less than the zirconia materials. This could suggest some residual porosity in the

GDC layer and will be discussed in Section 4.1.3.3.

Green tapes were sintered at three different temperatures, 1300ºC, 1350ºC or 1400ºC for either 3 or 4 hours. The following sections will discuss the characteristics of the microstructure in terms of particle size and porosity.

4.1.3.1 Electrolyte

One of the fundamental characteristics of an SOC is the dense electrolyte that prevents gas crossover and enables oxygen ion migration from one electrode to the other. SEM was used to identify any residual porosity or cracks, and measure the particle size of the sintered YSZ and SSZ electrolytes. As the sintering temperature increased, the particle size also increased, reducing any open porosity and also influencing the ionic conductivity.

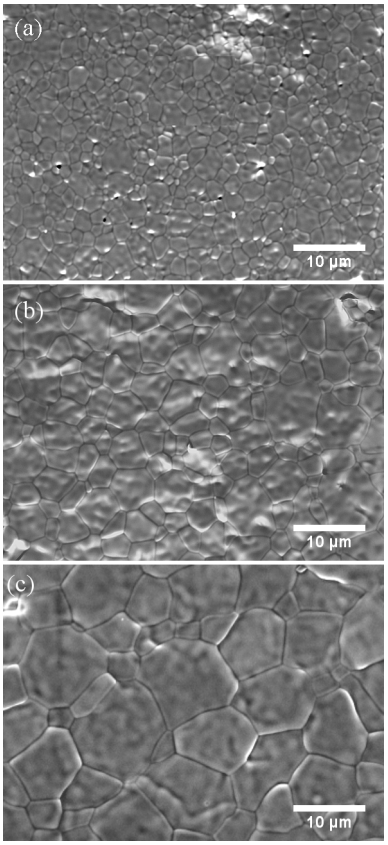


Figure 4.8: SEM micrographs of ScCeSZ pellets sintered at (a) 1300ºC, (b) 1350ºC and (c) 1400ºC for four hours.

Figure 4.8 illustrates the grain growth during sintering at different temperatures of the Sc-CeSZ electrolyte. Particle size analysis reveals average particle size for tapes sintered at 1300ºC, 1350ºC and 1400ºC to be 2.33 µm, 4.09 µm and 8.16 µm, respectively. In Figure 4.8 (a) there is still some residual porosity or pinholes that can be seen, which can be removed by increasing the temperature up to 1350ºC. Ionic conductivity of ScCeSZ increases with average grain size, hence the half-cell sintering temperature of 1400 ºC over a period of four hours was chosen as it produced a dense electrolyte layer with the largest grain size [195].

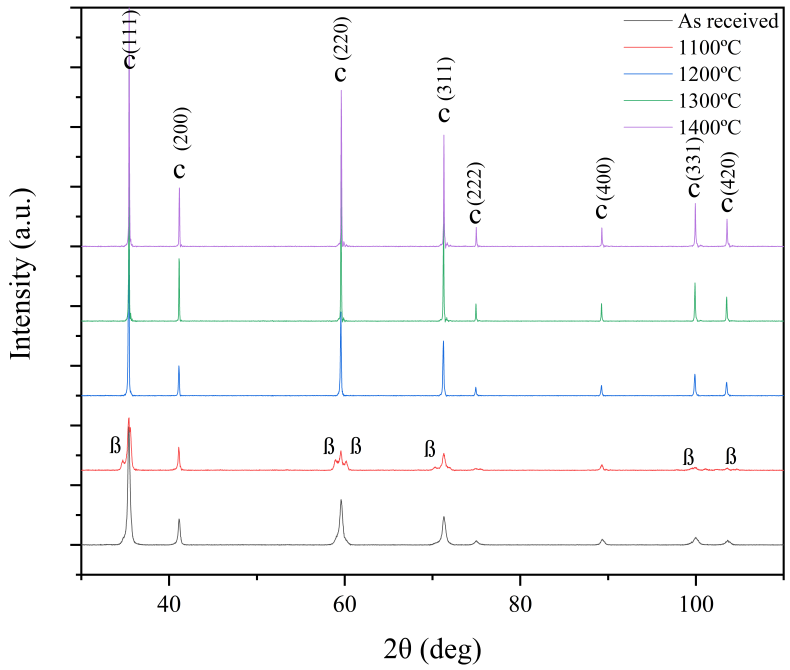


Figure 4.9: XRD spectra of ScCeSZ samples sintered between 1100ºC and 1400ºC for four hours. β indicates the rhombohedral phase and c indicates the cubic phase.

Scandia stabilised zirconia shows a conductive cubic phase structure at temperatures above 650ºC, however, at lower temperatures it can undergo a phase transition to a lower symmetry rhombohedral structure, with a reduced conductivity. To stabilise the cubic structure, 1% CeO_2 is co-doped onto the structure, and ScCeSZ becomes a promising electrolyte for IT-SOC

with superior mechanical strength, thermal compatibility, and ionic conductivity over a large temperature range.

XRD analysis was used on SSZ to confirm the phase of the electrolyte when using different sintering temperatures for the half cell. Figure 4.9 shows the XRD pattern of the as-received powder and SSZ pellets sintered at 1100ºC to 1400ºC for 4 hours. At a sintering temperature of 1100ºC, the less conductive rhombohedral-β-phase can be seen, identified by the split peaks, for example at $2\theta = 60º$. This indicates sintering is not complete as the oxygen vacancy-rich cubic phase has not yet been formed. As the sintering temperature increased to 1200ºC, the cubic phase, denoted by c, can be seen, indicating the presence of the more conductive crystal structure. As the sintering temperature increased, the also SSZ increased in crystallinity, shown by the narrowing of the peaks for samples 1200ºC, 1300ºC and 1400ºC in comparison to the broader peaks for the 1100ºC and the as-received sample. This is in agreement with the SEM micrographs in Figure 4.8.

4.1.3.2 Fuel Electrode

During sintering, the binder, pore former and other additives in the fuel electrode get burned off, inducing porosity within the structure. SOC fuel electrode porosity is typically in the range of 20 to 35% to obtain optimal performance. Values greater than this disrupt the percolation threshold of the Ni network (approximately 35%vol), increasing activation overpotential and decreasing mechanical strength. Low porosity values results in no continuous network for the gas phase to permeate through the electrode [196].

Tapioca starch was used as pore former in the production of the green tapes. By varying the amount of pore former between 1.5 and 3.0 wt%, the influence of the pore former with respect to sintering temperature can be seen. Green tapes consisting of the fuel electrode functional layer

and support were manufactured via the aqueous tape casting procedure outlined in Chapter 3, Section 3.2.1.2. The porosity of the fuel electrode was measured on 6 mm diameter pellets before and after reduction. The average porosity values for NiYSZ and NiSSZ tapes are shown in Tables 4.3 to 4.5.

Table 4.3: Ni-SSZ with 1.5% pore former fuel electrode porosity before and after reduction in H_2.

Sintering Temperature (ºC)	**Unreduced Porosity (%)**	**Reduced Porosity (%)**
1300	22.67 ± 0.034	33.21 ± 0.096
1350	15.56 ± 0.20	29.55 ± 0.088
1400	10.13 ± 0.076	23.88 ± 0.062

Table 4.4: Ni-YSZ with 1.5 % pore former fuel electrode porosity before and after reduction in H_2.

Sintering Temperature (ºC)	**Unreduced Porosity (%)**	**Reduced Porosity (%)**
1300	28.27 ± 0.10	30.16 ± 0.06
1350	23.30 ± 0.18	26.01 ± 0.13
1400	15.81 ± 0.23	21.01 ± 0.075

Table 4.5: Ni-YSZ with 3% pore former fuel electrode porosity before and after reduction in H_2.

Sintering Temperature (ºC)	**Unreduced Porosity (%)**	**Reduced Porosity (%)**
1300	37.27 ± 0.09	44.73 ± 0.19
1350	26.93 ± 0.22	36.19 ± 0.20
1400	17.99 ± 0.15	31.23 ± 0.28

The porosity decreased with sintering temperature for both NiYSZ and NiSSZ tapes. Comparing the porosity of the NiSSZ to the NiYSZ tapes, the NiYSZ tapes produced denser cells than tapes made from NiSSZ with the same amount of pore former (1.5%). This can be explained by the particle size difference between the SZZ and the YSZ powders. The SSZ particles were of a similar particle size to the NiO, whereas the YSZ was slightly larger than the

NiO. This resulted in the YSZ particles being more closely packed, resulting in a denser structure and the difference in porosity observed. The NiYSZ tapes with 3% pore former produced electrodes with high porosity (>30%) across all sintering temperatures. Sintering NiYSZ cells at 1400ºC using 1.5% pore former resulted in an acceptable 30 % porosity. The porosity values for NiSSZ tapes with 1.5% pore former show that sintering half cells at 1350ºC would result in cells with similar porosity to the NiYSZ cells sintered at 1400ºC. Sintering the NiSSZ cells at 1400ºC would also result in a optimal microstructure and porosity within the 20 to 35% range previously stated.

4.1.3.3 GDC Barrier Layer

Various methods of depositing a thin, dense layer of GDC have been successfully used in the past, such as screen-printing and physical vapour deposition (PVD), however they require additives that can reduce cell performance, incur a higher cost, or are more time consuming in manufacturing in comparison to tape casting [197]. Some researchers have also commented that the thin (usually a few 100 nm) barrier layer only has a short diffusion path, which still allows the migration of Sr and Zr species via defects and grain boundaries [198]. The method of including a sintering aid such as Fe_2O_3 to a screen printed GDC layer can lead to a dense barrier layer at higher sintering temperatures, but also yields a reduced electrochemical performance (0.385 Wcm^{-2}) in comparison to cells fabricated without any sintering aid (0.86 Wcm^{-2}) [199]. In research similar to the work carried out here, a magnetron sputtered composite layer between a YSZ electrolyte and a GDC barrier layer was successful in yielding cells with power density of 0.94 Wcm^{-2}. However, the degradation rate for these magnetron sputtered cells was very high (18%/1000 h) due to poor adhesion of the sputtered layer [200].

It has been shown that insulating layers can form when co-sintering GDC and zirconia elec-

trolytes at temperatures above 1250ºC, a process which can be suppressed by the addition of a small layer of nominal composition $Ce_{0.43}Zr_{0.43}GD_{0.10}Y0.04O_{1.93}$ [201]. On the other hand, sintering GDC at high temperatures (1400ºC) followed by sintering of LSCF at 1080ºC has been shown to reduce the formation of insulating layers more than sintering GDC at reduced temperatures. Additionally, sintering an LSCF oxygen electrode onto a GDC barrier layer affects the grain and pore size of the GDC barrier layer, due to the activity of Fe and Co, which act as sintering aids [202].

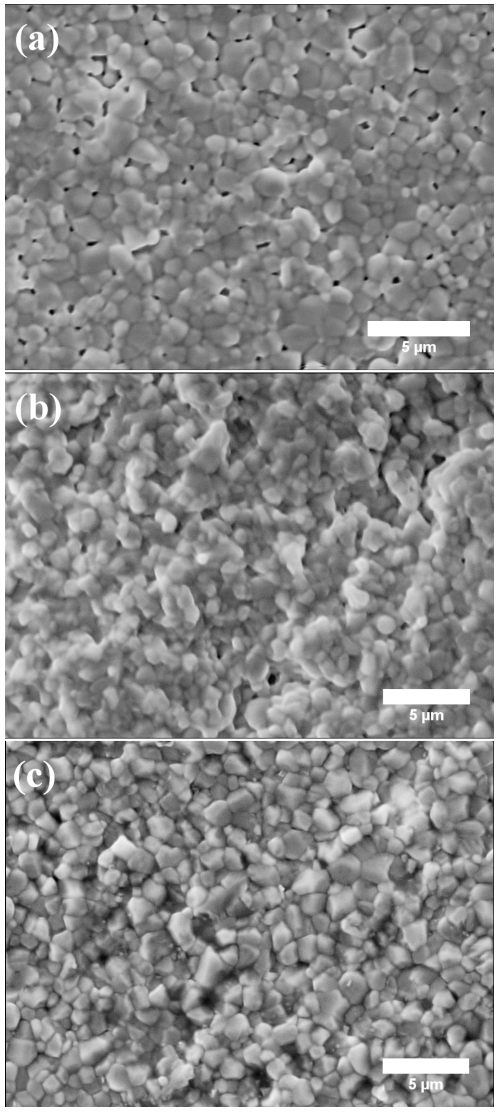


Figure 4.10: SEM micrographs of the GDC surface after sintering for 4 hours at (a) 1300ºC (b) 1350ºC and (c) 1400ºC.

Figure 4.10 shows the surface of the tape cast GDC barrier layer, highlighting the change in particle size and porosity with respect to sintering time and temperature. The images show more pores for the cells sintered at 1300ºC, and larger particle sizes with less pores for the cells sintered at 1400ºC for 4 hours. This information corroborates the shrinkage-expansion data from Figure 4.7, confirming that a sintering temperature of 1400ºC is necessary to minimise residual porosity and obtain an effective barrier for a tape cast GDC layer.

4.2 Spin Coating Method

The five-layer tape casting method succeeded in producing cells that showed no signs of delamination between the GDC barrier layer and the zirconia electrolyte, however, the addition of another layer to the cell increased the R_s, adversely affecting the performance. Reducing the thickness of the composite layer to a minimum assisted in reducing the R_s of the cell, however the limitations of the tape caster resulted in overall sub-optimal performance.

The ability of the tape casting equipment to produce a homogeneous layer was limited to approximately 4 µm. In order to overcome the challenge of reducing the ohmic resistance, a spin coating method was therefore investigated for the application of a homogeneous layer of thickness ≤ 4 µm. The spin coating method also reduced the challenge of co-sintering the electrolyte with the barrier layer, because the GDC was applied to a pre-sintered half cell (electrolyte and fuel electrode), eliminating the risk of delamination.

The process of tape casting the electrolyte and the fuel electrode (functional layer and support) was kept the same as per the previous descriptions in section 4.1. The difference being that the electrolyte was tape cast directly onto the carrier film, and the fuel electrode functional layer was tape cast on top of the electrolyte, both layers being dried in the oven at 60ºC in between casting, and the support cast on top of the functional layer. Once dry, the flexible green tape was

cut into button cells of diameter 40 mm and co-sintered at 1350ºC for four hours with organic burn-out stages at 300ºC and 600ºC. Previously, the sintering temperature was 1400ºC to account for the GDC layer, which required a higher sintering temperature than SSZ or YSZ. With the GDC layer being applied after the half cell sintering, this temperature could be reduced to minimise cell curvature whilst keeping the porosity of the fuel electrode within the acceptable range (Table 4.3).

4.2.1 Effect of RPM

Table 4.6: The different programmes used to investigate GDC thickness from spin-coating method.

Method	Rotation Speed (rpm)	Time (s)	GDC thickness (µm)
1	1200	20	5.61 ± 0.34
2	1700	20	4.65 ± 0.41
3	2500	20	2.80 ± 0.39

Three rotational speeds of the spin-coater were evaluated; 1200 rpm, 1700 rpm and 2500 rpm, each held for 20 seconds. Figure 4.11 shows the SEM images of half cells with GDC applied via spin coating at different speeds. The GDC thicknesses were measured using ImageJ software and were found to be 5.61 µm, 4.65 µm, and 2.80 µm for the cells spin coated at 1200 rpm, 1700 rpm, and 2500 rpm, respectively. In order to obtain a GDC barrier layer with thickness < 4 µm, the spin coater method 3 with 2500 rpm was chosen. The GDC layer in Figure 4.11 is identified as the white layer on the right, next to the dense electrolyte. The three different methods are described in Table 4.6.

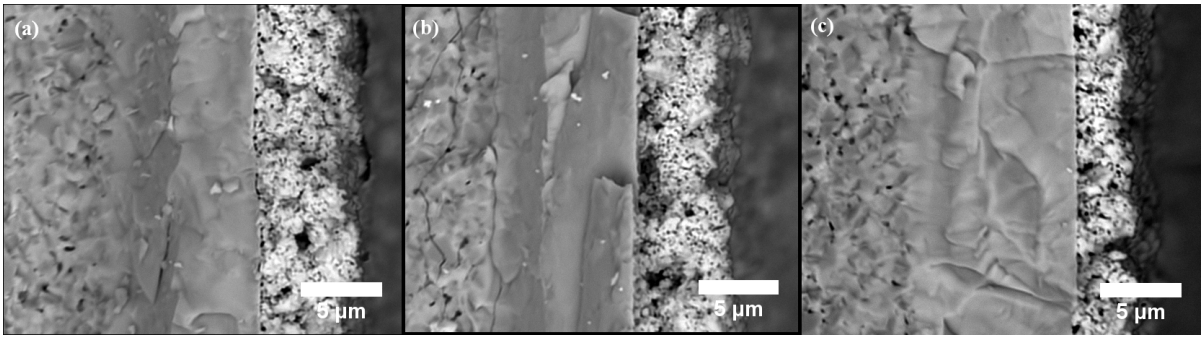


Figure 4.11: SEM micrographs of the cross section of a half cell after applying spin coated GDC at (a) 1200 rpm, (b) 1700 rpm, and (c) 2500 rpm.

4.3 Comparison of composite and spin coated cells

To investigate their potential as SOCs, NiSSZ cells fabricated by tape casting and spin coating were made into full cells and tested in fuel cell mode alongside NiYSZ cells made in the same way, further validating the results against literature values. A two-layer oxygen electrode; LSCF-GDC and LSCF, was painted onto the GDC barrier layer and sintered at 1080ºC for 3 hours. The cells were secured inside the cell holder in the testing rig, and heated at 3ºC/min to 800ºC where they were reduced overnight in 85% H_2 (balance N_2). Both types of cell underwent initial characterisation at 800ºC, exposing the fuel electrode to 60 mL/min H_2 and 10 ml/min N_2, and exposing the oxygen electrode to 200 mL/min air.

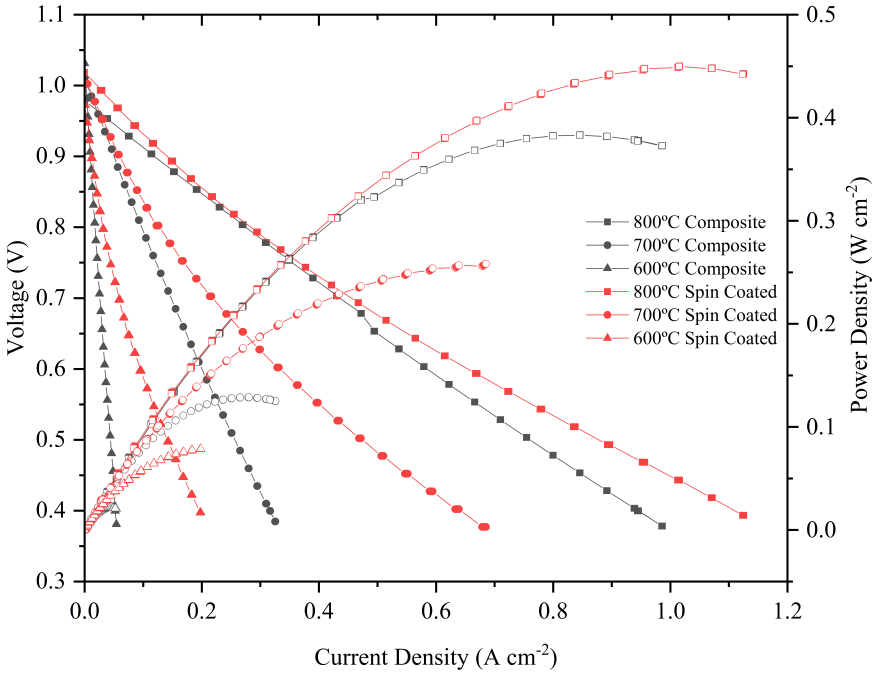


Figure 4.12: Polarisation curves of Ni-SSZ cells made via the composite tape casting method (grey) and the spin coated method (red) from 600ºC to 800ºC.

Figure 4.12 shows a comparison between the i-V curves for the composite cells and the spin coated cells, taken from OCV to 0.4 V at 600ºC, 700ºC and 800ºC. The NiSSZ cells made by the composite five layer tape casting method are shown in grey and the NiSSZ cells made by the spin coating method are shown in red. The maximum power density achieved for each cell type was 0.38 W/cm^2 and 0.45 W/cm^2 at 800ºC for composite and spin coated cells, respectively. At 800ºC, operating at a typical voltage of 0.7 V, both types of cells exhibited a similar current density, 0.43 A/cm^2 (composite) and 0.46 A/cm^2 (spin coated). However, as the cells were further polarised, the spin coated cell out-performed the composite cell. The OCV of the spin coated cells was higher than the OCV of the composite cells. The co-sintering of the electrolyte and barrier layer for the composite layer affected the sintering properties of the electrolyte, resulting in residual porosity which facilitated gas crossover, as seen by the OCV value of less

than 1 V. As the operating temperature decreased, the maximum power output decreased in line with the maximum current density. This can be explained by the lower ionic conductivity of the solid oxide electrolyte at reduced temperatures, which increases the ohmic and charge transfer resistances.

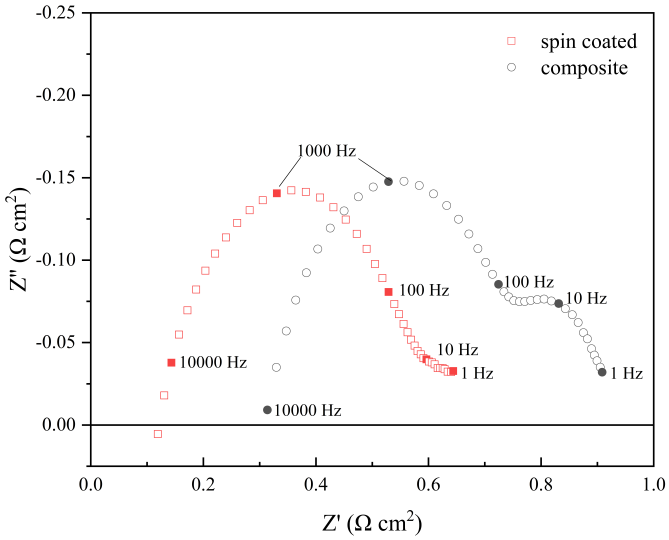


Figure 4.13: Impedance plots of NiSSZ cells made via the composite tape casting method (grey) and the spin coated method (red) at 800ºC.

Figure 4.13 shows the Nyquist plot at 800ºC for the two types of cells; spin coated (red), and composite (grey). The R_s for the spin coated cell (0.12 Ω cm^2) is lower than that of the composite cell (0.31 Ω cm^2). The R_s is related to the resistance of the electrolyte, so the addition of the composite layer, which extends the thickness of the electrolyte, has the effect of increasing the R_s. The polarisation resistance (R_{pol}) was 0.52 Ω cm^2 and 0.60 Ω cm^2 for the spin coated and composite cells, respectively. In line with this, the ASR was lower for the spin coated cells (0.64 Ω cm^2) than it was for the composite cells (0.91 Ω cm^2). The spin coated cells displayed one semi circle encompassing charge transfer resistance and diffusion resistance, indicating a small gas diffusion resistance in relation to the charge transfer resistance. On the other hand, the composite cell had a much larger gas diffusion resistance, as seen by the second

semi circle at low frequency. This large gas diffusion resistance arises in the composite cells due to the difference in microstructure; as seen in the SEM images (Figure 4.6) the porous composite layer resulted in a layer of stagnant fuel in the porous electrode, which increased the gas diffusion resistance.

The performances of both types of cells (0.38 and 0.45 W/cm^2 for composite and spin-coated cells at 800ºC, respectively) compare as well to NiSSZ cells previously manufactured using the same tape casting method in the same laboratory, which gave a power density of 0.39 W/cm^2 at 750 ºC and NiYSZ cells with a power density of 0.53 W/cm^2 at 800 ºC [43]. The similar performance of the cells made in this work prove that the new five-layer tape casting technique can be suitable for manufacturing IT-SOFCs, avoiding delamination of the GDC barrier layer during sintering. Further optimisation of the composite layer to mitigate the formation of insulating layers during sintering could be performed to further improve cell output. Overall, the spin coated cells gave higher power density and had a lower ASR, and thus were used in the experiments in the rest of this study.

4.4 Electrochemical characterisation of NiSSZ cells in fuel cell mode and electrolyser mode

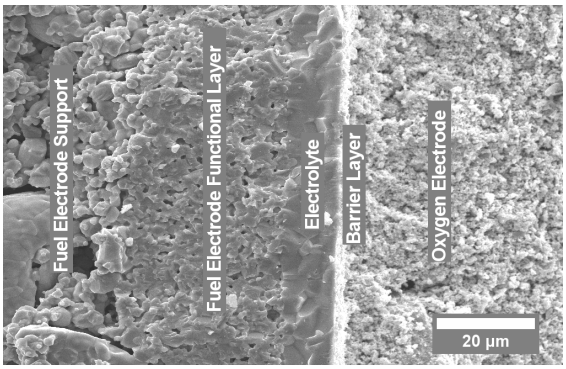
The NiSSZ cells manufactured in-house by the spin-coat method were tested in fuel cell mode and electrolyser mode using hydrogen and water, and mixtures of carbon dioxide and water. The effect of operating temperature and fuel composition on cell performance was investigated in terms of i-V curves and Electrochemical Impedance Spectroscopy (EIS). To the authors knowledge, this is the first time SOCs made from the ScCeSZ material set have been used for co-electrolysis of CO_2 and H_2O.

First, the cells were tested in SOFC mode using the same H_2 and N_2 fuel mix as used

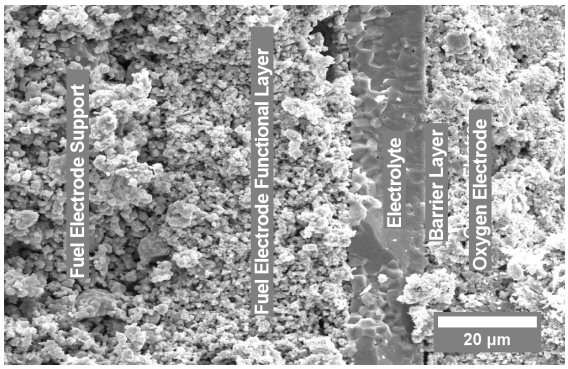
in Section 4.3 (85% H_2 and 15% N_2 at 70 ml/min, and 200 ml/min air). Then, the cells were tested in SOE mode with a H_2O and H_2 fuel mix and finally, a H_2O/CO_2 fuel mix for co-electrolysis. Commercial cells (Ni-YSZ/YSZ/GDC/LSCF) purchased from Ningbo SOFC-MAN Energy Technology were used to establish a baseline of performance to test and compare against.

4.4.1 Beginning of Life (BoL) Cells

An initial electrochemical performance check and SEM images were taken before changing the test parameters for each cell. This created a record of the cell performance and microstructure at their respective beginning-of-life (BoL) so a comparison to the end-of-life (EoL) could be made and any changes could be identified, characterised, and linked to any performacne degradation observed. The initial performance check was carried out at 800ºC after reduction of the fuel electrode from NiO to Ni. This included recording i-V curves between OCV and 0.4 V, and impedance spectra at OCV in a fuel mix of 85% H_2 and 15% N_2 on the fuel electrode at a total flow rate of 70 ml/min, and 200 ml/min air to the oxygen electrode.



(a) Un-reduced NiSSZ cell.



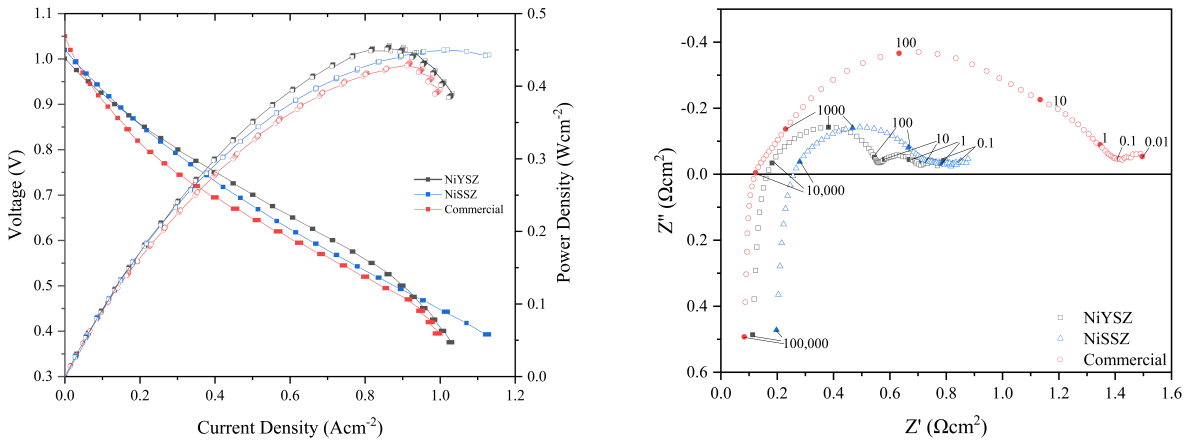
(b) Reduced NiSSZ cell.

Figure 4.14: NiSSZ full cell (a) before reduction and (b) after reduction, at BoL before electrochemical testing.

Figure 4.14 (a) shows an SEM micrograph of a full NiSSZ cell before reduction and electro-

chemical testing. The fuel electrode support can be identified by it's higher porosity in comparison to the fuel electrode functional layer, which did not contain pore former so appears more dense. The uniform, dense electrolyte can be seen free of cracks next to the thin GDC barrier layer. The uniform layers of the double-layer oxygen electrode show a good porosity and no delamination. Figure 4.14 (b) shows the same cell after reduction of the fuel electrode in H_2. The resulting reduced electrode can be identified by the increased porosity of the fuel electrode support and the fuel electrode functional layer, from the reduction of NiO to Ni.

4.4.2 Fuel Cell Testing



(a) i-V curves for different cells at 800ºC.

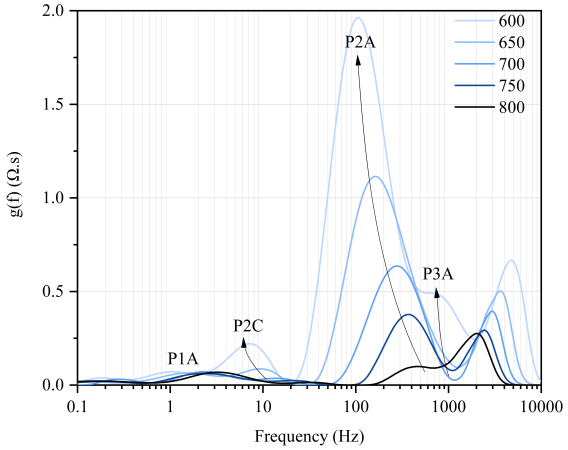
(b) EIS spectra taken at OCV at 800ºC.

Figure 4.15: (a) i-V curve and (b) EIS spectra for cells made in-house (NiYSZ and NiSSZ) compared to commercial NiYSZ cells. Frequency has been labelled on the impedance plot.

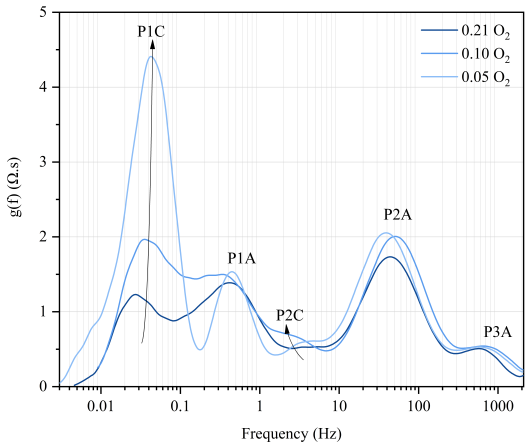
Figure 4.15 shows i-V curves for cells made in-house (NiYSZ and NiSSZ) versus commercial NiYSZ cells tested at 800ºC. At this temperature, there is no distinct advantage of NiSSZ cells over NiYSZ in terms of performance. However, a benefit can be noticed at high current densities, where a limiting current density is reached for the NiYSZ cells but not the NiSSZ cells. The ASR was highest for the commercial cells, at 1.5 Ωcm^2. The in-house cells had similar ASR with values of 0.80 Ωcm^2 and 0.87 Ωcm^2 for NiYSZ and NiSSZ cells, respectively. The ASR

was higher for the NiSSZ cells than the NiYSZ cells but the R_{pol} was the same ($0.68\Omega cm^2$) for both cells made in-house.

DRT analysis was undertaken on the impedance spectra of cells tested in fuel cell mode at different conditions to assign each peak to an internal process. Conditions that were changed were the operating temperature, and partial pressures of the fuel and the oxidant. Figure 4.16 (a) shows the DRT response with respect to temperature for a NiSSZ cell fuelled by 85% H_2, balance N_2 at 60 ml/min, and 180 ml/min air. As the temperature decreased from 800ºC to 600ºC, the high frequency peak increased until it revealed a second, coupled peak, at 600ºC. The three increasing peaks were temperature dependant and can be attributed to fuel electrode processes (P_{3A} + P_{2A}) at high frequency and the oxygen electrode process (P_{2C}) at lower frequency [203]. The low frequency peak that was independent of temperature change can be associated with the fuel electrode support (P_{1A}).



(a) DRT analysis of a NiSSZ cell operating from 600ºC to 800ºC fuelled by 100% H_2 to the fuel electrode and 0.21 O_2 to the air electrode (N_2 balance).



(b) DRT of cell with changing oxygen partial pressure to the oxygen electrode (N_2 balance.

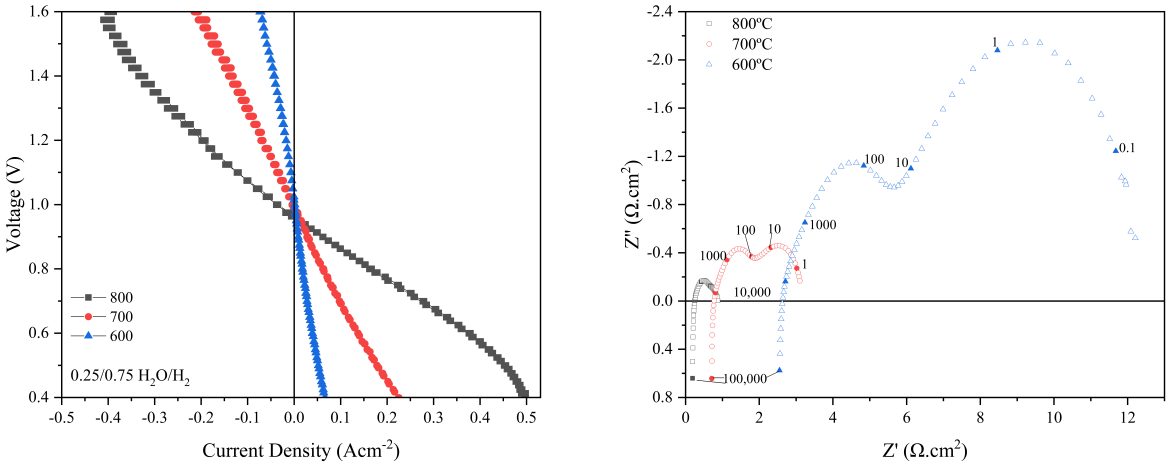
Figure 4.16: DRT analysis showing changing internal processes when operating at different temperatures and different O_2 partical pressure.

The DRT of impedance spectra measured at OCV with varying amounts of O_2 partial pressure (Figure 4.16 (b)) revealed that the high frequency peaks were independent of oxidant com-

position. Peak P_{1C} at low frequency significantly increased by reducing the oxygen partial pressure and can be assigned to gas diffusion in the oxygen electrode [204]. The five peaks identified in the DRT correspond to five internal cell processes that can be modelled in a equivalent circuit model (ECM). This is in agreement with the findings of other researchers using similar fuel electrode-supported cells [205, 206].

4.4.3 Reversible Solid Oxide Cell Testing

4.4.3.1 Effect of fuel composition



(a) Polarisation curve for NiSSZ cell.

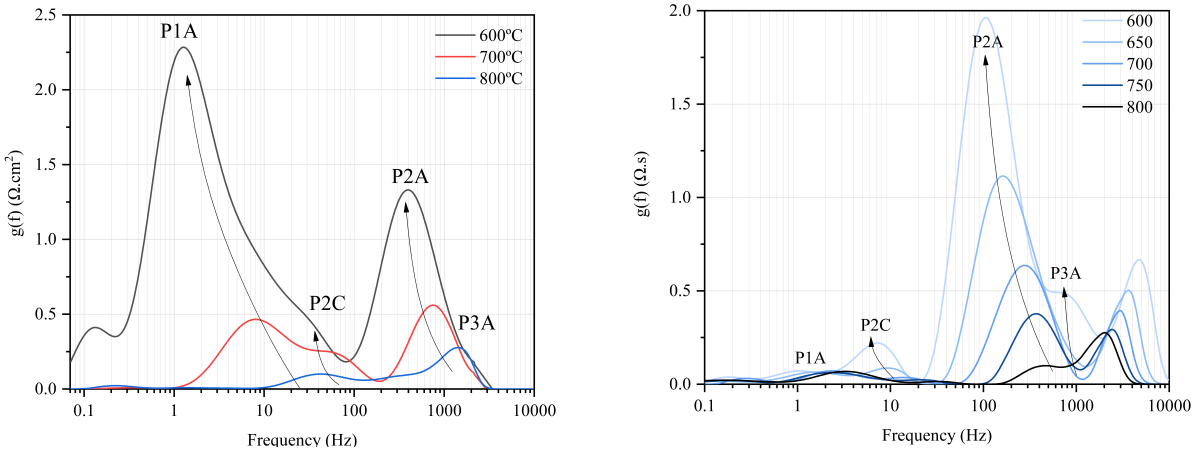
(b) Corresponding EIS taken at OCV.

Figure 4.17: Performance (i-V and EIS) of NiSSZ cells operating as rSOCs in a 0.25/0.75 H_2O/H_2 fuel mix with air on the oxygen electrode from 800ºC to 600ºC.

Figure 4.17 (a) and (b) shows the polarisation curve and the impedance for a NiSSZ cell operating on 25% H_2O in H_2, respectively. The continuity in the i-V curve between fuel cell mode and electrolysis mode as seen in Figure (a) illustrates the cell's ability to perform well as rSOCs. Electrolysis mode showed a higher ASR (1.06 Ωcm^{-2} at 1.3 V) than fuel cell mode (0.91 Ωcm^{-2} at 0.7 V) at 800ºC. Due to equipment limitations, a maximum water content of 25% was achievable, which can explain the comparatively lower performance in water electrolysis

mode than fuel cell mode.

DRT shown in Figure 4.18 highlight that during electrolysis the processes related to the fuel electrode functional layer (P_{2A}) and the fuel electrode support (P_{1A}), were the dominating processes, especially with decreasing temperature. Figure 4.18 (b) is the same as Figure 4.16 (a) and has been shown here again for reference purposes. In electrolysis mode, process P_{2A} completely obfuscates process (P_{3A}) across all temperatures. The P_{2C} process (oxygen electrode process) was also slightly dependent on water content in the fuel electrode for electrolysis.



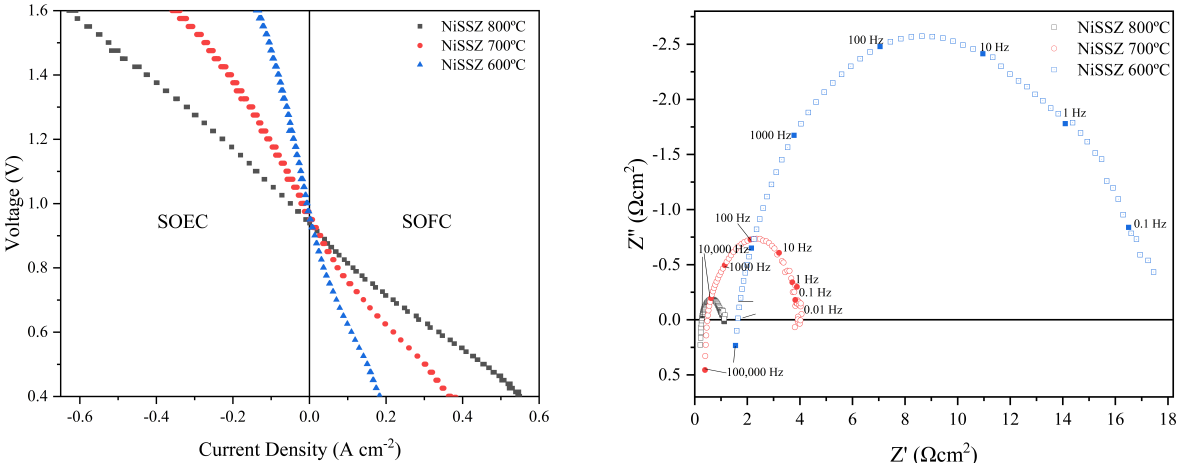
(a) Water electrolysis DRT.

(b) Fuel Cell DRT.

Figure 4.18: (a) DRT taken at OCV during electrolysis of 25% H_2O in H_2, and (b) a repeat of Figure 4.16 (a), with the DRT taken at OCV for the same type of cell in fuel cell mode.

Figure 4.19 (a) shows the polarisation curves of oxidation and reduction of a H_2, H_2O, CO_2 and CO mixture at temperatures in the range of 800ºC to 600ºC for NiSSZ cells. From these curves it was observed that no limiting current density was reached for NiSSZ cells operating on this fuel mix. The ASR was higher for co-electrolysis mode than in fuel cell mode across all temperatures. The impedance measurements at OCV (Figure 4.19 (b)) show that these cells have a larger resistance in co-electrolysis compared to water electrolysis (Figure 4.17), despite the fuel gases being supplied at a higher reactant/product ratio. The R_s contributes approximately 25% of the total resistance at 800ºC, down to 10% at 600ºC. It was not possible to

distinguish different electrode contributions to the total resistance from DRT analysis due to large contributions from the fuel electrode processes.



(a) Polarisation curve for NiSSZ cells.

(b) Corresponding EIS taken at OCV.

Figure 4.19: Co-electrolysis polarisation curves taken between 0.4 V and 1.6 V at 600ºC, 700ºC and 800ºC for NiSSZ cells with a fuel mix of 25% H_2O, 25% CO_2, 25% H_2 and 25% CO.

Figure 4.20 shows a comparison between NiSSZ cells and NiYSZ cells operating on the co-electrolysis fuel mixture. Performance was higher for co-electrolysis in the NiSSZ cells across the whole temperature range, however during fuel cell operation, the NiSSZ cell performance was only significantly higher at 600ºC and 700ºC, whereas at 800ºC the performance was equivalent to the NiYSZ cells up to approximately 0.6 V.

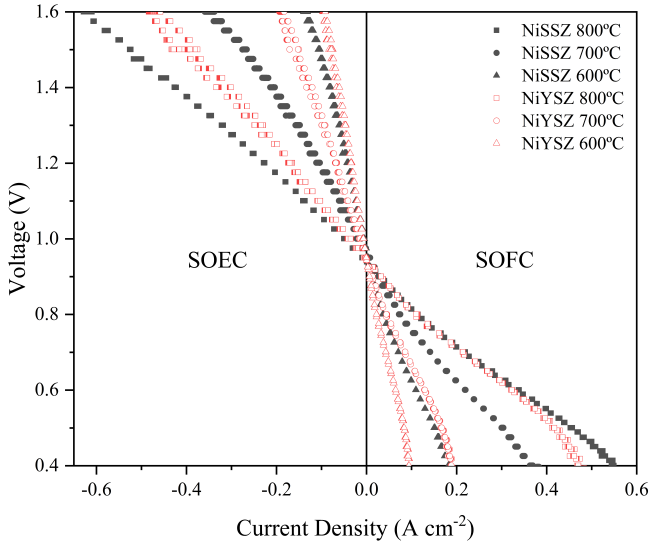
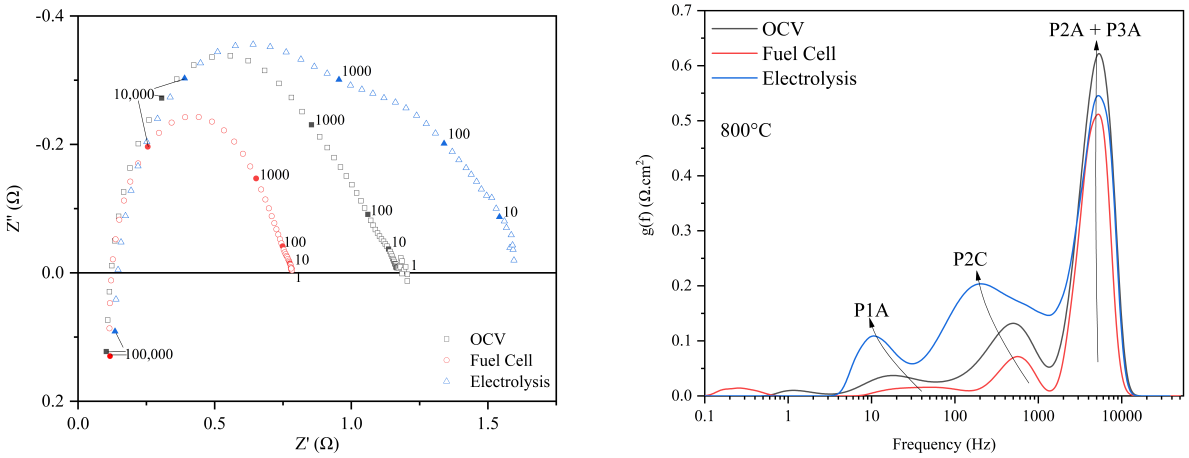


Figure 4.20: Comparison of i-V curves for NiSSZ and NiYSZ cells fuelled by 25% H_2O, 25% CO_2, 25% H_2 and 25% CO.

It can be seen that for the NiYSZ cells a limiting current density was approached at voltages below 0.5 V as the polarisation increased at high current densities. This is particularly visible for the NiYSZ cell at 800ºC. This type of resistance can be explained as a gas diffusion limitation, typically caused by the fuel supply or by a volume of stagnant gas adjacent to the porous electrode [207]. At these high current densities, the risk of carbon deposition increases, causing microstructural changes to the porous electrode, and altering the gas diffusion. This could also explain the slight hysteresis seen at high current densities during co-electrolysis at 800ºC in the NiYSZ cells. Hysteresis in the polarisation curve is linked to reaction starvation, or local changes in temperature, however these effects were not expected to occur under these conditions, therefore leaving carbon deposition as an explanation.

4.4.3.2 Effect of operating potential



(a) Impedance taken at OCV, 0.7V (fuel cell mode) and 1.3V (electrolysis mode).

(b) Corresponding DRT.

Figure 4.21: Impedance and corresponding DRT taken at 800ºC at three different potentials: 0V (OCV), 0.7V (fuel cell mode), and 1.3V (co-electrolysis) for cells fuelled by 25% H_2O, 25% CO_2, 25% H_2 and 25% CO.

The effect of operating potential on internal resistances was examined and is shown in Figure 4.21. Impedance was taken at OCV, 0.7V and 1.3V to compare the changes in impedance during fuel cell mode and electrolysis mode. The highest ASR was recorded during co-electrolysis mode (1.59 Ωcm^2), and lowest during fuel cell mode (0.78 Ωcm^2). Figure 4.21 (b) shows the DRT for the three different operating potentials. By changing the operating potential from fuel cell mode to co-electrolysis, the internal resistances associated with the fuel electrode and the oxygen electrode increased by 38% each.

Table 4.7 shows a comparative summary of resistances (Ohmic, polarisation and ASR) taken from impedance data at OCV for commercial NiYSZ cells, manufactured in-house NiYSZ cells and manufactured in-house NiSSZ cells. Factors such as contact resistance between the current collector and the cell, inductance of the wires and how well the cell is sealed in the cell holder can influence the R_s. Measures were put in place to minimise these variations, such as using the

Table 4.7: Comparison of internal resistances and ASR values obtained from AC impedance at OCV for cells operated on a co-electrolysis fuel mix.

Cell Type	Temperature (ºC)	R_s (Ω cm^{-2})	R_p (Ω cm^{-2})	ASR (Ω cm^{-2})
Commercial Cells	600	1.7	15.6	17.3
	700	0.4	4.7	5.1
	800	0.21	1.59	1.8
NiYSZ Cells	600	1.75	15.75	17.5
	700	0.55	4.02	4.57
	800	0.27	0.93	1.2
NiSSZ Cells	600	1.6	16.0	17.6
	700	0.5	3.4	3.9
	800	0.28	0.79	1.07

same amount of conductive silver paste, cutting the same size gasket, using the same conditions for reducing, and using the same spring mechanism to hold the cell holder in place.

4.5 Summary

SOCs were successfully produced in-house via aqueous tape casting technique. The GDC barrier layer for LSCF oxygen electrode cells was produced via two manufacturing techniques; tape casting and spin coating. The tape casting technique included the addition of a new composite layer, resulting in a five-layer tape casting method which produced homogeneous layers that did not delaminate from the electrolyte upon sintering. Cells produced via spin coating the GDC onto pre-sintered half cells resulted in a barrier layer thickness < 3 µm, which was thinner than the tape casting technique could achieve. The risk of delamination was minimised using this technique by sintering the GDC separately and at a reduced temperature.

The TEC and the shrinkage/expansion of GDC, SSZ and YSZ was determined by dilatometry analysis. The TEC for each material was found to be 13.84 x10^{-6}1/K for GDC, 10.88 x10^{-6}1/K for SSZ, and 10.72 x10^{-6}1/K for YSZ. The large difference in TEC between the two

zirconia based structures and the GDC material wass the reason the GDC barrier layer delaminated from the zirconia upon co-sintering. The composite layer was introduced to minimise the effect of delamination by gradually changing the TEC from GDC values to zirconia. First, the functionality of the composite layer was established, with thick ($\sim$ 20 μm each) layers. After this, the thickness of each layer was reduced down to 4 μm to establish the limit of the tape casting instrument. This however resulted in poor OCV due to a slightly porous electrolyte layer and gas cross-over during cell operation. Finally, the layer thicknesses were optimised to produce a cell with a dense electrolyte and overall thickness of 21.5 μm for all three layers (electrolyte, composite and barrier layer).

The fuel electrode microstructure was investigated by the addition of varying amounts of tapioca starch acting as a pore former to the slurry matrix. These slurries were manufactured into green tapes and sintered at 1300ºC, 1350ºC and 1400ºC to see the dual effect of the amount of pore former and the sintering temperature. A higher sintering temperature resulted in a denser microstructure, therefore 1.5% pore former was found to be optimal for the NiSSZ cells sintered at 1350ºC which gave an average porosity of 29.88%. The NiYSZ cells required 3% pore former at 1400ºC to achieve a porosity of 34.71%. Different amounts of pore former were required to get similar values of porosity in the green tapes for the NiSSZ and NiYSZ cells due to the difference in particle size of the 8YSZ and the 10Sc1CeSZ. The 8YSZ powder employed had a smaller particle size than 10Sc1CeSZ, this formed a denser microstructure with the Ni particles, therefore requiring more pore former to obtain a comparable fuel electrode microstructure.

Cells made via both manufacturing techniques were electrochemically tested to compare the performance. The addition of the new composite layer ultimately increased this type of cell's ASR, resulting in poorer performance than spin coated GDC cells. The spin coated cells

gave better overall performance, achieving a maximum power density at 800ºC of 0.45 W/cm^2, compared to the composite cells' 0.38 W/cm^2. At 800ºC, the ASR for the composite and spin coated cells was 0.91 Ω cm^2 and 0.64 Ω cm^2, respectively. Due to the higher performance of the spin coated GDC cells across the whole temperature range, this manufacturing technique was used going forward in the rest of this work.

Spin coated cells were characterised as fuel cells with H_2/N_2 gas mixtures, and as rSOCs with H_2O/H_2 gas mixtures, and $CO_2/H_2O/CO/H_2$ gas mixtures. The spin coated cells made in-house produced a higher power density (0.45 Wcm^{-2}) than commercial cells (0.43 Wcm^{-2}) when tested in fuel cell mode. The NiSSZ cells had lower R_{pol} and ASR values across the whole temperature range compared to NiYSZ cells during co-electrolysis. DRT analysis of impedance spectra revealed higher resistances in electrolysis mode compared to fuel cell mode for both the fuel electrode and oxygen electrode. NiSSZ cells achieved higher current densities than NiYSZ cells across all temperatures during co-electrolysis, and showed a significant improvement to the conventional NiYSZ material set when operating at temperatures of 700ºC and below. During co-electrolysis testing, cells made in-house (both NiSSZ and NiYSZ) had lower ASR than commercial NiYSZ cells at operating temperatures of 800ºC and 700ºC.

CHAPTER FIVE

THERMODYNAMIC EQUILIBRIUM ANALYSIS

Thermodynamic equilibrium calculations offer insight into the properties of reactions in terms of temperature, pressure, and reactant quantities. These calculations do not account for kinetics but are still suited to interpreting processes with high reaction rates, like those which occur at very high temperatures, such as in SOCs. Equilibrium calculations are often used to evaluate methane reformate compositions and carbon deposition, however, they only provide an insight to expected conditions and do not account for catalysed reactions, such as the formation of carbon over nickel [208–210]. Data here is presented in mole fractions of species, which can then be graphically represented in terms of temperature, steam/carbon (S/C) ratio, fuel utilisation, or in carbon-hydrogen-oxygen (C-H-O) ternary diagrams.

5.1 Thermodynamics of high temperature co-electrolysis

The co-electrolysis reaction proceeds via the simultaneous reduction of CO_2 and H_2O to form CO and H_2, respectively. Both reactions are endothermic, meaning they have a positive ΔH. The minimum electrical energy required for the reaction is equal to the change in Gibbs free energy (ΔG), and varies with temperature according to Equation 5.1. The ΔH and ΔS values for the

reaction can be calculated using Equations 5.2 and 5.3, where ΔH_f is the enthalpy of formation and C_p is the average specific heat capacity at 1073 K, the typical operating temperature of an SOC.

$$\Delta G = \Delta H - T\Delta S \tag{5.1}$$

$$\Delta H(T) = \Delta H_{f298K} + \int_{298K}^{T} \Delta C_p \, dT \tag{5.2}$$

$$\Delta S(T) = \Delta S_{298K} + \int_{298K}^{T} \Delta C_p \, dT \tag{5.3}$$

Table 5.1: Thermodynamic parameters for species present in co-electrolysis. ΔH and ΔS values are at standard conditions and C_p values are at 1073 K.

Species	**Enthalpy of formation** $\Delta H_f(kJmol^{-1})$	**Entropy** $\Delta S(Jmol^{-1}K^{-1})$	**Heat Capacity** $C_p(Jmol^{-1}K^{-1})$
H_2 (g)	0	130.59	30.82
O_2 (g)	0	205.03	34.59
H_2O (g)	-241.83	188.84	41.51
CO (g)	-110.5	197.9	32.85
CO_2(g)	-393.5	213.79	54.58

By plotting the thermodynamic parameters of enthalpy (ΔH), entropy (ΔS) and Gibbs free energy (ΔG), as a function of temperature, the energy requirements for the co-electrolysis reaction is broken down into electrical energy requirement (ΔG) and thermal energy requirement ($T\Delta S$), as shown in Figure 5.1. This illustrates the benefits of high-temperature co-electrolysis over low temperature operation, as the electrical energy requirement for the reaction decreases with increasing temperature and a large part of the energy can be supplied in the form of high temperature heat.

The co-electrolysis reaction is more complex than either H_2O or CO_2 electrolysis due to

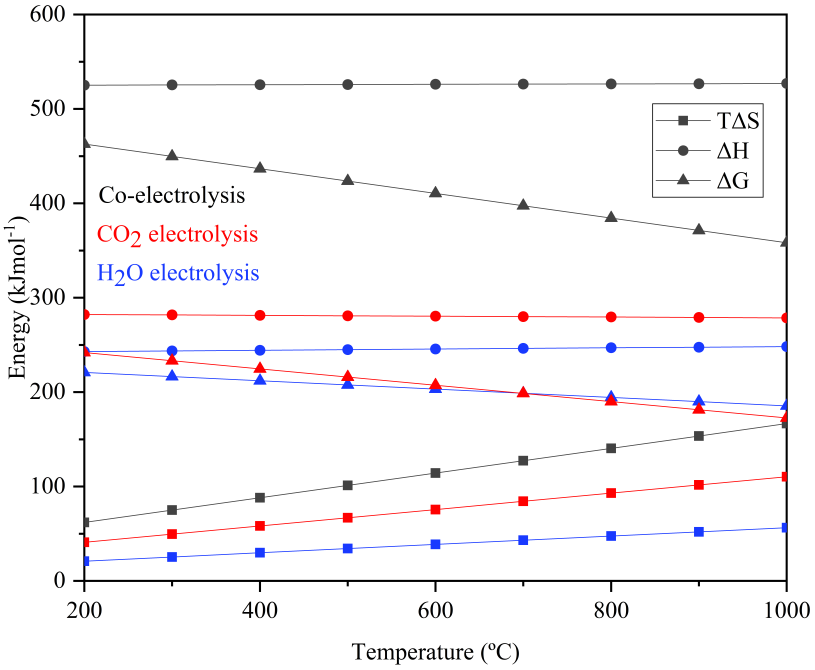


Figure 5.1: Relationships between enthalpy change (ΔH), entropy change (ΔS) and Gibbs free energy change (ΔG) of H_2O, CO_2 and co-electrolysis reactions.

the interference of the water gas shift (WGS) reaction. Simple reduction reactions occur in both H_2O electrolysis and CO_2 electrolysis, but when the two (C and H) species are mixed many side reactions can occur. The WGS boosts the H_2 yield via the reaction between CO and H_2O. There is still much debate in the literature about the overall contributions of the WGS to the co-electrolysis reaction, with some researchers saying that the WGS is responsible for CO production, whilst others believe CO and H_2 to be produced solely from CO_2 and H_2O electrolysis, respectively [29]. In addition to the WGS reaction there are a number of other possible side reactions taking place during co-electrolysis. These have been outlined in Table 5.2.

For a reaction to occur spontaneously, the ΔG for the reaction must be negative. Many of the reactions that can take place within a co-electrolysis reactor have negative values of ΔS and

ΔH, which means they are spontaneous at lower temperatures, and become less spontaneous as the temperature increases. Co-electrolysis, CO_2 and H_2O electrolysis all have large, positive values of ΔH, while also having positive ΔS which leads to a reduction in ΔG as the temperature increases, but generally not enough for them to occur spontaneously. Temperatures would have to reach over 3000°C before any of these reactions occurred spontaneously (thermolysis).

Table 5.2: Reactions potentially taking place during co-electrolysis

Reaction		
Co-electrolysis	$CO_2 + H_2O \longrightarrow CO + H_2 + O_2$	(5.4)
CO_2 Electrolysis	$CO_2 \longrightarrow CO + 0.5\,O_2$	(5.5)
H_2O Electrolysis	$H_2O \longrightarrow H_2 + 0.5\,O_2$	(5.6)
Water Gas Shift (WGS)	$CO + H_2O \longrightarrow H_2 + CO_2$	(5.7)
Reverse Water Gas Shift (RWGS)	$H_2 + CO_2 \longrightarrow H_2O + CO$	(5.8)
Boudouard	$2\,CO \longrightarrow CO_2 + C$	(5.9)
Reverse Coal Gas (RCG)	$H_2 + CO \longrightarrow C + H_2O$	(5.10)
Methanation	$CO + 3\,H_2 \longrightarrow CH_4 + H_2O$	(5.11)
Methane Cracking	$CH_4 \longrightarrow C + 2\,H_2$	(5.12)

Figure 5.2 illustrates the change in Gibbs free energies of the reactions that could be present during the co-electrolysis reaction. There are two converging points at 100°C and 700°C. At 100°C water becomes gaseous and there is a change in the energy requirement for co-electrolysis, H_2O electrolysis, RWGS and WGS reactions. At temperatures below 700°C the WGS, Boudouard and RCG reactions are thermodynamically favoured and become less so at temperatures above 700°C. Any carbon formation in the cell at temperatures below 700°C would be due to the Boudouard reaction or the RCG reaction. At temperatures above 700°C these reactions become thermodynamically unfeasible. Simultaneously, the methane cracking reaction becomes feasible so any carbon found in the cell above 700°C would be due to methane

cracking. However, at this temperature the methanation reaction also becomes unlikely so there would be no methane available for cracking to occur, so no carbon is expected to form.

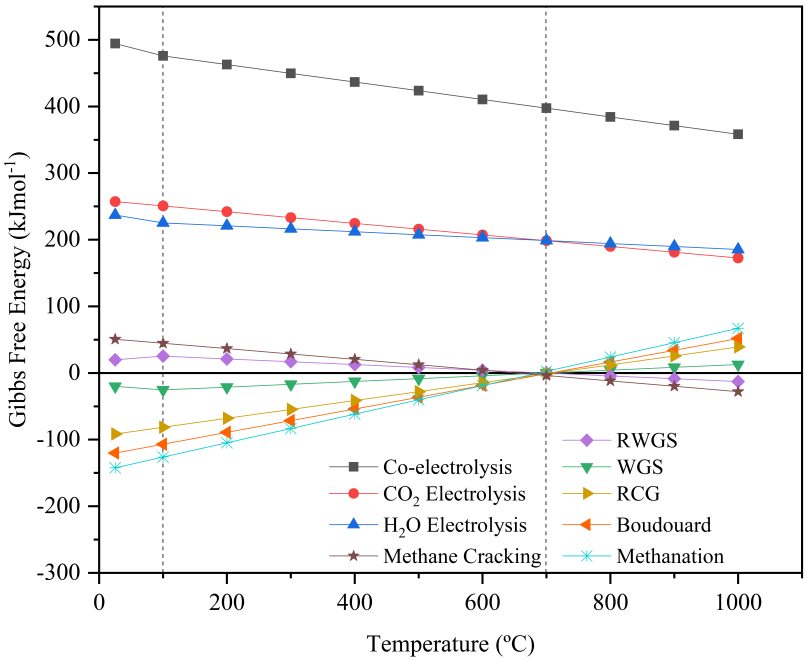


Figure 5.2: Gibbs Free Energies for the reactions taking place during co-electrolysis.

5.2 Chemical Equilibrium Analysis

The thermodynamic equilibrium composition of the co-electrolysis reaction to produce syngas was calculated using the Chemical Equilibrium with Applications (CEA) software of NASA [211]. This programme uses the minimum Gibbs free energy of the reactants to calculate chemical equilibrium compositions and properties of complex mixtures at specified temperature, pressure and fuel inlet composition. The software FactSage [212], was used to produce C-H-O ternary diagrams.

In this section, the equilibrium gas compositions will be calculated from $373.15 \leq T \leq 1273.15$ K, at 1 atm, to investigate the probability of carbon formation on the fuel electrode-

electrolyte boundary during co-electrolysis. The compositions are reported in mole fractions (x_i) and carbon is reported as solid graphite (gr). The programme produces a list of all possible species, including hydrocarbons and alcohols with negligibly low mole fractions. For the calculations in this work a limiting mole fraction of 1.0 x 10^{-3} was set and any mole fractions less than this were not considered to be present.

Again, a fuel composition of 25% H_2O, 25% H_2, 25% CO and 25% CO_2 was chosen in order to investigate the capability of operating the SOCs in reversible mode, generating power from syngas and producing syngas from co-electrolysis.

5.2.1 The effect of temperature change

Figure 5.3 shows the effect of changing the operating temperature of the reactor on the equilibrium composition of co-electrolysis reactants, which were originally 25% CO_2, 25% H_2O, 25% CO and 25% H_2. The equilibrium gas composition fluctuates according to temperature and the Gibbs free energy of the reactions as shown in Figure 5.2. From analysing the change in Gibbs free energies of the reactions with regards to temperature, Figure 5.3 confirms that carbon formation is more likely at lower temperatures, and none is expected at temperatures above 600°C. As research becomes more focused on bringing the operating temperature of these types of cells below 600°C, the formation of carbon at equilibrium will have to be considered in the future [213, 214].

Carbon is formed at these temperatures via the Boudouard and RCG reactions. The most carbon is formed at 400°C, and above this temperature, the amount decreases as CO starts to form from the RWGS reaction. As the temperatures rise above 700°C, H_2O and CO are produced as H_2 and CO_2 are being consumed, which can be explained by the RWGS reaction becoming spontaneous. Below these temperatures the WGS reaction dominates, as can be seen

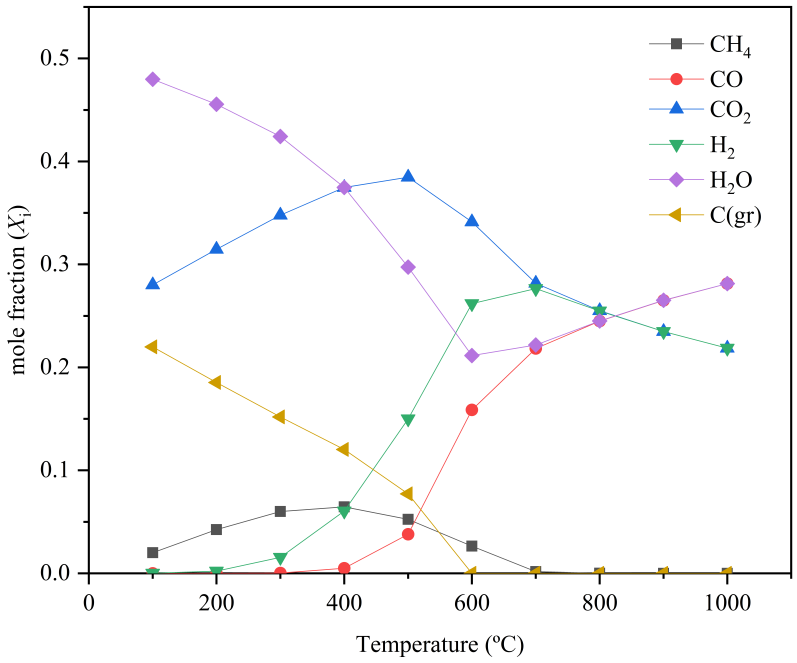


Figure 5.3: Effect of temperature change on gas equilibrium composition of a gas feed composition of 25% CO_2, 25% H_2O, 25% CO and 25% H_2.

by higher H_2 and CO_2 concentrations. Understanding at what process conditions carbon is formed allows targeting of critical testing conditions in order to verify carbon formation in post mortem. From Figure 5.3, it can be seen that to avoid carbon depositing on the cell, it must reach operating temperature before turning on the fuel supply. Similarly, the fuel supply must be turned off and an inert gas passed over the fuel electrode before cooling down of the cell to preserve any carbon formed during the testing sequence, in the state it was formed.

Methane is likely to be present in small quantities at temperatures below 700°C, thereafter the methanation reaction stops being spontaneous. Only at 800°C does the equilibrium composition reflect the actual fuel inlet composition, which should be taken into consideration when investigating the effects of fuel composition on the performance of the cell, and is the reason for choosing 800°C as a reference operating temperature.

5.2.2 The effect of fuel inlet composition change on carbon formation

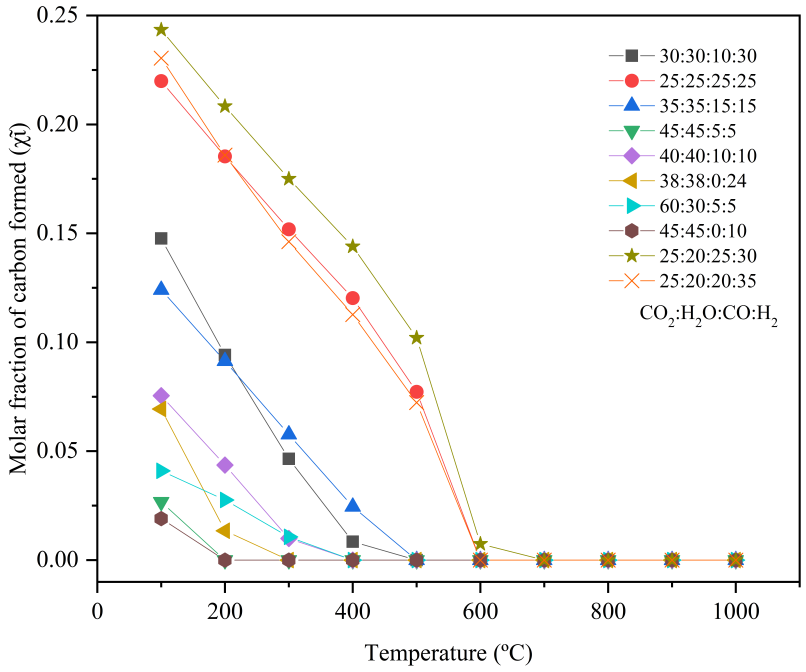


Figure 5.4: Effect of changing the fuel inlet composition on the amount of carbon formed.

Figure 5.4 displays the molar fraction of carbon in the fuel mix for different fuel compositions at equilibrium as a function of temperature. The amount of carbon formed is dependant on the CO:CO_2 ratio. The highest amount of carbon is deposited when the fuel inlet has equal mole fractions of CO and CO_2, but with less water. This can be seen by comparing the two fuel compositions 25:25:25:25 and 25:20:25:30 (CO_2:H_2O:CO:H_2). The reduced water and higher H_2 content creates a more reducing environment, increasing the feasibility of carbon formation.

At temperatures above 600°C, no matter what fuel composition is used, there will be no carbon formed. This is due to the carbon forming reactions no longer being spontaneous above these temperatures. This gives a good indication of the carbon formation threshold at equilibrium, however, in dynamic operation this threshold is likely to shift, meaning that in the

intermediate temperature range, there is a possibility of carbon formation on the cell after all.

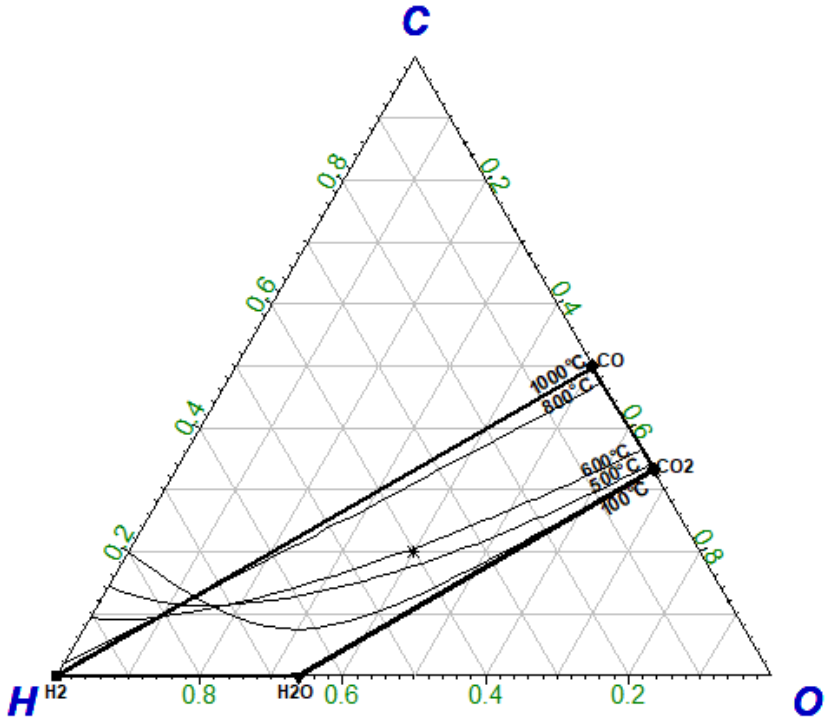


Figure 5.5: C-H-O ternary diagram with carbon deposition thresholds at different temperatures and the co-electrolysis gas composition region. The asterisk indicates the gas composition used in this study (25% H_2O, 25% CO_2, 25% H_2 and 25% CO).

Figure 5.5 shows an equilibrium C-H-O ternary diagram, indicating carbon deposition thresholds at 100°C, 500°C, 600°C, 800°C and 1000°C. The carbon deposition region is the side of the threshold line closest to the C = 1 vertex on the ternary diagram. Five species are marked on the diagram; H_2, H_2O, CO, CO_2 and the gas composition used in this work; 25% H_2O, 25% CO_2, 25% H_2 and 25% CO (labelled with asterisk). The region within the four axis marked by H_2, H_2O, CO and CO_2, denoted by a solid black line, represents the co-electrolysis gas composition region, including all mixtures of H_2, H_2O, CO and CO_2. The data presented in the C-H-O diagram is in agreement with the carbon deposition graph in Figure 5.4, as no carbon is formed at equilibrium at temperatures above 600°C for any of the mixtures compared in Figure 5.4.

5.3 Effect of current density on carbon deposition

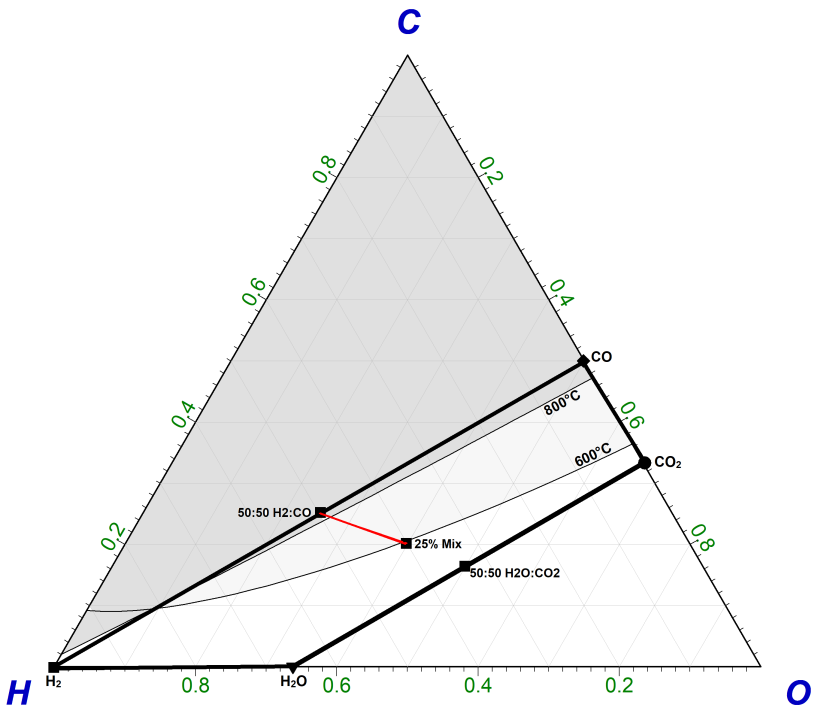


Figure 5.6: C-H-O ternary diagram showing the co-electrolysis gas composition region and the markers for 50:50 H_2:CO and 50:50 H_2O:CO_2. The grey regions indicate the carbon deposition region at 800°C.

In the previous sections, it was established that carbon formation during co-electrolysis is unlikely to occur at temperatures from 600°C to 800°C for the reference fuel feed of 25% CO_2, 25% H_2O, 25% CO and 25% H_2 at equilibrium. However, when considering dynamic operation, high current densities and high conversion result in an increase in the ratio of the products (CO and H_2) to the reactants (CO_2 and H_2O), which results in a more reducing atmosphere at the fuel electrode, making the formation of carbon more likely. This is in agreement with results reported elsewhere [124, 215]. In a similar study in 2019 [216], no carbon was found during intermediate-temperature co-electrolysis (525°C to 700°C), however this can be attributed to a higher oxygen content in the fuel mix (H_2, H_2O, CO_2 and He) compared to the fuel mix in this work.

The products of the co-electrolysis reaction, a mixture of H_2 and CO, have been marked on the ternary diagram in Figure 5.6. Also marked on this diagram is the 50:50 mixture of H_2O and CO_2 and the co-electrolysis gas mixture used in this work (labelled 25% Mix). These markers have been used to illustrate the extent of the co-electrolysis reaction in relation to the carbon deposition region at different temperatures and can be seen in more detail in Figure 5.7.

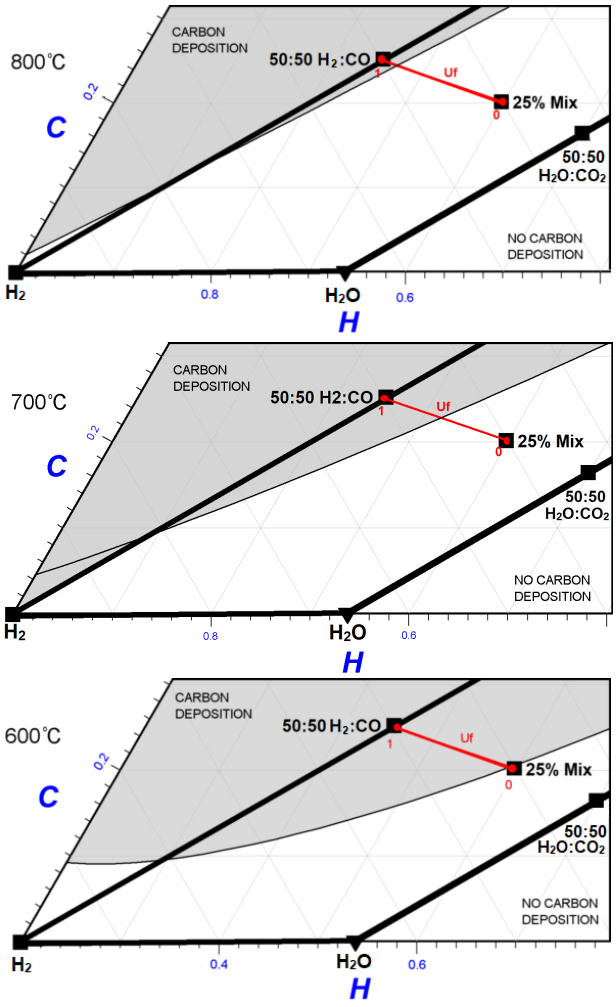


Figure 5.7: The H = 1 vertex of the C-H-O ternary diagram with carbon deposition thresholds at 600°C and 800°C shown. The fuel utilisation for co-electrolysis is superimposed in red.

Figure 5.7 shows the H = 1 vertex of the C-H-O ternary diagram with carbon deposition lines at 600°C, 700°C, and 800°C, and the co-electrolysis gas composition region. The diagrams show the gas composition for 25% H_2O, 25% CO_2, 25% H_2 and 25% CO (labelled 25%

Mix) and the gas composition for 50% H_2, 50% CO (full conversion). The marker for 50% H_2O 50% CO_2 is also visible. The grey areas in Figure 5.7 indicate the carbon deposition thresholds at 800°C, 700°C, and 600°C, respectively. Fuel utilisation, U_f, which relates to the current, has been used here to represent the extent of reduction of H_2O and CO_2 to H_2 and CO, rather than the ratio of operating current to Faradaic current, and has been superimposed onto the ternary phase diagram. At 800°C, the threshold to carbon deposition is crossed before $U_f = 1$. This illustrates the earlier discussion on carbon deposition being more likely at high conversion. At 700°C, the reaction proceeds past the median before the carbon deposition threshold is passed, whereas at 600°C the carbon deposition threshold is crossed as soon as the reaction proceeds. For the fuel composition used in this work, the co-electrolysis reaction at 600°C would be susceptible to carbon deposition, however, at 700°C, which still resides within the intermediate-temperature region, the co-electrolysis reaction can proceed successfully, to some extent, without this type of degradation.

5.4 Summary

Thermodynamic equilibrium calculations have been used as a method of predicting gas compositions and carbon deposition at different temperatures for the co-electrolysis reaction. The trends reveal that at different temperatures different reactions are favoured, which is in agreement with results found in literature.

The general trend in the intermediate temperature range is that there is a turning point at 700°C, after which the RWGS reaction boosts H_2O and CO concentrations. Below 700°C, CO_2 concentration dominates and carbon deposition becomes more likely via the Boudouard reaction. The amount of carbon deposited at equilibrium depends on the amount of CO present and how reducing the environment is. Higher oxygen species concentration (H_2O or CO_2)

makes carbon deposition unfeasible.

The carbon deposition region of C-H-O ternary diagrams has been used to identify the carbon deposition threshold in terms of U_f and operating temperature. It was found that at 800°C, carbon deposition is likely as U_f approaches 1. At U_f = 1 the gas composition in the reactor contains a higher concentration of CO and H_2, making a more reducing environment for carbon deposition to occur. At 700°C, the co-electrolysis reaction can proceed past U_f = 0.5 before the carbon deposition threshold is reached. At 600°C, carbon deposition is likely at much lower U_f values (U_f = 0.1), due to the increased Gibbs energy of carbon forming reactions at reduced temperatures. These investigations are a good starting point for designing experiments where the carbon deposition region needs to be avoided. However, they are limited in that the database uses only one form of carbon (graphite), whereas in real scenarios, more types of carbon are formed; amorphous carbon, carbon fibres, graphite and more.

CHAPTER SIX

CARBON DEPOSITION IN CO-ELECTROLYSIS

This chapter focuses on carbon deposition on the NiSSZ and NiYSZ cells with respect to operating temperature. The cell performance during co-electrolysis in the temperature region 600ºC to 800ºC is evaluated and the carbon deposition thresholds for each material set is identified. The carbon deposition thresholds are translated into concentration of CO in the fuel outlet to align with the thermodynamic thresholds. Ultimately, this gives an indication of how tolerant the ScCeSZ in the fuel electrode cermet is to carbon deposition compared to the conventional YSZ material.

First, carbon deposition in CO_2 electrolysis was examined to identify the characteristic electrochemical changes that occur during this type of degradation. The overpotentials for the three carbon deposition reactions (Boudouard reaction and two electrochemical carbon deposition reactions) were calculated and used to visualise each reaction's contribution at different temperatures. Experimental CO_2 electrolysis tests were used to produce impedance spectra changes corresponding to carbon deposition. This facilitated the identification of carbon deposition in the impedance response for co-electrolysis.

The cells were tested in co-electrolysis mode using a fuel composition of 25% H_2O, 25% CO_2, 25% H_2 and 25% CO. The resulting polarisation curves and impedance plots were compared against each other. Carbon deposition threshold tests were carried out after initial characterisation and the results were compared to the thermodynamic equilibrium calculations carried out in Chapter 5.

Finally, the amount of carbon deposited on each cell after the threshold test was quantified using the temperature programmed oxidation (TPO) technique. TPO was chosen instead of other carbon qualification techniques such as Raman spectroscopy, due to availability of instruments and ease of quantification. Initially, Raman spectroscopy was carried out and characteristic carbon D- and G-peaks were identified on some of the tested cells, but not all. Therefore, it was deduced that the amount of carbon on some of the cells was below the detection limit for this technique, thus TPO was chosen. The observed trends were discussed with respect to operating temperature, fuel electrode material, and current density.

6.1 Carbon deposition during CO_2 electrolysis

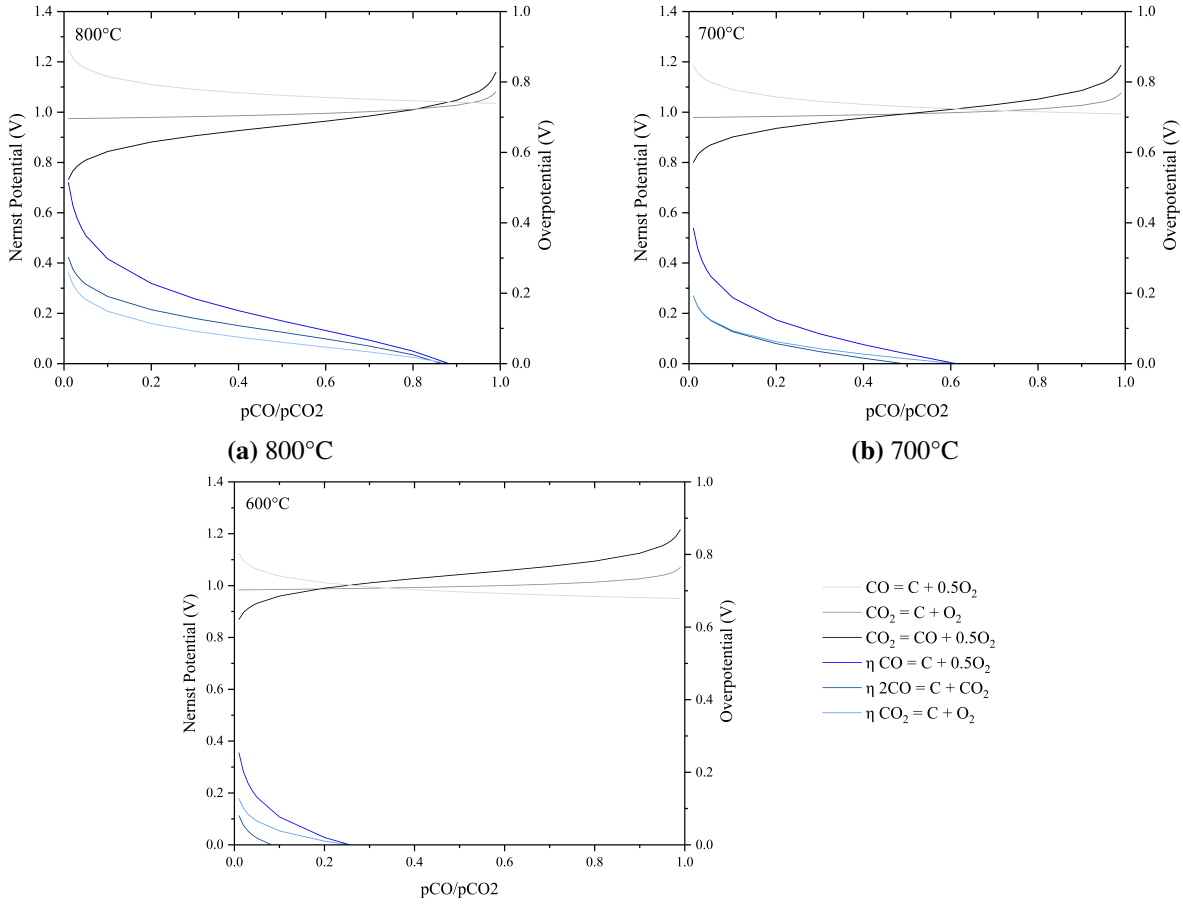
To identify the electrochemical effects of carbon deposition, CO_2 electrolysis tests were carried out in an experimental procedure similar to that of Skafte et al. [217]. By looking at pure CO_2 electrolysis, the effects from any side reactions with H_2, such as the reverse water gas shift (RWGS) reaction, can be excluded, leaving only the effects from carbon-related degradation. The three carbon deposition reactions that could occur during co-electrolysis are the Boudouard reaction (Equation 6.1), or direct electrochemical deposition of carbon (Equation 6.2 and Equation 6.3).

$$2\,CO \longrightarrow CO_2 + C \tag{6.1}$$

$$CO_2 \longrightarrow O_2 + C \tag{6.2}$$

$$CO \longrightarrow 0.5\,O_2 + C \tag{6.3}$$

6.1.1 Thermodynamics of carbon deposition



(a) 800°C

(b) 700°C

(c) 600°C

Figure 6.1: Calculated Nernst potential for the CO_2 electrolysis reaction and two electrochemical carbon deposition reactions. The overpotential for the Boudouard reaction and electrochemical carbon deposition reactions are shown on the second y-axis.

Using the Nernst equation and thermodynamic data, the cell potential for the above three carbon forming reactions was calculated between 600ºC and 800ºC and plotted in Figure 6.1. The difference between this cell potential and the Nernst potential for CO_2 electrolysis to CO and O_2 gives the overpotential required for electrochemical carbon deposition to occur. From look-

ing at Figure 6.1 (a), at 800ºC carbon formation will occur via the Boudouard reaction at OCV when the CO concentration is above 87%. When the CO concentration is less than 87%, carbon formation via the electrochemical reduction of CO_2 is favoured (Equation 6.2). This threshold decreases with temperature. At 700ºC, the Boudouard threshold is 49% CO in CO_2. At 600ºC, the Boudouard threshold surpasses the CO_2 electrochemical reduction threshold and carbon will form via this pathway if the CO concentration is more than 7.9%. These findings are in agreement with experimental data from the literature which found that at lower temperatures (650ºC) carbon was found more evenly distributed throughout the fuel electrode, whereas at higher temperatures (750ºC) carbon formation was found in the 20 microns closest to the electrolyte, where the electrochemical reactions take place, indicating electrochemical carbon deposition at higher temperatures and the Boudouard reaction at lower temperatures [218].

6.1.2 Carbon deposition and EIS

Degradation effects can be detected by observing changes in polarisation and serial resistances from impedance spectra, including the impact of carbon deposition. Increases to the high frequency arc have been observed when switching fuel gas from H_2 to CH_4 [219, 220]. Increases to the low frequency arc (gas diffusion resistance) have been reported to be associated with carbon plugging the pores of the fuel electrode [221]. One study used DRT during co-electrolysis to investigate the changing performance with increasing current density [124]. To the author's knowledge, there are no studies using EIS and DRT to characterise carbon deposition in SOCs during co-electrolysis.

The method of carbon detection consisted of increasing the electrolysis current step-wise at 90 minutes per step until the measured voltage response became unstable and increased independently of the current. This spontaneous voltage increase indicated the operating conditions

where cell degradation and potential carbon deposition occurred. An unstable voltage was defined as a deviation of 10 mV from the average. The average was taken across ten minutes of each step after the voltage response had stabilised (after the first ten minutes). Figure 6.2 shows an example of this type of test where the voltage can be seen to start increasing over the hold time from 1.35 V. For this example, the spontaneous increase in voltage indicates the potential at which carbon deposits change the microstructure of the cell for 50:50 CO_2/CO mixtures at 700ºC. The increase in cell voltage could also be due to the stabilising process of the charge double layer between the electrode and the electrolyte. This could be checked by repeating the test of the same cell, or carrying out the same test using a H_2O/H_2 (carbon free) fuel mix.

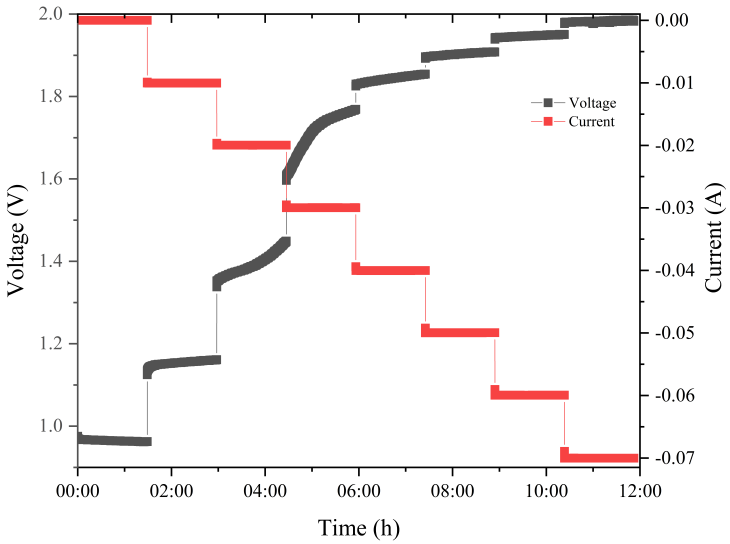
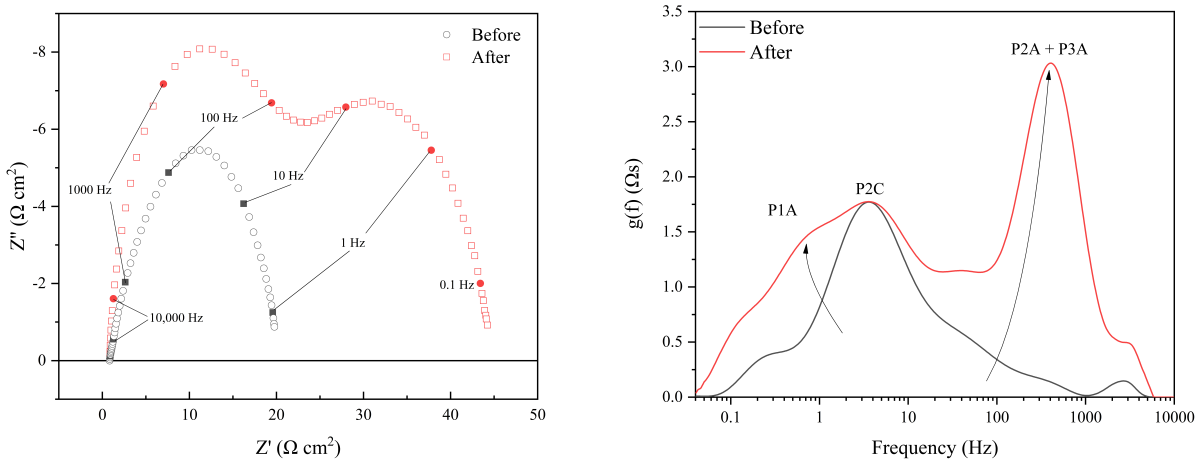


Figure 6.2: CO_2 electrolysis galvanostatic cell test at 700ºC with 0.50/0.50 pCO2/pCO fuel mix used to identify the carbon deposition threshold. The current was increased in 10 mA steps and held for 90 minutes at each step.

Impedance spectra were taken at OCV before and after each cell test to compare the effects of carbon deposition on the individual internal resistance contributions. Carbon deposition during the CO_2 electrolysis reaction can be characterised in EIS as an increase in the charge transfer and gas diffusion overpotentials related to the fuel electrode, as seen in Figure 6.3.

This increase in the high frequency arc seen in Figure 6.3 (a) can be explained by the deposited carbon blocking the TPB active sites and changing the microstructure or, in extreme cases, by areas of delamination between the fuel electrode and the electrolyte. Here, the deposited carbon also increased the gas diffusion resistance by blocking the gas pores, as seen in the increase in the low frequency arc. The corresponding DRT analysis (Figure 6.3 (b)) of the impedance revealed an increase in the peak relating to the coupled process P_{3A} and P_{2A}, charge transfer and ionic transport in the fuel electrode functional layer. The P_{2C} peak is unchanged as the carbon is deposited at the fuel electrode-electrolyte boundary, and does not affect the oxygen electrode. The P_{1A} peak increases slightly as the gas diffusion in the fuel electrode substrate resistance increases, relating to the blocked gas pores.



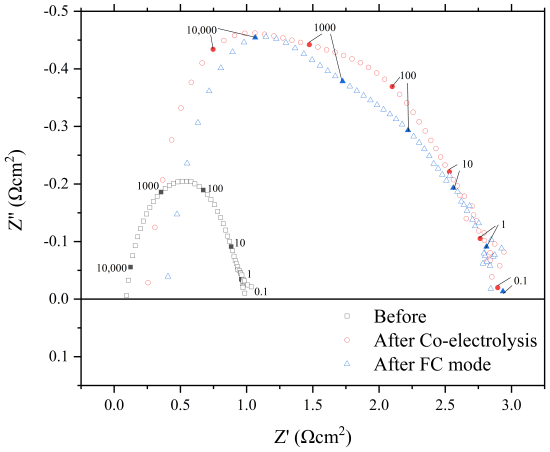
(a) Impedance **(b)** DRT

Figure 6.3: (a) Impedance and (b) corresponding DRT spectra, taken at OCV before and after polarisation curve for CO_2 electrolysis at 700ºC.

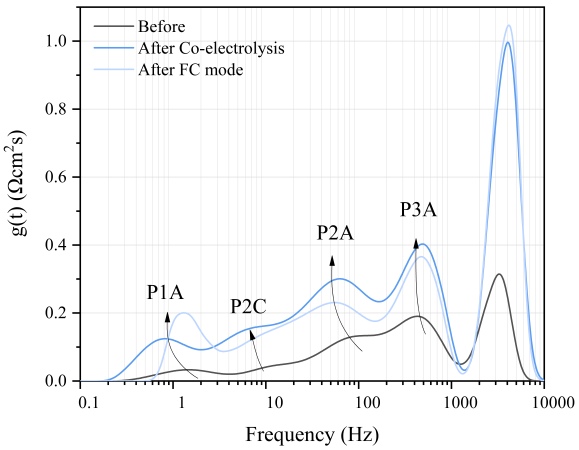
6.1.3 Effect of carbon on EIS spectra in co-electrolysis

Impedance tests were carried out at OCV before and after the carbon deposition threshold tests in order to investigate the effects of high current density and carbon deposition on the cell's resistance. Impedance spectra were converted into DRT to gain further insight into how each of

the different processes within the cell were affected by the co-electrolysis test.



(a) Impedance at OCV before and after carbon threshold tests.



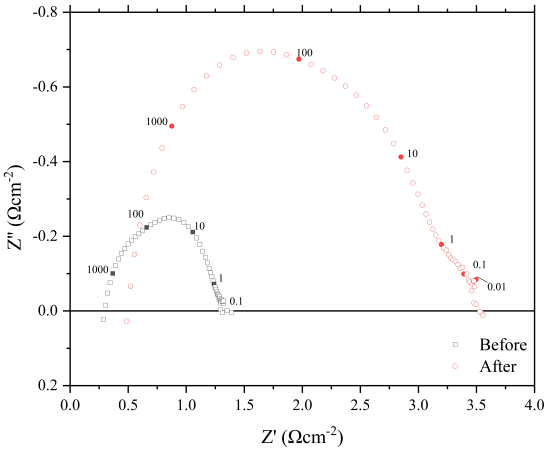
(b) DRT analysis of impedance from (a).

Figure 6.4: (a) EIS taken at OCV and (b) corresponding DRT for NiSSZ cell at 800ºC.

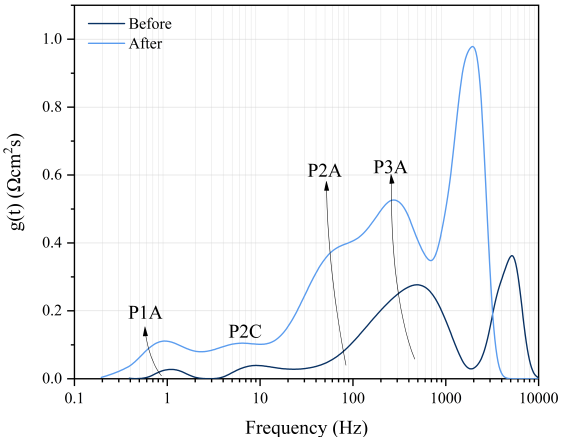
Figure 6.4 (a) shows how the impedance changed for NiSSZ cells at OCV before and after carbon deposition from co-electrolysis at 800ºC. R_s increased from 0.09 to 0.26 Ωcm^2 and R_{pol} increased from 0.89 Ωcm^2 to 2.63 Ωcm^2. After the co-electrolysis test, the test was reversed and the cell was operated in fuel cell mode to see the effects on different internal processes. R_s increased by a further 0.14 Ωcm^2, however R_{pol} decreased from 2.63 Ωcm^2 to 2.5 Ωcm^2 after reversing the current.

The individual changes to internal processes throughout this test are illustrated in the DRT in Figure 6.4 (b). Here it can be seen that after operation in co-electrolysis the processes P_{3A} and P_{2A}, related to the TPB, and process P_{1A}, related to the fuel electrode substrate, had increased. The increase in P_{1A} suggests that carbon had formed in the fuel electrode substrate. After switching to fuel cell mode, this process increased further still, meaning the changes in the fuel electrode substrate remained unchanged by switching modes. On the other hand, the processes that occur at the TPB (P_{3A} and P_{2A}) decreased after operating in fuel cell mode. This demonstrates how the increase in resistance due to carbon at the TPB can be reduced by switching to

fuel cell mode, which increases the concentration of H_2O and CO_2 in the fuel electrode, removing the carbon via oxidation. The P_{2C} process which relates to the oxygen reduction reaction in the LSCF oxygen electrode increased during co-electrolysis, and decreased after switching to fuel cell mode, however, to a lesser extent than the P_{3A} and P_{2A} processes. This oxygen electrode process would not be associated with carbon formation and so this fluctuation can be attributed to the difference in oxygen partial pressure in fuel cell mode and co-electrolysis mode; electrolysis reactions are well known for increasing degradation of the oxygen electrode.



(a) Impedance at OCV before and after carbon threshold tests.



(b) DRT analysis of impedance from (a).

Figure 6.5: (a) EIS taken at OCV and (b) corresponding DRT for NiYSZ cell at 800ºC.

Figure 6.5 (a) shows the equivalent impedance spectra at OCV for NiYSZ cells before and after co-electrolysis testing at 800ºC. A similar impedance response is seen compared to the NiSSZ cells; R_s increased from 0.31 Ωcm^2 to 0.49 Ωcm^2 and R_{pol} increased from 1.35 Ωcm^2 to 3.53 Ωcm^2. The NiYSZ cells had a higher initial R_s, but this increased by approximately the same value (0.17 Ωcm^2) as the NiSSZ cells during co-electrolysis testing. The NiYSZ R_{pol} increased by 2.18 Ωcm^2 whereas the NiSSZ increased by 1.74 Ωcm^2.

The DRT shown in Figure 6.5 (b), revealed discrepancies in the P_{3A} and P_{2A} TPB processes. After operation in co-electrolysis mode, NiYSZ cells have higher resistances in the TPB than

NiSSZ cells, and a similar resistance in the fuel electrode substrate (P_{1A}) to the NiSSZ cells. The resistance related to the LSCF oxygen electrode (P_{2C}) is slightly smaller in the NiYSZ cell than the NiSSZ, which can be attributed to variances in the manufacturing resulting in a slightly thicker or thinner electrode as the difference is small (0.05 $\Omega cm^2 s$). These DRT comparisons between the two cell types can be seen in Figure 6.6.

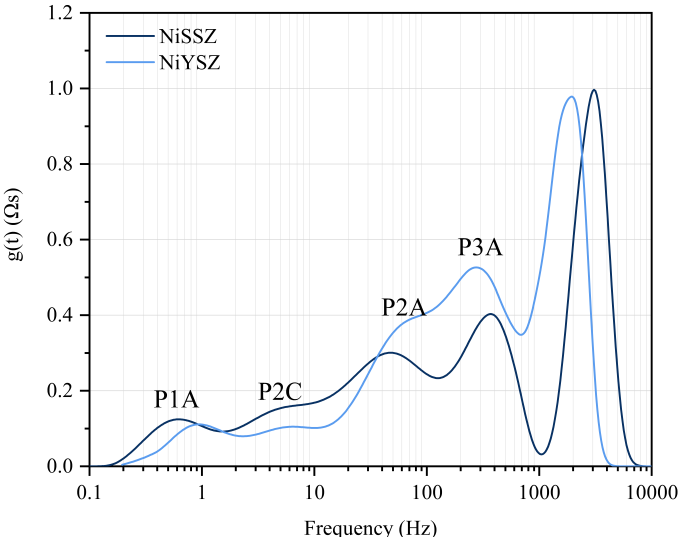


Figure 6.6: Comparison of DRT spectra of NiSSZ and NiYSZ cells after co-electrolysis tests, taken at OCV at 800ºC.

Both NiSSZ and NiYSZ cells have been operated at high current densities in electrolysis mode, which can lead to partial delamination of the electrode and additional peaks in the DRT spectrum. Extra peaks in the high frequency region of the DRT can be due to resistive inter-layers, however the resistive $SrZrO_3$ layer that would be most likely to form in this type of cell would be characterised by an unchanging DRT peak. The peaks seen at high frequency in both the NiSSZ cells and NiYSZ cells have increased after co-electrolysis testing, suggesting a different type of resistance. Delamination of an electrode can be characterised in DRT by an increase in R_s and R_{pol} of a similar extent, which is seen to be the case here. Delamination of the fuel electrode for these cells was later confirmed by SEM analysis.

6.2 Identification of carbon deposition threshold

Theoretically, carbon should not be able to form at 800ºC because the fuel mix used only allows for a maximum pCO = 0.50, and the threshold was calculated to be pCO = 0.80, as shown in Section 6.1.1. It is important to note that using thermodynamics to predict carbon formation can only be used as a guide. Thermodynamic analysis does not take into account the kinetics of the reactions, presence of a catalyst, size of the reactor, or the mechanism for the reaction, which can change the local conditions (pressure, temperature, reactant concentration), thus changing the thermodynamics.

6.2.1 Calculation of pCO at the outlet

The current density at which carbon formed was translated into the concentration of CO at the outlet in order to illustrate the carbon deposition threshold on polarisation curves. pCO was calculated from the Faraday's Law of electrolysis, Equation 6.4, and the ideal gas law, Equation 6.5.

$$n_i = \frac{I}{nF} \tag{6.4}$$

$$n_{gas} = \frac{PV}{RT} \tag{6.5}$$

Where n_i is the molar flow of reactants (mol s^{-1}) converted by the current, I (A), n is the number of electrons transferred in the reaction, F is Faraday's constant (C mol^{-1}), n_{gas} is the molar flow of reactants (mol s^{-1}) at the inlet, P is the pressure (101325 Pa), V is the volumetric flow of reactants (m^3s^{-1}) at the inlet, R is the ideal gas constant ($Jmol^{-1}K^{-1}$) and T is the temperature (K). Fuel utilisation was calculated by Equation 6.6, and the concentration of CO at the outlet, pCO, was calculated by Equation 6.7. Where n_{react} is the molar flow of reactants,

V_{CO} is the volumetric flow of CO in the fuel inlet and V_{total} is the total volumetric flow at the fuel inlet.

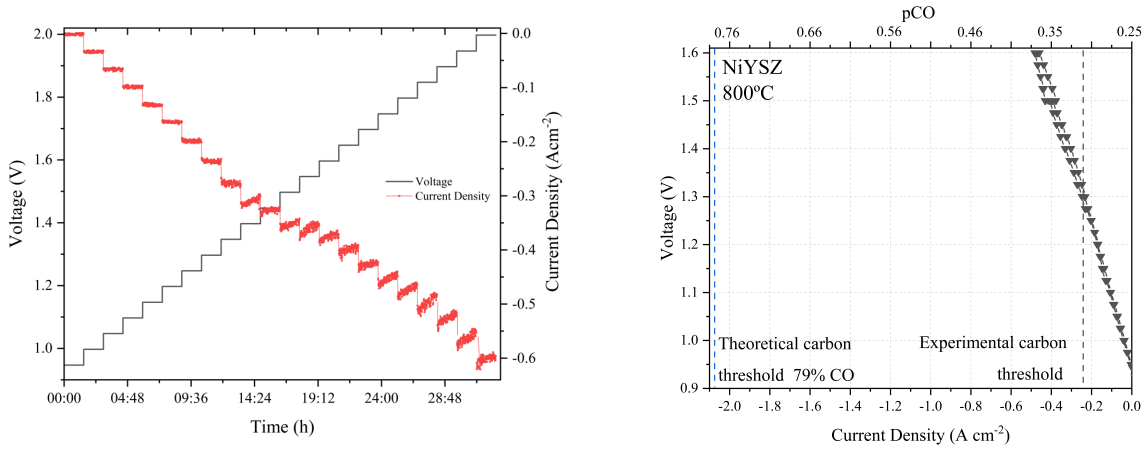
$$U_F = \frac{I}{nF(n_{react})} \tag{6.6}$$

$$pCO = U_F \frac{V}{V_{total}} + \frac{V_{CO}}{V_{total}} \tag{6.7}$$

6.2.2 Comparison of theoretical and experimental carbon deposition threshold

Figure 6.7 (a) shows the electrochemical test carried out to identify the experimental carbon deposition threshold. At 1.4 V the current density loses stability and begins to increase, indicating the onset of carbon deposition. Comparing this to Figure 6.7 (b), which shows a polarisation curve for the co-electrolysis reaction, hysteresis of the curve can be observed at a similar potential of 1.38 V. The difference between these two cell tests was the time the potential was held at each step. For (a) the current was held for 90 minutes at each step, up to a final current density of -0.6 Acm^{-1}, and for (b), each step was held for 60 seconds up to a final current density of approximately -0.5 Acm^{-1}. This implies that the step time taken at each potential does not significantly influence the carbon deposition threshold during co-electrolysis at this temperature.

Carbon was formed at a lower threshold than theoretically calculated, as seen in Figure 6.7 (b), because the local conditions throughout the cell varied from the average current density. An influencing factor in the carbon deposition threshold is the presence of Ni in the fuel electrode, which catalyses the coking reaction. Additionally, electrolysis is an endothermic reaction so it is possible that as the reaction proceeds there is a temperature drop across the cell resulting in conditions more suited for carbon deposition. Finally, at higher current densities there is an increase in the concentration of CO and H_2, resulting in a more reducing environment; a



(a) Cell test to investigate carbon deposition.

(b) Polarisation curve showing hysteresis at similar potential to (a), indicating carbon deposition.

Figure 6.7: Cell tests investigating the carbon deposition threshold at 800ºC for NiYSZ cells. The voltage becomes unstable at 1.3 V as seen in (a) and (b). Theoretical carbon deposition threshold from section 6.1.1 and experimental carbon deposition threshold have been superimposed onto (b).

condition favoured for carbon formation.

At 800ºC the threshold for NiSSZ and NiYSZ cells were 1.54 V and 1.3 V, respectively. For the NiYSZ cells, this threshold decreased steadily down to 1.2 V at 600ºC, following the predicted thermodynamic limits. On the other hand, the threshold for the NiSSZ cells stayed at approximately 1.5 V across the whole temperature range, which would correspond to the similar amounts of carbon formed on all the NiSSZ cells. The threshold graphs for the cell tests at other temperatures all follow the same trend and can be found in Appendix B.

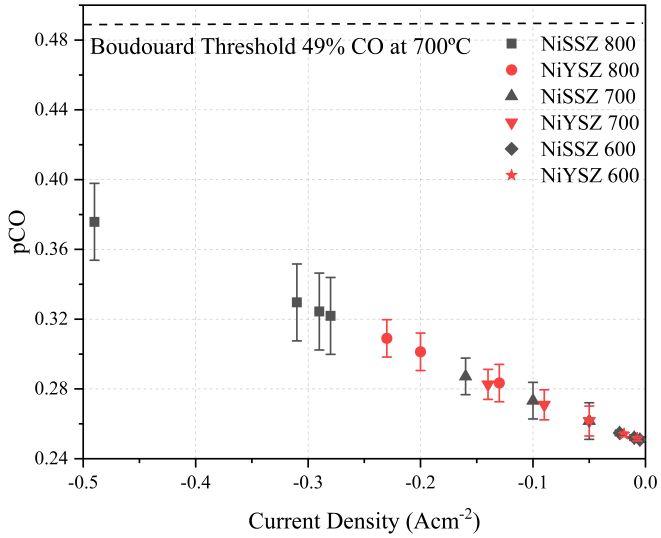


Figure 6.8: The calculated pCO corresponding to carbon deposition for NiSSZ and NiYSZ cells operated between 800ºC and 600ºC as a function of current density.

The points in Figure 6.8 represent where different cells exhibited the onset of carbon formation. For example, at 800ºC the NiSSZ cells could reach a current density of -0.28 Acm^{-2} before the effects of carbon deposition occurred. The point at -0.49 Acm^{-2} represents the cell test described in Figure 6.7 (a), where each current step was held for 90 minutes. This resulted in a higher carbon deposition threshold than if the cell was polarised at a higher rate. The average CO concentration can be seen in Table 6.1. This highlights that at 800ºC NiSSZ cells can operate at 58% higher current density than NiYSZ cells before the onset of carbon deposition. At 700ºC, though, the average threshold was similar, pCO = 0.2740 versus pCO = 0.2717 for NiSSZ and NiYSZ, respectively.

Table 6.1: Average values of pCO at which the onset of carbon formation occured for NiSSZ and NiYSZ cells across the temperature range 800ºC to 600ºC.

Temperature (ºC)	NiSSZ	NiYSZ
800	0.3379 ± 0.022	0.2979 ± 0.011
700	0.2740 ± 0.011	0.2717 ± 0.0086
600	0.2526 ± 0.0016	0.2528 ± 0.0013

In the given fuel composition of 25% H_2O, 25% CO_2, H_2, and 25% CO, at 600ºC carbon formation is thermodynamically inevitable, however, the conductive properties of carbon mean that small amount of deposits will actually improve the cell performance before detrimental amounts are accumulated. This is well illustrated in Figure 6.9 where the current increases in the green region from approximately -0.3 Acm^2 before decreasing in the grey region from approximately -0.6 Acm^2. This reduces the accuracy of the carbon threshold cell tests at lower temperature because the carbon is already present on the fuel electrode at the start of the test so instability or fluctuations in the current are less obvious.

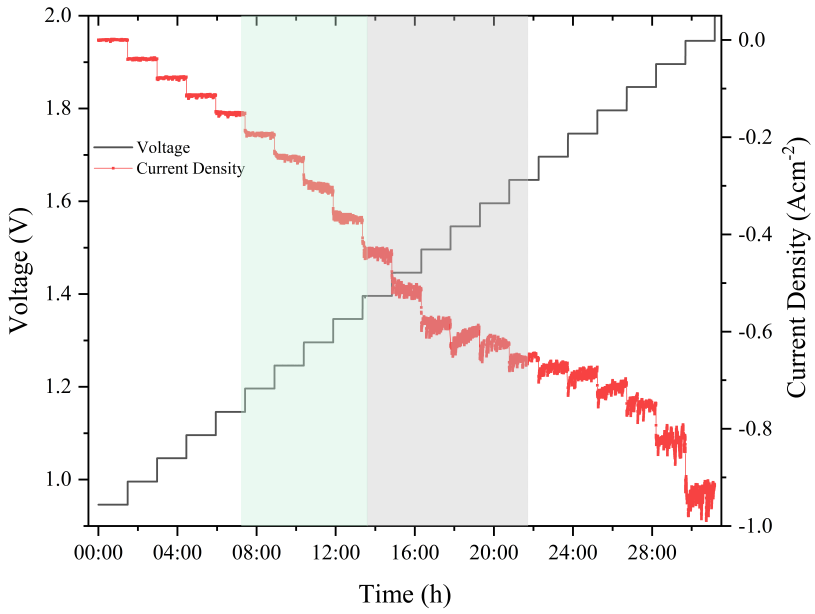
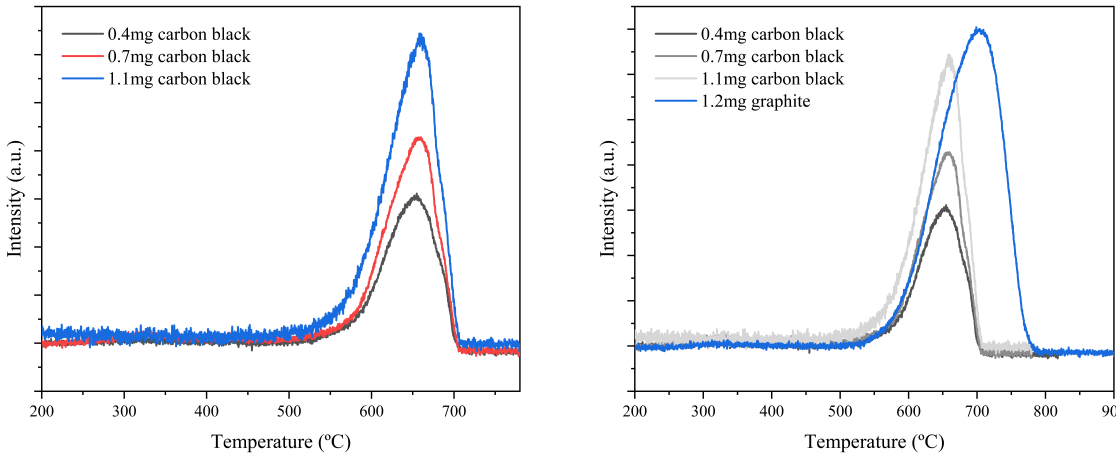


Figure 6.9: Cell test showing how carbon formation causes initial increase in performance (from -0.3 Acm^2) before detrimental effect (from -0.6 Acm^2).

6.3 Characterisation of carbon deposits



(a) Carbon black calibration standards.

(b) Graphite TPO peak.

Figure 6.10: TPO peaks for (a) the three carbon black calibration standards, and (b) graphite.

TPO was used to quantify the amount of deposited carbon on each cell. Figure 6.10 (a) shows the resulting peaks from the calibration standards using carbon black, an amorphous carbon, and Figure 6.10 (b) shows the comparison to using graphite, a more ordered carbon. There are many factors which affect the oxidation temperature of carbon, including morphology and how dispersed the carbon is. Graphite oxidises at a higher temperature due to being more highly ordered, and therefore less reactive, resulting in fewer specific surface active sites. Amorphous carbon is disordered with a larger surface area, so has more surface active sites for the oxidation of carbon to proceed, therefore resulting in a lower oxidation temperature. Using known quantities of carbon black for the calibration standards facilitated the quantification of deposited carbon on the NiSSZ and NiYSZ cells, post-mortem.

6.3.1 Effect of temperature on amount of deposited carbon

Figure 6.11 shows the mass of deposited carbon as a function of temperature for the two types of cells, NiSSZ and NiYSZ. The range between minimum and maximum values of carbon deposits

across all temperatures for the NiSSZ cells was m = 0.27 mg of carbon, whereas the NiYSZ cells had a higher range of m = 0.95 mg carbon. The average deposits for each cell are shown in Table 6.2. The amount of carbon formed at each temperature for both material sets varied significantly. This could be due to slight variances within the microstructure from cell to cell, resulting in a different surface area of nickel exposed for the coking reaction. Another possibility could be deviations in the temperature of the cell, causing the carbon deposition threshold to shift. To improve the accuracy of these results a higher resolution technique to get a more accurate carbon reading should be used, or improved cell testing rig conditions. Nevertheless, a clear trend can be observed; the amount of carbon deposited on the fuel electrode decreased with temperature for both material sets, with considerably more carbon depositing on NiYSZ cells than NiSSZ cells across the full temperature range.

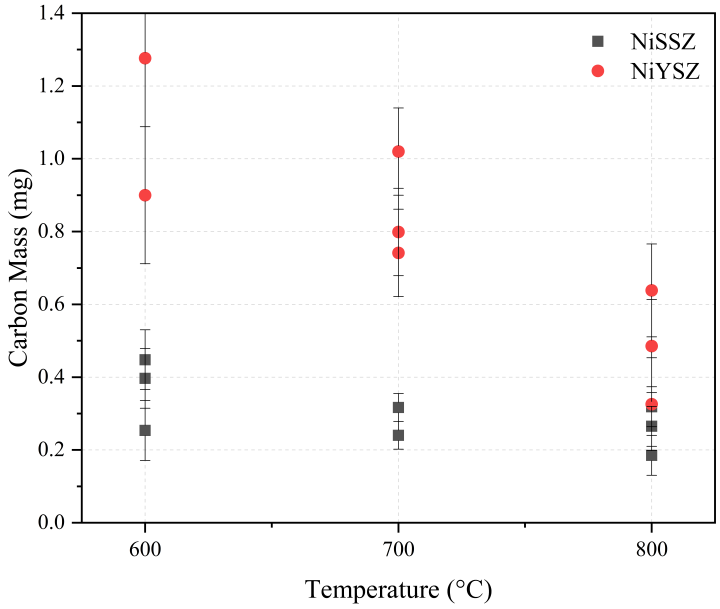


Figure 6.11: Quantified carbon deposits from NiSSZ and NiYSZ cells tested in co-electrolysis mode between 600°C and 800°C.

Table 6.2: Average mass of carbon for NiSSZ and NiYSZ cells at different operating temperatures.

Temperature (ºC)	Mass of deposited carbon (mg)	
	NiSSZ	**NiYSZ**
800	0.2563 ± 0.05484	0.4831 ± 0.1277
700	0.2785 ± 0.03819	0.8536 ± 0.1200
600	0.3660 ± 0.08224	1.088 ± 0.1882

The main differences in carbon deposits are seen at 600ºC, where the average amount of deposited carbon for NiYSZ (1.09 mg) is significantly higher than that for the NiSSZ cells (0.37 mg). In comparison, the average amount of deposited carbon at 800ºC was 0.48 mg and 0.26 mg for NiYSZ and NiSSZ cells, respectively. This reveals that the carbon resistant qualities of ScCeSZ are recognised across all temperatures but prove a significant benefit at temperatures below 800ºC when compared to conventional NiYSZ cells.

Linking Figure 6.11 to Figure 6.8, it can be concluded that the NiSSZ cells can operate at 58% higher current density at 800ºC whilst exhibiting approximately half the amount of carbon deposits. Operating the cells at 700ºC and 600ºC resulted in approximately three times the amount of carbon on the NiYSZ cells than the NiSSZ cells for both temperatures. The average concentration of CO at which carbon formation occurred for these cells was similar, at approximately 0.27 CO, which translates to 0.11 Acm^{-2}, or just outside of OCV.

6.3.2 Effect of temperature on type of deposited carbon

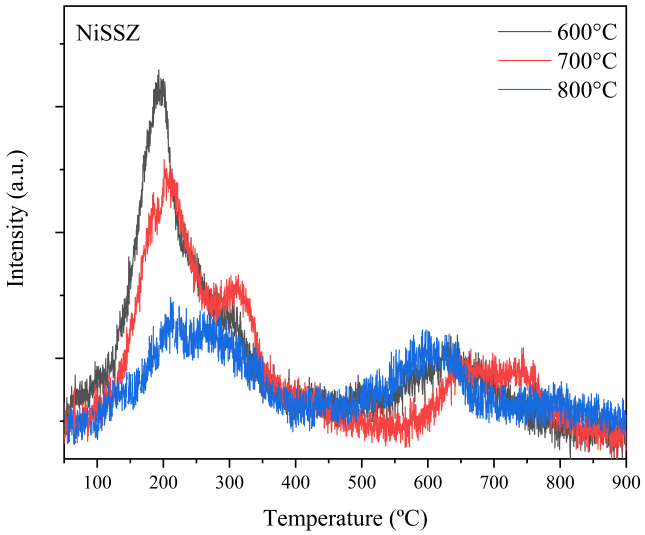


Figure 6.12: CO_2 peaks from TPO analysis of the NiSSZ cells.

The TPO profile of carbon found on the NiSSZ cells (Figure 6.12) shows that two main types of carbon were formed during co-electrolysis; one with an oxidation temperature of approximately 200°C and another with a higher oxidation temperature of approximately 600°C. Comparing this TPO profile to the one of carbon black and graphite for the calibration in Figure 6.10, we can say that the carbon formed during co-electrolysis is highly disordered and sparsely deposited as it has a lower oxidation temperature than carbon black. The low oxidation temperature can be explained by carbon deposits near to any Ni particles in the fuel electrode, which will oxidise at a lower temperature, due to the catalysing effects of the Ni. Finally, this low temperature peak could also be attributed to carbon fibres, which have been shown to oxidise at low temperatures [119]. This is also in agreement with observations from SEM which showed large amounts of fibrous or rod-shaped carbon deposits. This will be discussed further in a later section.

Changing the operating temperature of co-electrolysis cells affects the type of carbon that is formed. Lower operating temperatures result in more amorphous carbon whereas at higher

temperatures the deposited carbon is a mixture of amorphous and graphitic carbon, seen in the additional small peak at higher temperatures. This is in agreement with the literature which describes fibrous or amorphous carbon deposits being formed predominantly at lower temperatures, and graphitic carbon characteristically formed at higher temperatures [119].

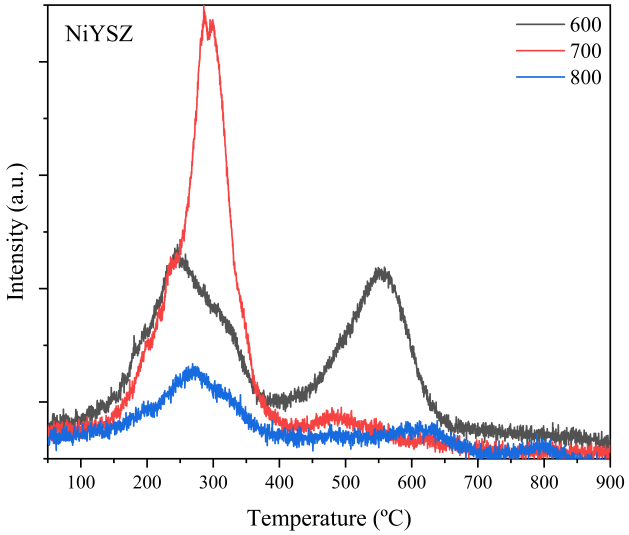


Figure 6.13: TPO profile from NiYSZ cells.

For the NiYSZ cells (Figure 6.13), the total amount of carbon deposited at 600ºC was still more than that deposited at 700ºC or 800ºC, however, the double peak for the cell tested at 600ºC shows that more ordered carbon formed at the lower temperatures rather than the higher temperatures, as with NiSSZ cells. The second peak at 550ºC had an oxidation temperature lower than that of graphite (>700ºC) so it was still amorphous carbon, but had a different morphology to the other amorphous peak at 250ºC. Furthermore, the profile for 700ºC shows a sharp peak at 300ºC, indicating the presence of a more homogeneous carbon. The TPO profile for 800ºC reveals a further small peak at 800ºC, indicating the deposition of more graphitic carbon at higher temperatures.

Figure 6.12 and Figure 6.13 reveal that the peaks at 200 to 300ºC correspond to amorphous carbon deposited around the Ni, covering the TPB, the peak in the region of 500 to 600ºC is

from filamentous carbon, which is typically more ordered than amorphous carbon, and the small peak at 800ºC can be attributed to graphitic carbon. These conclusions can be corroborated with SEM images in Section 6.3.2.1.

6.3.2.1 SEM images of carbon formed at different temperatures

SEM was used to investigate the changes in the cell microstructure after testing in co-electrolysis. Deposits of carbon were observed in the form of carbon fibres, carbon flakes and amorphous carbon. Ni can be identified from the SEM images as the component that appears brighter and with a rough surface, whereas the zirconia (SSZ or YSZ) can be identified as the darker, smoother component.

At lower operating temperatures amorphous carbon formation on the Ni catalyst occurs, whereas higher temperatures favour more stable graphitic carbon deposits, including carbon fibres and carbon nanotubes (CNT). Amorphous and graphitic carbon tend to cover the surface of the Ni catalyst and reduce its activity, whereas carbon fibres tend to lead to crack formation, and have less of an effect on the Ni catalyst. The mechanism for carbon fibre formation onto Ni catalyst that is widely accepted in the literature involves three steps: (1) deposition of carbon on the Ni surface, (2) dissolution of the carbon into the bulk of the Ni, and (3) the precipitation of carbon as a fibre. Fibre growth can cause cells to fracture because of the mechanical stresses induced by the growth of the fibres [105].

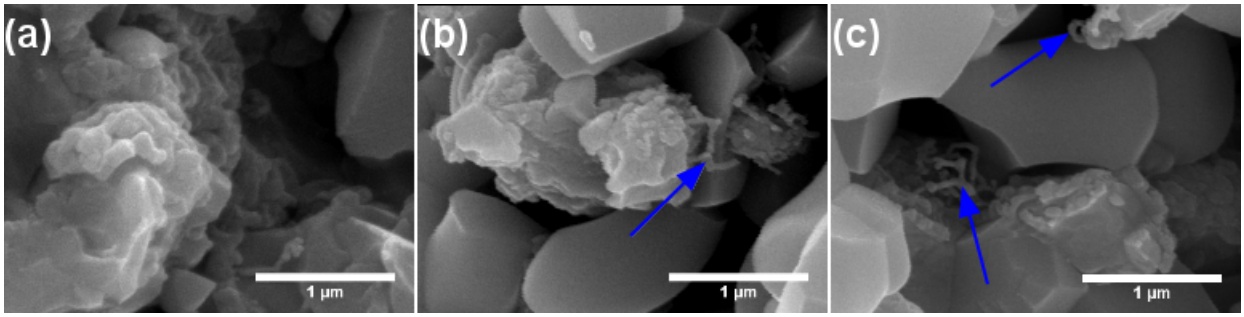


Figure 6.14: SEM images of NiSSZ cells showing different types of carbon that was deposited at operating temperatures of (a) 800ºC, (b) 700ºC, and (c) 600ºC.

Figure 6.14 shows the SEM image of the fuel electrode of NiSSZ cell after co-electrolysis at 800ºC, 700ºC and 600ºC. Figure 6.14 (a) reveals that the carbon deposition at 800ºC was so minimal it was difficult to locate during SEM. TPO results for this cell also confirmed minimal carbon deposits. At 700ºC, carbon could be found at the TPB sites in the pores surrounding the Ni and SSZ boundary in the form of carbon fibres. Figure 6.14 (c), which shows a cell tested at 600ºC, reveals higher amounts of carbon fibres were concentrated in the fuel electrode. It was noticeable by simple observation of SEM how the quantities of carbon deposits increased with decreasing operating temperature.

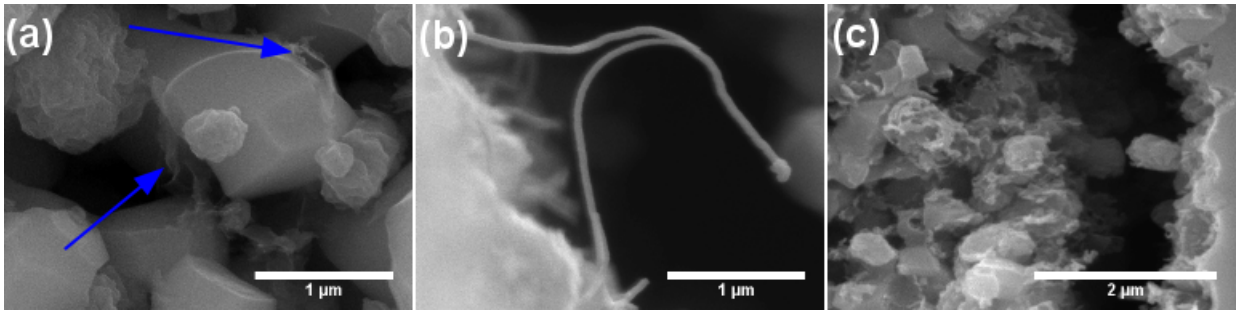


Figure 6.15: SEM images of NiYSZ cells showing different types of carbon that were deposited at operating temperatures of (a) 800ºC, (b) 700ºC, and (c) 600ºC.

The different types of carbon were more noticeable on the NiYSZ cells than NiSSZ cells due to the higher quantities of carbon found. At 800ºC, the carbon was located at the first 2µm of the TPB, predominantly found surrounding the YSZ, as seen in Figure 6.15 (a). The

carbon here took on the flake morphology, which is typically known to be a more graphitic carbon. This is in agreement with the TPO profile for NiYSZ cells operated at 800ºC which showed oxidation peaks at 600ºC and 800ºC. The carbon formed at 700ºC (Figure 6.15 (b)) was located at the site of delamination between fuel electrode and electrolyte on a NiYSZ cell. This image was taken after the carbon deposition threshold test and shows how severe carbon deposition can result in total delamination and destruction of the cell. Carbon fibres were found along the boundary in the first one to two µm of the fuel electrode. The carbon here consisted of two fibres joining together at a nanoparticle, which EDX analysis (shown in Table 6.3) revealed to consist predominantly of zirconia; suggesting that the carbon fibres originated from a zirconia base and not Ni, as previously thought. Thermodynamic calculations in the previous section highlighted that the predominant carbon deposition reaction at this operating temperature would be electrochemical carbon deposition. This can be used to explain why the carbon formed at these TPB sites - the sites where electrochemical reactions occurred. In this instance, as the carbon fibre built, it expanded the volume of the fuel electrode, ultimately leading to delamination.

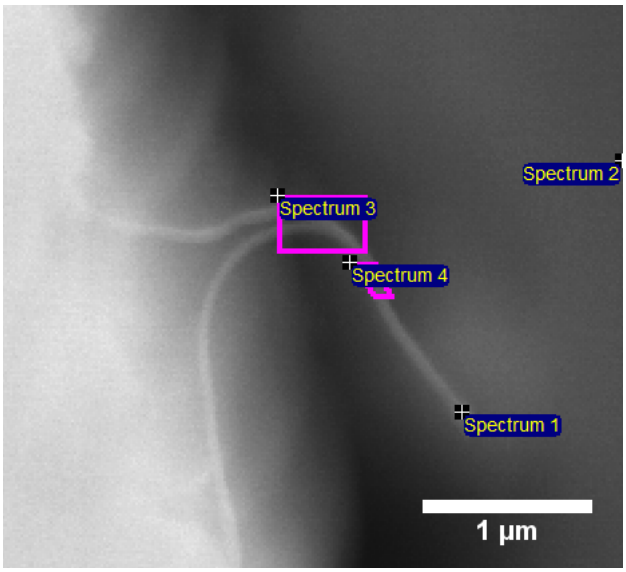


Figure 6.16: Locations of EDX spectra.

Table 6.3: EDX results from carbon fibre image in Figure 6.16.

Spectrum	C	O	Ni	Zr
Spectrum 1	34.04	13.41	14.44	38.11
Spectrum 2	25.60	15.00	5.17	54.23
Spectrum 3	33.27	11.77	19.34	35.62
Spectrum 4	31.56	12.95	16.93	38.56

Delamination of the fuel electrode also occurred for the NiYSZ cell tested at 600ºC (Figure 6.15 (c)), however, no carbon fibres were observed, only amorphous carbon covering the TPB. It appears that the amorphous carbon formed at 600ºC covered both the Ni and the zirconia, rather than just the zirconia, which was seen at higher temperatures. Referring back to thermodynamics, at this temperature the Boudouard reaction becomes the more likely carbon deposition reaction, which explains why the carbon can be seen on the Ni as well as the zirconia.

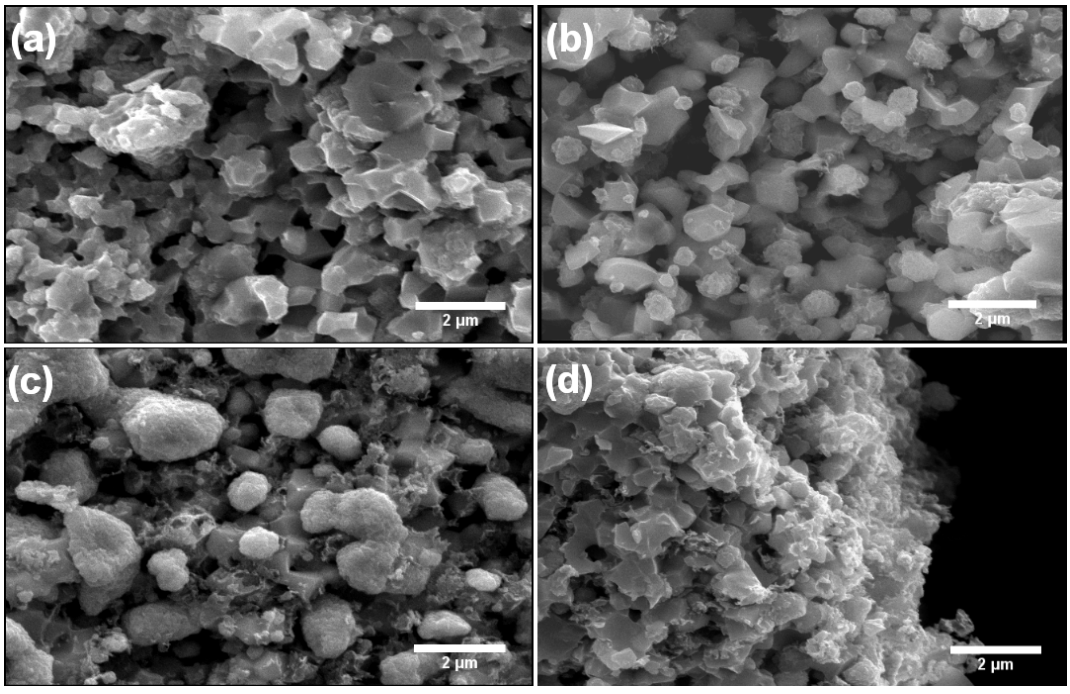


Figure 6.17: SEM images of NiYSZ cells showing different stages of carbon deposition due to operating temperature. (a) shows a BoL fuel electrode to compare to the fuel electrode of cells after co-electrolysis tests at (b) 800ºC, (c) 700ºC and (d) 600ºC.

Figure 6.17 shows SEM images of the fuel electrode surface of four different cells; (a) a

reduced fuel electrode, and the rest show fuel electrode surfaces after co-electrolysis testing at (b) 800ºC, (c) 700ºC, and (d) 600ºC. These images illustrate how carbon deposition becomes more extensive as the operating temperature decreases, leading to reduced porosity as the carbon gradually covers the fuel electrode TPBs, ultimately leading to complete cell deactivation.

6.4 Summary

In this chapter it was shown that carbon deposition during co-electrolysis can occur outside of the predicted thermodynamic limits, even at elevated temperatures. The carbon deposition thresholds were estimated by thermodynamic calculations, which indicated deposition could occur at OCV where the concentration of CO reached 87%, 49% and 7.9% at 800ºC, 700ºC and 600ºC, respectively. For the experimental conditions in this work, which included a fuel mix of 25:25:25:25 CO_2:H_2O:CO:H_2, theoretically, carbon could only form at 600ºC. The method used to identify the experimental carbon deposition threshold revealed significant differences in the theoretical and experimental threshold. NiSSZ cells had a higher threshold than NiYSZ cells across all operating temperatures, but showed significant advantages at 800ºC where the amount of carbon deposits was almost half of that found on equivalent NiYSZ cells at 58% higher current density.

TPO experiments revealed that changing the operating temperature of the cells resulted in different carbon morphology; carbon fibres, flakes, and amorphous carbon. No definitive conclusions could be drawn from the types of carbon formed on NiSSZ compared to NiYSZ cells, other than at lower operating temperatures more amorphous carbon formed and more ordered, graphitic carbon formed at higher operating temperatures. To accompany the TPO results, SEM images showed carbon fibres formed in the boundary between fuel electrode and electrolyte, particularly when delamination of the electrode occurred. Carbon fibres found showed zirco-

nia nanoparticles present at the end of the fibre, indicating that they originated from a zirconia particle. At 800ºC, carbon typically formed around the zirconia, rather than the Ni, which is indicative of electrochemical carbon deposition. At lower temperatures, the carbon was found at the TPB in between Ni and Zr, suggesting a transition from electrochemical carbon deposition to the Boudouard reaction for carbon formation at lower temperatures.

CHAPTER SEVEN

CONCLUSIONS

Two methods for manufacturing fuel electrode supported solid oxide cells (SOC) were developed in the study reported here. Both methods utilised the technique of reverse aqueous tape casting. One method involved tape casting the GDC barrier layer, and the other method spin coated the GDC barrier layer. The effect of pore former and sintering temperature was investigated between 1300 and 1400ºC. It was found that less pore former was required for the NiSSZ cells than the NiYSZ due to differences in particle size, which resulted in a denser microstructure of the NiYSZ cells after sintering. The thickness of each sintered layer was reduced to 4 μm, which was found to be the limit of the tape casting equipment. This resulted in pin holes in the layers as they dried, so the thickness was increased in order to create homogeneous layers. The thickness of all layers needed to be minimised because of the addition of a new composite layer, which was used to reduce the mismatch of thermal expansion coefficient between the zirconia electrolyte and the barrier layer. This TEC mismatch was identified as the reason for the initial GDC delamination. Cells made via this five-layer tape casting method were the first of their kind and were successful in their objective of mitigating GDC delamination from the electrolyte. These cells showed good performance but had a high ohmic resistance (0.31 Ω cm^2) and a high degradation rate, so were not used in the rest of this work. The high R_{ohm} was a

result of the additional composite layer and not being able to reduce the tape cast layers to less than 4 μm.

To overcome the limits of the tape casting equipment, cells were made in the same way as the previous method, but the GDC barrier layer was spin coated onto a pre-sintered half cell. Optimising the speed of the spin-coater resulted in a homogeneous GDC barrier layer with sintered thickness <4 μm (2.80 μm). These cells successfully mitigated GDC delamination. Sintering the GDC separately had the added benefit of reducing the GDC sintering temperature, so that no insulating layers formed between the GDC and the electrolyte. The reduction in cell thickness resulted in a lower R_{ohm} (0.12 Ω cm^2), and good performance across all temperatures, so these cells were used for further tests in the rest of this work. Cells were made from two material sets: Firstly, Ni/ScCeSZ fuel electrode, ScCeSZ electrolyte, GDC barrier layer, LSCF-GDC/LSCF double-layer oxygen electrode and secondly Ni/YSZ fuel electrode, YSZ electrolyte, GDC barrier layer, LSCF-GDC/LSCF double-layer oxygen electrode. The cells were labelled NiSSZ and NiYSZ, respectively. By making the same type of cells but with differing ionic conductivity component (ScCeSZ versus YSZ), the effect of the ScCeSZ material in terms of conductivity and carbon tolerance in the fuel electrode was identified.

NiSSZ cells were characterised in fuel cell mode and electrolyser mode by testing in H_2/N_2, H_2O/H_2 and $CO_2/H_2O/CO/H_2$ fuel mixtures. Electrochemical Impedance Spectroscopy (EIS) was used to calculate ASR values in each testing mode. Both the NiSSZ and NiYSZ cells made in-house performed better than commercial NiYSZ cells when initially tested in fuel cell mode at 800ºC. Power densities at 0.7 V reached 0.32 W cm^{-2}, 0.35 W cm^{-2}, and 0.28 W cm^{-2} for NiSSZ, NiYSZ and commercial NiYSZ cells, respectively. Nevertheless, NiSSZ cells outperformed NiYSZ cells during testing in co-electrolysis fuel mixtures (25% $CO_2/H_2O/CO/H_2$).

In co-electrolysis mode, at an operating potential of 1.3 V, NiSSZ cells reached current densities of 0.34 Acm^{-2}, 0.16 Acm^{-2}, and 0.06 Acm^{-2} at 800ºC, 700ºC and 600ºC, respectively. Whereas, NiYSZ cells reached current densities of 0.25 Acm^{-2}, 0.1 Acm^{-2}, and 0.05 Acm^{-2} at 800ºC, 700ºC and 600ºC, respectively. NiSSZ cells performed better in comparison to NiYSZ in co-electrolysis and fuel cell mode, with particular benefit seen at reduced temperatures in fuel cell mode.

Thermodynamic equilibrium calculations predicted that for the fuel composition used in this work, carbon deposition is likely to occur at 600ºC, even at OCV. At 700ºC and 800ºC, carbon deposition is likely only as the reactions proceed, with the carbon threshold being crossed earlier at lower operating temperatures. At 800ºC, carbon will form at OCV via the Boudouard reaction when the CO concentration reaches 87%. At 700ºC, this Boudouard threshold drops to 49% pCO, and at 600ºC, it is only 7.9% pCO. Of the three carbon forming reactions at play here (Boudouard reaction and two electrochemical carbon deposition reactions), the Boudouard is the most likely reaction mechanism at 700ºC and 600ºC. At 800ºC, the electrochemical carbon deposition reaction (Equation 7.1) dominates:

$$CO_2 -> C + O_2 \tag{7.1}$$

Theoretical and experimental carbon deposition thresholds were calculated for both NiSSZ and NiYSZ cells. The carbon threshold for NiSSZ cells was higher than that for NiYSZ cells across all temperatures. At 800ºC, NiSSZ operated at a 58% higher current density than NiYSZ cells, and had almost half the amount of carbon deposits. At 700ºC and 600ºC, the amount of carbon found on NiYSZ cells was three times higher than that found on NiSSZ cells. This illustrates how the carbon resistant qualities of ScCeSZ are more convincing at lower operating

temperatures.

Carbon was found on all cells operated in co-electrolysis mode via SEM and TPO test. Greater amounts of amorphous carbon were found on both types of cells which were operated at the lower end of the temperature range. At higher temperatures, more ordered carbon deposits were found. There was no distinguishing difference in the types of carbon formed on NiSSZ cells compared to NiYSZ cells. SEM revealed carbon fibres and carbon flakes in the fuel electrode. In cells operated at 800ºC, carbon was found in the fuel electrode functional layer, in the first few microns from the electrolyte, usually around a zirconia particle. This confirmed predictions that at these temperatures carbon is formed from electrochemical carbon deposition reactions. At lower temperatures, carbon was more evenly spread across a larger area of the fuel electrode and was not positioned on zirconia particles but was found close to Ni as well, indicating the transition to carbon formed by the Boudouard reaction. EDX of the carbon fibres showed zirconia nanoparticles at the ends of the fibres, indicating that they originated from a zirconia particle, not Ni, which had been previously assumed.

NiSSZ fuel electrode supported cells have been shown to be effective in mitigating carbon deposition during co-electrolysis reactions. The benefit of these cells in comparison to the conventional NiYSZ cells has been proven across all intermediate temperatures, and a variety of gas mixtures, but is most pronounced at temperatures below 700ºC. The increased performance of NiScCeSZ cells makes it a sensible choice when designing and manufacturing intermediate-temperature SOCs.

Further work comparing the cost of the materials for cell/stack production, or the increased syngas production due to higher achievable current densities without risk of carbon deposition would be advantageous. Consequently, a more real-world benefit of ScCeSZ as a fuel electrode

material in solid oxide cells could be realised.

7.1 Further Work

This work has characterised the Ni/ScCeSZ material set in different operational modes and has begun to quantify its carbon resistant benefits. It therefore provides a starting point for further research into the Ni/ScCeSZ material's properties and opens up other research opportunities into SOCs fuelled by carbonaceous fuels. Some potential research avenues are described below.

- Further research into the time dependence of carbon formation at certain voltages would highlight the fuel electrode's ability to resist carbon formation in more detail. With this, identifying to what extent carbon can be deposited in co-electrolysis mode and the reverse operation still be able to oxidise and remove the carbon. This, coupled with strong carbon deposition identification parameters, would allow for a self-regenerative rSOCs.

- Develop techniques that utilise Raman spectroscopy to help identify the degree of graphitisation (IG/ID) so the amount and types of carbon (amorphous or graphitic) can be examined in detail.

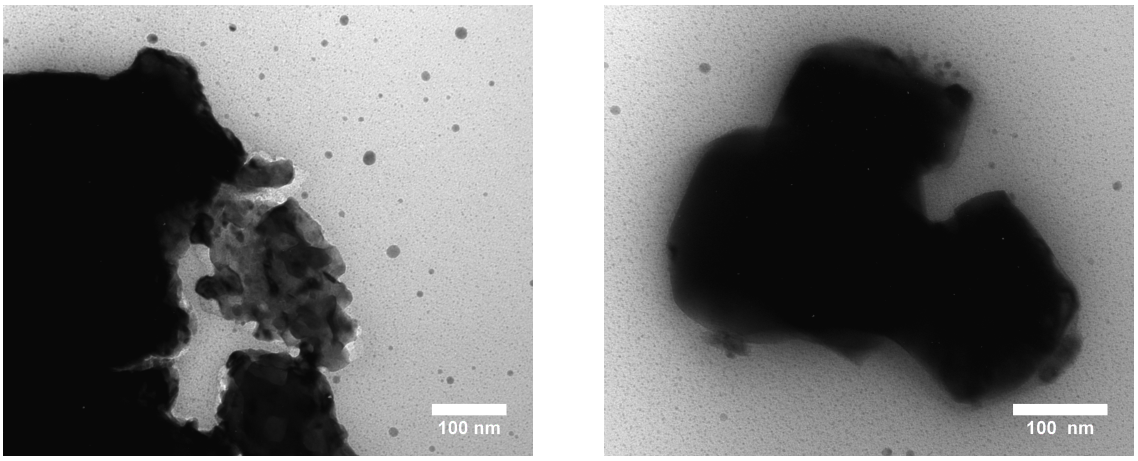
- Long-term testing of NiSSZ cells in co-electrolysis mode are required to reliably calculate the degradation rate (%/1000 hours) at an industry standard potential suitable for syngas production.

- Finally, investigating the scalability of these types of cells into stacks, and evaluating the change in degradation rate, would facilitate further understanding of the potential of these material sets on a larger scale.

APPENDIX ONE

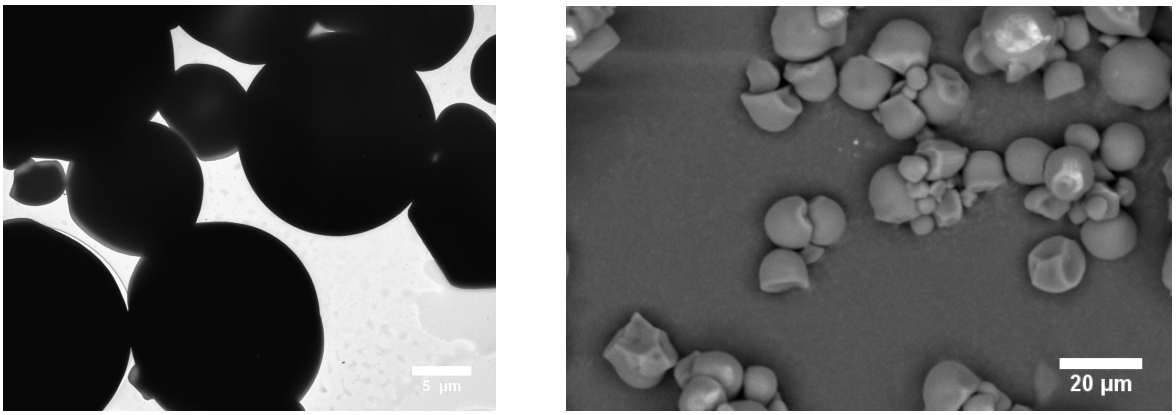
CHARACTERISATION OF STARTING MATERIALS

A.1 Microscopy



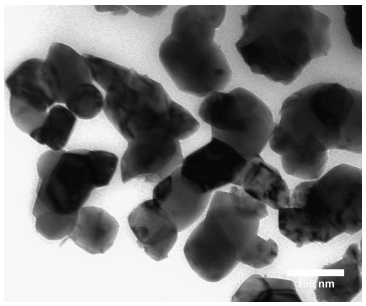
(a) NiO TEM micrograph **(b)** NiO TEM

Figure A.1: NiO TEM micrographs

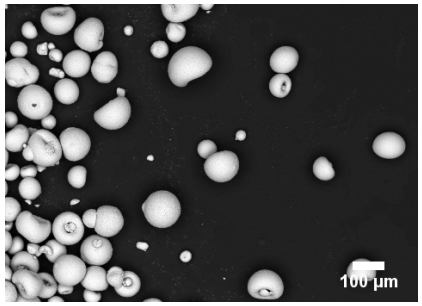


(a) Tapioca starch TEM micrograph **(b)** Tapioca starch SEM

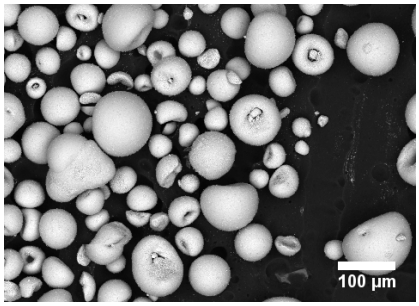
Figure A.2: Tapioca starch pore former imaged by (a) TEM, and (b) SEM.



(a) TEM image of as received 10Sc1CeSZ powder.

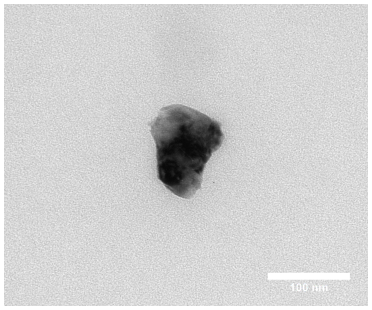


(b) SEM image of as received ScCeSZ powder.

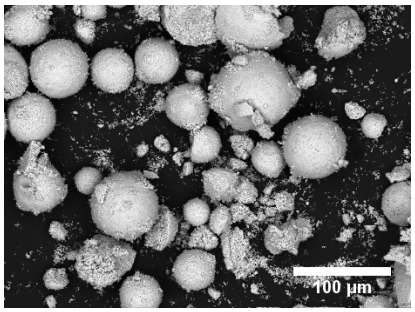


(c) SEM image of pre-calcined ScCeSZ powder.

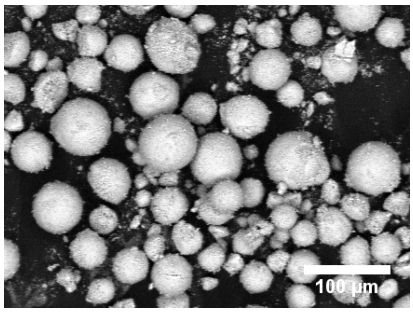
Figure A.3: TEM and SEM images of 10Sc1CeSZ powder from DAIICHI KIGENSO KAGAKU KOGYO CO., Ltd. (DKKK) showing (a) particles of size 0.1 µm, (b) agglomerates of the as received powder, and (c) agglomerates in the pre-calcined powder.



(a) TEM image of 8YSZ powder particle.

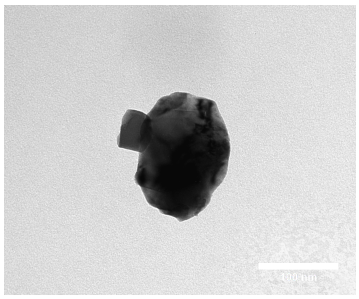


(b) SEM image of as received 8YSZ powder.

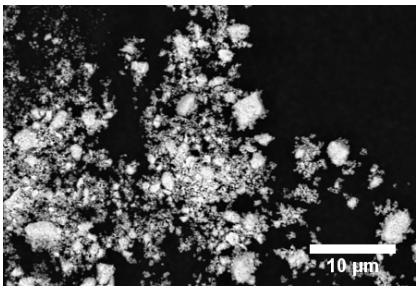


(c) SEM image of pre-calcined 8YSZ powder.

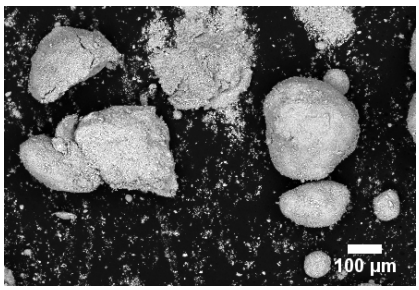
Figure A.4: TEM and SEM images of 8YSZ powder from Tosoh Ltd. showing (a) single 0.1 µm particle, and (b) agglomerates of the powder as received, and (c) agglomerates of the calcined powder.



(a) TEM image of 10GDC powder particle.



(b) SEM image of as received 10GDC powder.

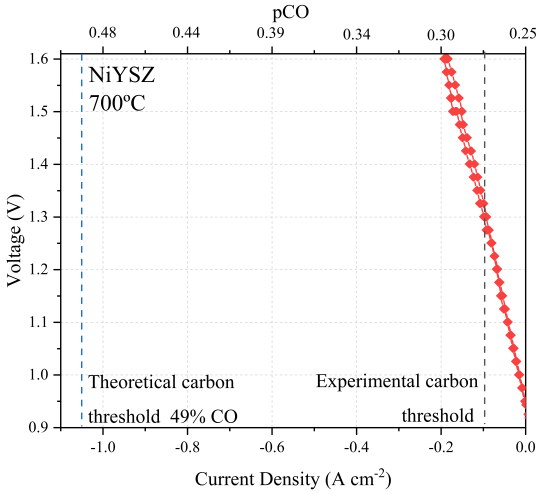


(c) SEM image of as received 10GDC powder showing agglomerates.

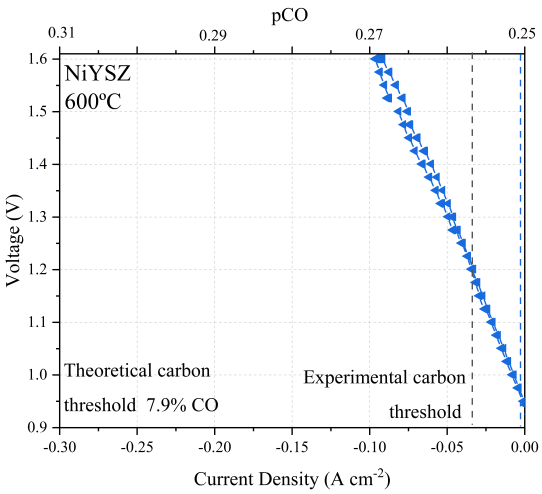
Figure A.5: TEM and SEM images of 10GDC powder from Fuel Cell MaterialsLtd. showing (a) single 0.15 µm particle, (b) and (c) agglomerates of the powder.

APPENDIX TWO

CARBON DEPOSITION THRESHOLD GRAPHS

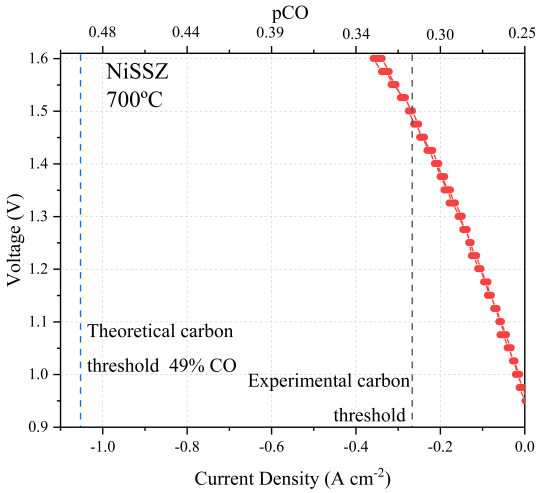


(a) Polarisation curve showing experimental and theoretical carbon deposition threshold for 700ºC.

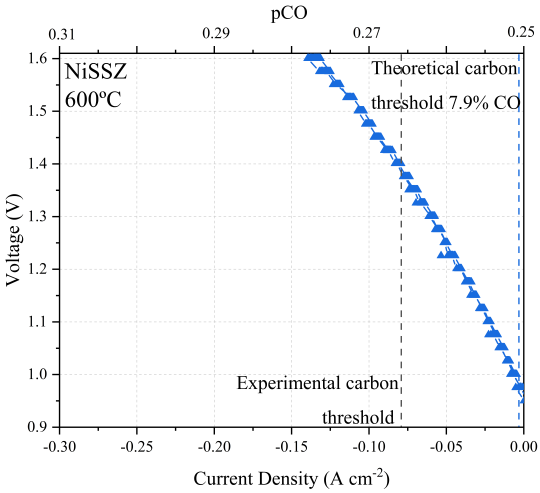


(b) Polarisation curve showing experimental and theoretical carbon deposition threshold for 600ºC.

Figure B.1: Polarisation curves at (a) 700ºC and (b) 600ºC showing experimental (grey) and theoretical (blue) carbon deposition thresholds as a vertical dashed line for NiYSZ cells.



(a) Polarisation curve showing experimental and theoretical carbon deposition threshold for 700ºC.



(b) Polarisation curve showing experimental and theoretical carbon deposition threshold for 600ºC.

Figure B.2: Polarisation curves at (a) 700ºC and (b) 600ºC showing experimental (grey) and theoretical (blue) carbon deposition thresholds as a vertical dashed line for NiSSZ cells.

APPENDIX THREE

AUTHOR CONTRIBUTION TO CHAPTER FOUR

Parts of Chapter Four: Cell Manufacturing, are based on the publication *Five-layer reverse tape casting of IT-SOFC* [222]. Author contributions to this paper that are mentioned in this thesis are outlined here.

A. L. Snowdon conceived the idea of a composite layer, wrote the paper, collected data including, thermal expansion coefficient of each material, SEM images, electrochemical polarisation curves and impedance plots. A. L. Snowdon and Z.Jiang both manufactured cells of differing layer thickness, imaged them using SEM. Z. Jiang carried out analysis of the SEM images including measurements and editing using ImageJ, and conceived the idea of the spin-coated cells. All authors provided critical feedback and helped shape the research, analysis and manuscript. Any other data that is present in the chapter that has not been mentioned in this annex, does not appear in the publication and is new collected data for this thesis.

Bibliography

[1] J. G. J. Olivier and J. A. H. W. Peters. *Trends in Global CO2 and Total Greenhouse Gas Emissions 2019 Report*. Tech. rep. The Hague: PBL Netherlands Environmental Assessment Agency, 2020.

[2] C. o. C. Change. "Reducing UK Emissions - 2018 Progress Report to Parliament" (2018).

[3] B. Steele, A. Atkinson, J. A. Kilner, N. P. Brandon, and R. A. Rudkin. *Fuel Cells, U.S. Patent US6794075B2*. 2001.

[4] R. Markillie. *UK Government's £23m funding for hydrogen vehicles and infrastructure*. URL: https://www.itm-power.com/news/launch-of-first-london-hyfive-hydrogen-refuelling-station (visited on 04/24/2019).

[5] International Rnewable Energy Agency. *Renewable Power Generation Costs in 2020*. 2020. URL: https://www.irena.org/-/media/Files/IRENA/Agency/Publication/2018/Jan/IRENA%7B%5C_%7D2017%7B%5C_%7DPower%7B%5C_%7DCosts%7B%5C_%7D2018.pdf.

[6] H. Corporation. "Hydrogenics wins P2G contract in Germany, electrolyser deal in UK". *Fuel Cells Bull.* (2017), 10–11.

[7] H. Corporation. "German wind site with 1 MW Hydrogenics P2G energy storage". *Fuel Cells Bull.* (2013), 8.

[8] Hydrogen. "ITM Power delivers Power-to-Gas unit to Thüga Frankfurt plant". *Fuel Cells Bull.* (2013), 8.

[9] F.C.H. *Development of Business Cases for Fuel Cells and Hydrogen Applications for Regions and Cities- Hydrogen injection into the Natural Gas Grid.* Tech. rep. Brussels, 2017, 1–18.

[10] HyDeploy. *UK's first grid-injected hydrogen pilot gets underway - HyDeploy*. URL: https://hydeploy.co.uk/about/news/uks-first-grid-injected-hydrogen-pilot-gets-underway/ (visited on 01/07/2020).

[11] P. Breeze. *Fuel Cells*. London: Elsevier Ltd., 2017, 4.

[12] F. C. T. Office. "Fuel Cell Fact Sheet" (2015).

[13] M. M. Hussain, X. Li, and I. Dincer. “A general electrolyte-electrode-assembly model for the performance characteristics of planar anode-supported solid oxide fuel cells”. *J. Power Sources* 189 (2009), 916–928.

[14] H. Kim, J.-W. Lee, S.-B. Lee, T.-H. Lim, S.-J. Park, R.-H. Song, and D.-R. Shin. “Evaluation of Micro-Tubular SOFC: Cell Performance with respect to Current Collecting Method”. *Trans. Korean Hydrog. New Energy Soc.* 23 (2012), 43–48.

[15] F. Zhao, T. J. Armstrong, and A. V. Virkar. “Measurement of O_2-N_2 Effective Diffusivity in Porous Media at High Temperatures Using an Electrochemical Cell”. *J. Electrochem. Soc.* 150 (2003), A249.

[16] K. Nath and D. Das. “Production and storage of hydrogen: Present scenario and future perspective”. *J. Sci. Ind. Res.* 66 (2007), 701–709.

[17] C.-J. Winter and J. Nitsch. *Hydrogen as an energy carrier: technologies, systems, economy*. Ed. by J. Nitsch. Berlin: Springer-Verlag, 1988.

[18] Helmeth Project. *High temperature electrolysis cell (SOEC)*. URL: http://www.helmeth.eu / index . php / technologies / high - temperature - electrolysis - cell - soec (visited on 10/01/2021).

[19] X. Sun, B. R. Sudireddy, X. Tong, M. Chen, K. Brodersen, and A. Hauch. “Optimization and Durability of Reversible Solid Oxide Cells”. *ECS Trans.* 91 (2019), 2631–2639.

[20] J. Mermelstein and O. Posdziech. “Development and Demonstration of a Novel Reversible SOFC System for Utility and Micro Grid Energy Storage”. *Fuel Cells* 17 (2017), 562–570.

[21] H. Europe. *Project REFLEX*. Tech. rep. 2018, 2–3.

[22] C. Bin, Y. S. Hajimolana, V. Venkataraman, M. Ni, and P. Aravind. “Integration of Reversible Solid Oxide Cells with methane synthesis (ReSOC-MS) in grid stabilization”. *Energy Procedia* 158 (2019), 2077–2084.

[23] S. H. Jensen, C. Graves, M. Mogensen, C. Wendel, R. Braun, G. Hughes, Z. Gao, and S. A. Barnett. “Large-scale electricity storage utilizing reversible solid oxide cells combined with underground storage of CO_2 and CH_4”. *Energy Environ. Sci. Energy Environ. Sci* 8 (2015), 2471–2479.

[24] S. D. Ebbesen, X. Sun, and M. B. Mogensen. “Understanding the processes governing performance and durability of solid oxide electrolysis cells”. *Faraday Discuss.* 182 (2015), 393–422.

[25] Z. Liu, H. Yang, R. Kutz, and R. I. Masel. “CO_2 electrolysis to CO and O_2 at high selectivity, stability and efficiency using sustainion membranes”. *J. Electrochem. Soc.* 165 (2018), J3371–J3377.

[26] K. Xie, Y. Zhang, G. Meng, and J. T. S. Irvine. "Direct synthesis of methane from CO_2/H_2O in an oxygen conducting solid oxide electrolyser." *Energy Environ. Sci.* 4 (2011), 2218.

[27] C. Yang, J. Li, J. Newkirk, V. Baish, R. Hu, Y. Chen, and F. Chen. "Co-electrolysis of H_2O and CO_2 in a solid oxide electrolysis cell with hierarchically structured porous electrodes". *J. Mater. Chem. A* 3 (2015), 15913–15919.

[28] S. D. Ebbesen and M. Mogensen. "Electrolysis of carbon dioxide in Solid Oxide Electrolysis Cells". *J. Power Sources* 193 (2009), 349–358.

[29] C. Graves, S. D. Ebbesen, and M. Mogensen. "Co-electrolysis of CO_2 and H_2O in solid oxide cells: Performance and durability". *Solid State Ionics* 192 (2011), 398–403.

[30] M. Chen, J. V. T. Høgh, J. U. Nielsen, J. J. Bentzen, S. D. Ebbesen, and P. V. Hendriksen. "High temperature co-electrolysis of steam and CO_2 in an SOC stack: Performance and durability". *Fuel Cells* 13 (2013), 638–645.

[31] S. Diethelm, J. V. Herle, D. Montinaro, and O. Bucheli. "Electrolysis and Co-electrolysis performance of SOE short stacks". *Fuel Cells* 13 (2013), 631–637.

[32] N. H. Menzler, W. Schafbauer, R. Mücke, R. Kauert, and O. Büchler. "Advanced Manufacturing Technology for Solid Oxide Fuel Cells". *Adv. Solid Oxide Fuel Cells VII*. Ed. by N. P. Bansal, P. Singh, S. Widjaja, and D. Singh. John Wiley & Sons, Ltd, 2011, 147–160.

[33] G. N. Howatt, R. G. Breckenridge, and J. M. Brownlow. "Fabrication of Thin Film Ceramic Sheets for Capacitors". *J. Am. Ceram. Soc.* 30 (1947), 237–242.

[34] E. R. Twiname. "Tape Casting and Lamination". *Encycl. Mater. Tech. Ceram. Glas.* (2021), 189–194.

[35] R. E. Mistler and E. R. Twiname. *Tape Casting: Theory and Practice*. Wiley, 2000, 298.

[36] J. Zhou, Q. Liu, Q. Sun, and S. H. Chan. "A Low Cost Large-Area Solid Oxide Cells Fabrication Technology based on Aqueous Co-Tape Casting and Co-Sintering". *Fuel Cells* 14 (2014), 667–670.

[37] W. Schafbauer, N. H. Menzler, and H. P. Buchkremer. "Tape Casting of Anode Supports for Solid Oxide Fuel Cells at Forschungszentrum Jülich". *Int. J. Appl. Ceram. Technol.* 11 (2014), 125–135.

[38] W. S. Jang, S. H. Hyun, and S. G. Kim. "Preparation of YSZ/YDC and YSZ/GDC composite electrolytes by the tape casting and sol-gel dip-drawing coating method for low-temperature SOFC". *J. Mater. Chem. A* 37 (2002), 2535–2541.

[39] C. Goulart and D. de Souza. "Critical analysis of aqueous tape casting, sintering, and characterization of planar Yttria-Stabilized Zirconia electrolytes for SOFC". *Int. J. Appl. Ceram. Technol.* 14 (2017), 413–423.

[40] M. R. Somalu, V. Yufit, D. Cumming, E. Lorente, and N. P. Brandon. “Fabrication and characterization of Ni/ScSZ cermet anodes for IT-SOFCs”. *Int. J. Hydrogen Energy* 36 (2011), 5557–5566.

[41] M. P. Albano and L. B. Garrido. “Aqueous tape casting of yttria stabilized zirconia”. *Mater. Sci. Eng. A* 420 (2006), 171–178.

[42] A. Kristoffersson, E. Roncari, and C. Galassi. “Comparison of different binders for water-based tape casting of alumina”. *J. Eur. Ceram. Soc.* 18 (1998), 2123–2131.

[43] N. Arifin, T. Button, and R. Steinberger-Wilckens. “Carbon-Tolerant Ni/ScCeSZ Via Aqueous Tape Casting for IT-SOFCs”. *ECS Transactions* 78 (2017), 1417–1426.

[44] M. Boaro, J. M. Vohs, and R. J. Gorte. “Synthesis of highly porous yttria-stabilized zirconia by tape-casting methods”. *J. Am. Ceram. Soc.* 86 (2003), 395–400.

[45] A. Sarikaya and F. Dogan. “Effect of various pore formers on the microstructural development of tape-cast porous ceramics”. *Ceram. Int.* 39 (2013), 403–413.

[46] D. H. Kim, K. Y. Lim, U. Paik, and Y. G. Jung. “Effects of chemical structure and molecular weight of plasticizer on physical properties of green tape in $BaTiO_3$/PVB system”. *J. Eur. Ceram. Soc.* 24 (2004), 733–738.

[47] Z. Wang, J. Qian, J. Cao, S. Wang, and T. Wen. “A study of multilayer tape casting method for anode-supported planar type solid oxide fuel cells (SOFCs)”. *J. Alloys Compd.* 437 (2007), 264–268.

[48] C. Jin, Y. Mao, D. W. Rooney, N. Zhang, and K. Sun. “Fabrication and characterization of SSZ tape cast electrolyte-supported solid oxide fuel cells”. *Ceram. Int.* 42 (2016), 5523–5529.

[49] L. Wang, G. Tang, and Z.-K. Xu. “Comparison of Water-Based and Solvent-Based Tape Casting for Preparing Multilayer ZnO Varistors”. *J. Am. Ceram. Soc.* 91 (2008), 3742–3745.

[50] D. Hotza and P. Greil. “Review: aqueous tape casting of ceramic powders”. *Mater. Sci. Eng. A* 202 (1995), 206–217.

[51] P. Nahass, W. Rhine, R. Pober, H. Bowen, and W. Robbins. “A comparison of aqueous and non-aqueous slurries for tape casting”. *Ceram. Trans.* 15 (1990), 355–364.

[52] R. K. Nishihora, P. L. Rachadel, M. G. N. Quadri, and D. Hotza. “Manufacturing porous ceramic materials by tape casting—A review”. *J. Eur. Ceram. Soc.* 38 (2018), 988–1001.

[53] J. Zhou, Q. Liu, L. Zhang, Z. Pan, and S. H. Chan. “Influence of pore former on electrochemical performance of fuel-electrode supported SOFCs manufactured by aqueous-based tape-casting”. *Energy* 115 (2016), 149–154.

[54] A. Sanson, P. Pinasco, and E. Roncari. “Influence of pore formers on slurry composition and microstructure of tape cast supporting anodes for SOFCs”. *J. Eur. Ceram. Soc.* 28 (2008), 1221–1226.

[55] M. A. Hanifi A. R.and Laguna-Bercero, N. K. Sandhu, T. H. Etsell, and P. Sarkar. “Tailoring the Microstructure of a Solid Oxide Fuel Cell Anode Support by Calcination and Milling of YSZ”. *Sci. Rep.* 6 (2016), 27359.

[56] K. Lee S.and Lee, Y. hoon Jang, and J. Bae. “Fabrication of solid oxide fuel cells (SOFCs) by solvent-controlled co-tape casting technique”. *Int. J. Hydrogen Energy* 42 (2017), 1648–1660.

[57] N. A. Arifin. “Developing Carbon Tolerant Ni/ScCeSZ cells via Aqueous Tape Casting for Direct Biogas fed Solid Oxide Fuel Cells (SOFC)”. PhD thesis. University of Birmingham, 2018.

[58] J. Watton. “Performance and degradation of solid oxide cells for steam electrolysis by”. PhD thesis. University of Birmingham, 2016.

[59] B. Yildiz. “Reversible solid oxide electrolytic cells for large-scale energy storage: challenges and opportunities”. *Funct. Mater. Sustain. Energy Appl.* Ed. by J. A. Kilner, S. J. Skinner, S. J. C. Irvine, and P. P. Edwards. Woodhead Publishing, 2012. Chap. 6, 149–179e.

[60] C. Graves, S. D. Ebbesen, S. H. Jensen, S. B. Simonsen, and M. B. Mogensen. “Eliminating degradation in solid oxide electrochemical cells by reversible operation”. *Nat. Mater.* 14 (2014), 239–244.

[61] S. Zha, Z. Cheng, and M. Liu. “Sulfur Poisoning and Regeneration of Ni-Based Anodes in Solid Oxide Fuel Cells”. *J. Electrochem. Soc.* 154 (2007), B201.

[62] K. Sasaki, K. Susuki, A. Iyoshi, M. Uchimura, N. Imamura, H. Kusaba, Y. Teraoka, H. Fuchino, K. Tsujimoto, Y. Uchida, and N. Jingo. “H_2S Poisoning of Solid Oxide Fuel Cells”. *J. Electrochem. Soc.* 153 (2006), A2023.

[63] Y. Matsuzaki and I. Yasuda. “Poisoning effect of sulfur-containing impurity gas on a SOFC anode: Part I. Dependence on temperature, time, and impurity concentration”. *Solid State Ionics* 132 (2000), 261–269.

[64] Z. Cheng and M. Liu. “Characterization of sulfur poisoning of Ni-YSZ anodes for solid oxide fuel cells using in situ Raman microspectroscopy”. *Solid State Ionics* 178 (2007), 925–935.

[65] Z. Cheng, S. Zha, and M. Liu. “Influence of cell voltage and current on sulfur poisoning behavior of solid oxide fuel cells”. *J. Power Sources* 172 (2007), 688–693.

[66] S. Ebbesen, C. R. Graves, A. Hauch, S. H. Jensen, and M. B. Mogensen. "Poisoning of Solid Oxide Electrolysis Cells by Impurities". *J. Electrochem. Soc.* 157 (2010), 1419–1429.

[67] T. L. Skafte, P. Blennow, J. Hjelm, and C. Graves. "Carbon deposition and sulfur poisoning during CO_2 electrolysis in nickel-based solid oxide cell electrodes". *J. Power Sources* 373 (2018), 54–60.

[68] A. Hagen, J. F. Rasmussen, and K. Thydén. "Durability of solid oxide fuel cells using sulfur containing fuels". *J. Power Sources* 196 (2011), 7271–7276.

[69] L. Yang, Z. Cheng, M. Liu, and L. Wilson. "New insights into sulfur poisoning behavior of Ni-YSZ anode from long-term operation of anode-supported SOFCs". *Energy Environ. Sci.* 3 (2010), 1804–1809.

[70] A. Hauch, S. D. Ebbesen, S. H. Jensen, and M. Mogensen. "Solid Oxide Electrolysis Cells: Microstructure and Degradation of the Ni/Yttria-Stabilized Zirconia Electrode". *J. Electrochem. Soc.* 155 (2008), B1184.

[71] J. M. Porras-Vazquez and P. R. Slater. "Synthesis and Characterization of Oxyanion-Doped Cobalt Containing Perovskites". *Fuel Cells* 12 (2012), 1056–1063.

[72] K. Hilpert, D. Das, M. Miller, D. H. Peck, and R. Weiß. "Chromium Vapor Species over Solid Oxide Fuel Cell Interconnect Materials and Their Potential for Degradation Processes". *J. Electrochem. Soc.* 143 (1996), 3642–3647.

[73] S. R. Akanda, M. E. Walter, N. J. Kidner, and M. M. Seabaugh. "Mechanical characterization of oxide coating-interconnect interfaces for solid oxide fuel cells". *J. Power Sources* 210 (2012), 254–262.

[74] M. S. Sohal, J. E. O'brien, C. M. Stoots, V. I. Sharma, B. Yildiz, and A. Virkar. "Degradation issues in solid oxide cells during high temperature electrolysis". *Proc. ASME 2010 Eight Int. Fuel Cell Sci. Eng. Technol. Conf.* 2010.

[75] M. B. Mogensen, M. Chen, H. L. Frandsen, C. Graves, J. B. Hansen, K. V. Hansen, A. Hauch, T. Jacobsen, S. H. Jensen, T. L. Skafte, and X. Sun. "Reversible solid-oxide cells for clean and sustainable energy". *Clean Energy* 3 (2019), 175–201.

[76] A. V. Virkar. "Mechanism of oxygen electrode delamination in solid oxide electrolyzer cells". *Int. J. Hydrogen Energy* 37 (2010), 9527–9543.

[77] G. A. Hughes, K. Yakal-Kremski, and S. A. Barnett. "Life testing of LSM–YSZ composite electrodes under reversing-current operation". *Phys. Chem. Chem. Phys.* 15 (2013), 17257.

[78] J. Guan, N. Minh, B. Ramamurthi, J. Ruud, J.-K. Hong, P. Riley, and D. Weng. *High Performance Flexible Reversible Solid Oxide Fuel Cell*. Tech. rep. DoE, 2007.

[79] M. A. Laguna-Bercero, R. Campana, A. Larrea, J. A. Kilner, and V. M. Orera. "Performance and aging of microtubular YSZ-based solid oxide regenerative fuel cells". *Fuel Cells* 11 (2011), 116–123.

[80] W. Wang, Y. Huang, S. Jung, J. M. Vohs, and R. J. Gorte. "A Comparison of LSM, LSF, and LSCo for Solid Oxide Electrolyzer Anodes". *J. Electrochem. Soc.* 153 (2006), A2066.

[81] K. M. Papazisi, D. Tsiplakides, and S. Balomenou. "Carbon Tolerant Fuel Electrodes for Reversible SOFC Operating on Carbon Dioxide". *E3S Web of Conferences* 16 (2017).

[82] V. Vibhu, S. Yildiz, S. R. Foit, K. Schiemann, I. C. Vinke, R.-A. Eichel, and L. de Haart. "LSC Infiltrated LSCF Oxygen Electrode for High Temperature Steam Electrolysis". *ECS Trans.* 78 (2017), 3283–3295.

[83] A. Brisse, J. Schefold, and M. Zahid. "High temperature water electrolysis in solid oxide cells". *Int. J. Hydrogen Energy* 33 (2008), 5375–5382.

[84] J. Schefold, A. Brisse, and M. Zahid. "Long Term Testing of Solid Oxide Fuel Cell Stacks with Yttria Stabilized Zirconia Electrolyte in the H_2O Electrolysis Mode". *ECS Trans.* ECS, 2010, 357–367.

[85] J. Schefold, A. Brisse, and F. Tietz. "Nine Thousand Hours of Operation of a Solid Oxide Cell in Steam Electrolysis Mode". *J. Electrochem. Soc.* 159 (2012), 137–144.

[86] F. Tietz, D. Sebold, A. Brisse, and J. Schefold. "Degradation phenomena in a solid oxide electrolysis cell after 9000 h of operation". *J. Power Sources* 223 (2013), 129–135.

[87] P. Hjalmarsson, X. Sun, Y. L. Liu, and M. Chen. "Influence of the oxygen electrode and inter-diffusion barrier on the degradation of solid oxide electrolysis cells". *J. Power Sources* 223 (2013), 349–357.

[88] P. Kim-Lohsoontorn, N. Laosiripojana, and J. Bae. "Performance of solid oxide electrolysis cell having bi-layered electrolyte during steam electrolysis and carbon dioxide electrolysis". *Curr. Appl. Phys.* 11 (2011), S223–S228.

[89] K. Chen and S. P. Jiang. "Failure mechanism of (La,Sr)MnO_3 oxygen electrodes of solid oxide electrolysis cells". *Int. J. Hydrogen Energy* 36 (2011), 10541–10549.

[90] N. Mahato, A. Banerjee, A. Gupta, S. Omar, and K. Balani. "Progress in material selection for solid oxide fuel cell technology: A review". *Prog. Mater. Sci.* 72 (2015), 141–337.

[91] S. J. Kim, S. W. Kim, Y. M. Park, K. J. Kim, and G. M. Choi. "Effect of Gd-doped ceria interlayer on the stability of solid oxide electrolysis cell". *Solid State Ionics* 295 (2016), 25–31.

[92] T. Klemensø, C. Chung, P. H. Larsen, and M. Mogensen. "The Mechanism Behind Redox Instability of Anodes in High-Temperature SOFCs". *J. Electrochem. Soc.* 152 (2005), A2186–A2192.

[93] D. Sarantaridis and A. Atkinson. "Redox Cycling of Ni-Based Solid Oxide Fuel Cell Anodes: A Review". *Fuel Cells* 7 (2007), 246–258.

[94] B. Song, E. Ruiz-Trejo, A. Bertei, and N. P. Brandon. "Quantification of the degradation of Ni-YSZ anodes upon redox cycling". *J. Power Sources* 374 (2018), 61–68.

[95] D. Waldbillig, A. Wood, and D. G. Ivey. "Thermal analysis of the cyclic reduction and oxidation behaviour of SOFC anodes". *Solid State Ionics* 176 (2005), 847–859.

[96] L. Grahl-Madsen, P. H. Larsen, N. Bonanos, J. Engell, and S. Linderoth. "Mechanical strength and electrical conductivity of Ni-YSZ cermets fabricated by viscous processing". *J. Mater. Sci.* 41 (2006), 1097–1107.

[97] R. M. German. "Coarsening in Sintering: Grain Shape Distribution, Grain Size Distribution, and Grain Growth Kinetics in Solid-Pore Systems". *Crit. Rev. Solid State Mater. Sci.* 35 (2010), 263–305.

[98] M. S. Khan, S. B. Lee, R. H. Song, J. W. Lee, T. H. Lim, and S. J. Park. "Fundamental mechanisms involved in the degradation of nickel–yttria stabilized zirconia (Ni–YSZ) anode during solid oxide fuel cells operation: A review". *Ceram. Int.* 42 (2016), 35–48.

[99] J. Alemán, A. V. Chadwick, J. He, M. Hess, K. Horie, R. G. Jones, P. Kratochvíl, I. Meisel, I. Mita, G. Moad, S. Penczek, and R. F. Stepto. "Definitions of terms relating to the structure and processing of sols, gels, networks, and inorganic-organic hybrid materials". *Pure Appl. Chem.* 79 (2007), 1801–1829.

[100] T. S. Li, W. G. Wang, H. Miao, T. Chen, and C. Xu. "Effect of reduction temperature on the electrochemical properties of a Ni/YSZ anode-supported solid oxide fuel cell". *J. Alloys Compd.* 495 (2010), 138–143.

[101] L. Holzer, B. Iwanschitz, T. Hocker, B. Münch, M. Prestat, D. Wiedenmann, U. Vogt, P. Holtappels, J. Sfeir, A. Mai, and T. Graule. "Microstructure degradation of cermet anodes for solid oxide fuel cells: Quantification of nickel grain growth in dry and in humid atmospheres". *J. Power Sources* 196 (2011), 1279–1294.

[102] A. Gubner, H. Landes, J. Metzger, H. Seeg, and R. Stübner. "Investigations into the Degradation of the Cermet Anode of a Solid Oxide Fuel Cell". *ECS Proc. Vol.* 40 (1997), 844–850.

[103] A. Hauch, K. Brodersen, M. Chen, and M. B. Mogensen. "Ni/YSZ electrodes structures optimized for increased electrolysis performance and durability". *Solid State Ionics* 293 (2016), 27–36.

[104] H. Sumi, K. Ukai, Y. Mizutani, H. Mori, C.-J. Wen, H. Takahashi, and O. Yamamoto. "Performance of nickel–scandia-stabilized zirconia cermet anodes for SOFCs in 3% H_2O–CH_4". *Solid State Ionics* 174 (2004), 151–156.

[105] K. Huang and J. B. Goodenough. *Solid Oxide Fuel Cell Technology*. Cambridge: Woodhead Publishing Limited, 2009.

[106] X. Li, M. Liu, S. Y. Lai, D. Ding, M. Gong, J. P. Lee, K. S. Blinn, Y. Bu, Z. Wang, L. A. Bottomley, F. M. Alamgir, and M. Liu. "In Situ Probing of the Mechanisms of Coking resistance on Catalyst-Modified Anodes for Solid Oxide Fuel Cells". *Chem. Mater.* 27 (2015), 822–828.

[107] M. B. Mogensen. "Materials for reversible solid oxide cells". *Curr. Opin. Electrochem.* 21 (2020), 265–273.

[108] K. Sasaki and Y. Teraoka. "Equilibria in Fuel Cell Gases". *J. Electrochem. Soc.* 150 (2003), 885–888.

[109] M. Liu, Y. M. Choi, L. Yang, K. Blinn, W. Qin, P. Liu, and M. Liu. "Direct octane fuel cells: A promising power for transportation". *Nano Energy* 1 (2012), 448–455.

[110] M. Liu, L. Yang, S. Wang, K. Blinn, M. Liu, Z. Liu, and Z. Cheng. "Enhanced sulfur and coking tolerance of a mixed ion conductor for SOFCs: $BaZr_{0.1}Ce_{0.7}y_{0.2-x}Yb_xO_{3-\delta}$". *Science* 326 (2009), 126–129.

[111] L. Yang, Y. Choi, W. Qin, H. Chen, K. Blinn, M. Liu, P. Liu, J. Bai, T. A. Tyson, and M. Liu. "Promotion of water-mediated carbon removal by nanostructured barium oxide/nickel interfaces in solid oxide fuel cells". *Nat. Commun.* 2 (2011), 1–9.

[112] N. M. Galea, D. Knapp, and T. Ziegler. "Density functional theory studies of methane dissociation on anode catalysts in solid-oxide fuel cells: Suggestions for coke reduction". *J. Catal.* 247 (2007), 20–33.

[113] J. Guo, C. Xie, K. Lee, N. Guo, J. T. Miller, M. J. Janik, and C. Song. "Improving the carbon resistance of Ni-based steam reforming catalyst by alloying with Rh: A computational study coupled with reforming experiments and EXAFS characterization". *ACS Catal.* 1 (2011), 574–582.

[114] E. Nikolla, J. W. Schwank, and S. Linic. "Hydrocarbon steam reforming on Ni alloys at solid oxide fuel cell operating conditions". *Catal. Today* 136 (2008), 243–248.

[115] J. Liu and S. A. Barnett. "Operation of anode-supported solid oxide fuel cells on methane and natural gas". *Solid State Ionics* 158 (2003), 11–16.

[116] S. Mcintosh and R. J. Gorte. "Direct Hydrocarbon Solid Oxide Fuel Cells". *Chem. Rev.* 104 (2004), 4845–4846.

[117] D. La Rosa, A. Sin, M. L. Faro, G. Monforte, V. Antonucci, and A. S. Aricò. “Mitigation of carbon deposits formation in intermediate temperature solid oxide fuel cells fed with dry methane by anode doping with barium”. *J. Power Sources* 193 (2009), 160–164.

[118] H. Hongpeng, R. J. Gorte, and J. M. Vohs. “Highly Sulfur Tolerant Cu-Ceria Anodes for SOFCs”. *Electrochem. Solid-State Lett.* 8 (2005), A279–A280.

[119] H. Sumi, P. Puengjinda, H. Muroyama, T. Matsui, and K. Eguchi. “Effects of crystal structure of yttria- and scandia-stabilized zirconia in nickel-based SOFC anodes on carbon deposition and oxidation behavior”. *J. Power Sources* 196 (2011), 6048–6054.

[120] A. Gunji, C. Wen, J. Otomo, T. Kobayashi, K. Ukai, Y. Mizutani, and H. Takahashi. “Carbon deposition behaviour on Ni-ScSZ anodes for internal reforming solid oxide fuel cells”. *J. Power Sources* 131 (2004), 285–288.

[121] D. A. Agarkov, M. A. Borik, S. I. Bredikhin, I. N. Burmistrov, G. M. Eliseeva, V. A. Kolotygin, A. V. Kulebyakin, I. E. Kuritsyna, E. E. Lomonova, F. O. Milovich, V. A. Myzina, P. A. Ryabochkina, N. Y. Tabachkova, and T. V. Volkova. “Structure and transport properties of zirconia crystals co-doped by scandia, ceria and yttria”. *J. Mater.* 5 (2019), 273–279.

[122] Y. Arachi, T. Asai, O. Yamamoto, Y. Takeda, N. Imanishi, K. Kawate, and C. Tamakoshi. “Electrical Conductivity of ZrO_2 Sc_2O_3 Doped with HfO_2, CeO_2, and Ga_2O_3”. *J. Electrochem. Soc* 148 (2001), A520–A523.

[123] M. A. Laguna-Bercero, S. J. Skinner, and J. A. Kilner. “Performance of solid oxide electrolysis cells based on scandia stabilised zirconia”. *J. Power Sources* 192 (2009), 126–131.

[124] Y. Tao, D. Ebbesen, and M. B. Mogensen. “Carbon Deposition in Solid Oxide Cells during Co-Electrolysis of H_2O and CO_2”. *J. Electrochem. Soc.* 161 (2014), F337–F343.

[125] M. B. Pomfret, J. Marda, G. S. Jackson, B. W. Eichhorn, A. M. Dean, and R. A. Walker. “Hydrocarbon fuels in solid oxide fuel cells: In situ Raman studies of graphite formation and oxidation”. *J. Phys. Chem. C* 112 (2008), 5232–5240.

[126] Z.-Y. Chen, L.-J. Wang, X.-J. Du, Z.-H. Sun, F.-S. Li, and K.-C. Chou. “Carbon deposition in porous nickel/yttria-stabilized zirconia anode under methane atmosphere”. *Int. J. Miner. Metall. Mater.* 26 (2019).

[127] M. Yoshinaga, H. Kishimoto, K. Yamaji, Y. P. Xiong, M. E. Brito, T. Horita, and H. Yokokawa. “Deposited carbon distributions on nickel film/oxide substrate systems”. *Solid State Ionics*. Vol. 192. Elsevier, 2011, 571–575.

[128] Y. Zheng, J. Wang, B. Yu, W. Zhang, J. Chen, J. Qiao, and J. Zhang. "A review of high temperature co-electrolysis of H_2O and CO_2 to produce sustainable fuels using solid oxide electrolysis cells (SOECs): advanced materials and technology". *Chem. Soc. Rev.* 46 (2017), 1427–1463.

[129] N. Q. Minh and M. B. Mogensen. "Reversible Solid Oxide Fuel Cell Technology for Green Fuel and Power Production". *Electrochem. Soc. Interface* 22 (2013), 55–62.

[130] R. L. Ash, W. L. Dowler, and G. Varsi. "Feasibility of rocket propellant production on Mars". *Acta Astronaut.* 5 (1978), 705–724.

[131] NASA. *MOXIE for Scientists - NASA Mars*. 2020. URL: https://mars.nasa.gov/mars2020/spacecraft/instruments/moxie/for-scientists/ (visited on 07/22/2021).

[132] J. E. O'Brien, M. G. McKellar, C. M. Stoots, J. S. Herring, and G. L. Hawkes. "Parametric study of large-scale production of syngas via high-temperature co-electrolysis". *Int. J. Hydrogen Energy* 34 (2009), 4216–4226.

[133] Q. Fu, C. Mabilat, M. Zahid, A. Brisse, and L. Gautier. "Syngas production via high-temperature steam/CO_2 co-electrolysis: an economic assessment". *Energy Environ. Sci.* 3 (2010), 1382–1397.

[134] S. D. Ebbesen, R. Knibbe, and M. Mogensen. "Co-Electrolysis of Steam and Carbon Dioxide in Solid Oxide Cells". *J. Electrochem. Soc.* 159 (2012), F482–F489.

[135] Z. Zhan, W. Kobsiriphat, J. R. Wilson, M. Pillai, I. Kim, and S. A. Barnett. "Syngas Production By Co-electrolysis of CO_2 /H_2O: The Basis for a Renewable Energy Cycle". *Energy & Fuels* 23 (2009), 3089–3096.

[136] J. Dragsbaek Duhn, A. Degn Jensen, S. Wedel, and C. Wix. "Modeling of Gas Diffusion in Ni/YSZ Electrodes in CO_2 and Co-electrolysis". *Fuel Cells* 17 (2017), 442–456.

[137] L. Wang, Y. Zhang, M. Pérez-Fortes, P. Aubin, T. E. Lin, Y. Yang, F. Maréchal, and J. Van herle. "Reversible solid-oxide cell stack based power-to-x-to-power systems: Comparison of thermodynamic performance". *Appl. Energy* 275 (2020), 115330.

[138] D. M. Santos, C. A. Sequeira, and J. L. Figueiredo. "Hydrogen production by alkaline water electrolysis". *Quim. Nova* 36 (2013), 1176–1193.

[139] M. Thema, F. Bauer, and M. Sterner. "Power-to-Gas: Electrolysis and methanation status review". *Renew. Sustain. Energy Rev.* 112 (2019), 775–787.

[140] C. Wulf, J. Linßen, and P. Zapp. *Hydrogen Supply Chain: Design, Deployment and Operation*. Ed. by C. Azzaro-Pantel. London: Elsevier Ltd., 2018.

[141] A. Hauch, R. Küngas, P. Blennow, A. B. Hansen, J. B. Hansen, B. V. Mathiesen, and M. B. Mogensen. "Recent advances in solid oxide cell technology for electrolysis". *Science* 370 (2020).

[142] T. I. R. E. Agency. *Green hydrogen cost reduction scaling up electrolysers to meet the 1.5°c climate goal*. Tech. rep. 2020.

[143] M. Belimov, D. Metzger, and P. Pfeifer. "On the temperature control in a microstructured packed bed reactor for methanation of CO/CO_2 mixtures". *AIChE J.* 63 (2017), 120–129.

[144] C. von Olshausen. *Technologies for Sustainability and Climate Protection - Chemical Processes and Use of CO2*. Tech. rep. 2017, 133–141.

[145] *BALANCE project*. URL: https://www.balance-project.org/ (visited on 06/29/2020).

[146] *GrInHy 2.0: Green Industrial Hydrogen*. URL: https://www.green-industrial-hydrogen.com/ (visited on 06/24/2020).

[147] J. B. Hansen. "Biogas Upgrading in a 50 Kilowatt Solid Oxide Cells Based Demonstration Plant - Design and Operational Experiences Including Strategies to Counteract Degradation". *ECS Meet. Abstr.* MA2017-01 (2017), 1520.

[148] Daimler, Linde, and TOTAL. *New TOTAL hydrogen filling station in Karlsruhe unites mobility and renewable energy*. Tech. rep. 2017.

[149] F. Baldi, L. Wang, M. Pérez-Fortes, and F. Maréchal. "A cogeneration system based on solid oxide and proton exchange membrane fuel cells with hybrid storage for off-grid applications". *Front. Energy Res.* 6 (2019), 1–18.

[150] Sunfire GmbH. *Breakthrough for Power-to-X: Sunfire puts first co-electrolysis into operation and starts scaling*. Tech. rep. 2019.

[151] DTU. *Synfuel*. 2019. URL: https://www.synfuel.dk/ (visited on 06/23/2020).

[152] *NewSOC*. URL: https://www.newsoc.eu/ (visited on 06/27/2020).

[153] "Total, Sunfire partner on hydrogen tech for methanol production". *Fuel Cells Bull.* 2019 (2019), 12.

[154] "MultiPLHY project for green hydrogen at refinery in Rotterdam". *Fuel Cells Bull.* 2020 (2020), 10.

[155] A. O. Isenberg. "Energy conversion via solid oxide electrolyte electrochemical cells at high temperatures". *Solid State Ionics* 3-4 (1981), 431–437.

[156] E. Erdle, W. Dönitz, R. Schamm, and A. Koch. "Reversibility and polarization behaviour of high temperature solid oxide electrochemical cells". *Int. J. Hydrogen Energy* 17 (1992), 817–819.

[157] W. Dönitz, G. Dietrich, E. Erdle, and R. Streicher. "Electrochemical high temperature technology for hydrogen production or direct electricity generation". *Int. J. Hydrogen Energy* 13 (1988), 283–287.

[158] W. Dönitz and E. Erdle. “High-temperature electrolysis of water vapor-status of development and perspectives for application”. *Int. J. Hydrogen Energy* 10 (1985), 291–295.

[159] M. S. Hsu and M. I. of Technology. *Solid oxide electrochemical energy converter*. 1984.

[160] D. J. Bents. “High Temperature Solid Oxide Regenerative Fuel Cell for Solar Photovoltaic Energy Storage”. *22nd Intersoc. Energy Convers. Eng. Conf.* 1987.

[161] J. J. Romm. *The Hype about Hydrogen: Fact and Fiction in the Race to Save the Climate*. Island Press, 2004.

[162] O. A. Marina, L. R. Pederson, M. C. Williams, G. W. Coffey, K. D. Meinhardt, C. D. Nguyen, and E. C. Thomsen. “Electrode Performance in Reversible Solid Oxide Fuel Cells”. *J. Electrochem. Soc.* 154 (2007), B452–B457.

[163] J. S. Herring, J. E. O’Brien, C. M. Stoots, G. L. Hawkes, J. J. Hartvigsen, and M. Shahnam. “Progress in high-temperature electrolysis for hydrogen production using planar SOFC technology”. *Int. J. Hydrogen Energy* 32 (2007), 440–450.

[164] G. L. Hawkes, M. Sohal, P. Torgerson, T. Armstrong, and M. C. Williams. “Development of Reversible SOFC’s for Hydrogen Production”. *ECS Trans.* The Electrochemical Society, 2008, 7–21.

[165] N. Q. Minh. “Development of Reversible Solid Oxide Fuel Cells (RSOFCs) and Stacks”. *ECS Trans.* Vol. 35. ECS, 2011, 2897–2904.

[166] H. Xu, B. Chen, J. Irvine, and M. Ni. “Modeling of CH_4-assisted SOEC for H_2O/CO_2 co-electrolysis”. *Int. J. Hydrogen Energy* 41 (2016), 21839–21849.

[167] M. Ni, M. K. H. Leung, and D. Y. C. Leung. “Electrochemical modeling of hydrogen production by proton-conducting solid oxide steam electrolyzer”. *Int. J. Hydrog. Energy Energy* 33 (2008), 4040–4047.

[168] M. Ni, M. K. H. Leung, and D. Y. C. Leung. “A modeling study on concentration overpotentials of a reversible solid oxide fuel cell”. *J. Power Sources* 163 (2006), 460–466.

[169] C. H. Wendel and R. J. Braun. “Design and techno-economic analysis of high efficiency reversible solid oxide cell systems for distributed energy storage”. *Appl. Energy* 172 (2016), 118–131.

[170] Z. Zhang, J. Zhou, Z. Zong, Q. Chen, P. Zhang, and K. Wu. “Development and modelling of a novel electricity-hydrogen energy system based on reversible solid oxide cells and power to gas technology”. *Int. J. Hydrogen Energy* 44 (2019), 28305–28315.

[171] C. H. Wendel, P. Kazempoor, and R. J. Braun. “A thermodynamic approach for selecting operating conditions in the design of reversible solid oxide cell energy systems”. *J. Power Sources* 301 (2016), 93–104.

[172] Y. Chen, Y. Luo, Y. Shi, and N. Cai. “Theoretical modeling of a pressurized tubular reversible solid oxide cell for methane production by co-electrolysis”. *Appl. Energy* 268 (2020), 114927.

[173] G. Butera, S. H. Jensen, and L. R. Clausen. “A novel system for large-scale storage of electricity as synthetic natural gas using reversible pressurized solid oxide cells”. *Energy* 166 (2019), 738–754.

[174] L. Wang, M. Pérez-Fortes, H. Madi, S. Diethelm, J. V. Herle, and F. Maréchal. “Optimal design of solid-oxide electrolyzer based power-to-methane systems: A comprehensive comparison between steam electrolysis and co-electrolysis”. *Appl. Energy* 211 (2018), 1060–1079.

[175] G. Buffo, D. Ferrero, M. Santarelli, and A. Lanzini. “Energy and environmental analysis of a flexible Power-to-X plant based on Reversible Solid Oxide Cells (rSOCs) for an urban district”. *J. Energy Storage* 29 (2020), 101314.

[176] L. Blum, L. G. De Haart, J. Malzbender, N. H. Menzler, J. Remmel, and R. Steinberger-Wilckens. “Recent results in Jülich solid oxide fuel cell technology development”. *J. Power Sources* 241 (2013), 477–485.

[177] J. Schefold, A. Brisse, A. Surrey, and C. Walter. “80,000 current on/off cycles in a one year long steam electrolysis test with a solid oxide cell”. *Int. J. Hydrogen Energy* 45 (2020), 5143–5154.

[178] F. Petipas, Q. Fu, A. Brisse, and C. Bouallou. “Transient operation of a solid oxide electrolysis cell”. *Int. J. Hydrogen Energy* 38 (2013), 2957–2964.

[179] O. Schmidt, A. Gambhir, I. Staffell, A. Hawkes, J. Nelson, and S. Few. “Future cost and performance of water electrolysis: An expert elicitation study”. *Int. J. Hydrogen Energy* 42 (2017), 30470–30492.

[180] M. Z. Khan, R. H. Song, S. B. Lee, J. W. Lee, T. H. Lim, and S. J. Park. “Effect of GDC interlayer on the degradation of solid oxide fuel cell cathode during accelerated current load cycling”. *Int. J. Hydrogen Energy* 39 (2014), 20799–20805.

[181] V. N. Nguyen, Q. Fang, U. Packbier, and L. Blum. “Long-term tests of a Julich planar short stack with reversible solid oxide cells in both fuel cell and electrolysis modes”. *Int. J. Hydrogen Energy* 38 (2013), 4281–4290.

[182] T. H. Shin, J. H. Myung, K. M. Naeem, C. Savaniu, and J. T. S. Irvine. “Ce(Mn,Fe)O_2-(La,Sr)(Fe,Mn)O_3 composite as an active cathode for electrochemical reduction of CO_2 in proton conducting solid oxide cells”. *Solid State Ionics* 275 (2015), 106–109.

[183] M. Hubert, J. Laurencin, P. Cloetens, B. Morel, D. Montinaro, and F. Lefebvre-Joud. “Impact of Nickel agglomeration on Solid Oxide Cell operated in fuel cell and electrolysis modes”. *J. Power Sources* 397 (2018), 240–251.

[184] A. Faes, A. Hessler-Wyser, D. Presvytes, C. G. Vayenas, and J. Vanherle. “Nickel-zirconia anode degradation and triple phase boundary quantification from microstructural analysis”. *Fuel Cells* 9 (2009), 841–851.

[185] S. Nuggehalli Sampathkumar, P. Aubin, K. Couturier, X. Sun, B. R. Sudireddy, S. Diethelm, M. Pérez-Fortes, and J. Van herle. “Degradation study of a reversible solid oxide cell (rSOC) short stack using distribution of relaxation times (DRT) analysis”. *Int. J. Hydrogen Energy* 47 (2022), 10175–10193.

[186] E. Tang, M. Richards, and R. Petri. *Advanced Materials for RSOFC Dual Operation with Low Degradation*. Tech. rep. 2012.

[187] M. Instruments. *Mastersizer 2000 User Manual*. Tech. rep. 2007.

[188] N. M. Mcdonald. “The Manufacturing and Testing of Anode Supported Ni10Sc1CeSZ SOFCs For Intermediate Temperature Operation”. PhD thesis. University of Birmingham, 2017.

[189] E. Ivers-Tiffée and A. Weber. “Evaluation of electrochemical impedance spectra by the distribution of relaxation times”. *J. Ceram. Soc. Japan* 125 (2017), 193–201.

[190] Y.-S. Yoo, M. Choi, J.-H. Hwang, H.-N. Im, B. Singh, and S.-J. Song. “La_2NiO_4 as oxygen electrode in reversible solid oxide cells”. *Ceram. Int.* 41 (2015), 6448–6454.

[191] M. Schönleber, D. Klotz, and E. Ivers-Tiffée. “A Method for Improving the Robustness of linear Kramers-Kronig Validity Tests”. *Electrochim. Acta* 131 (2014), 20–27.

[192] T. H. Wan, M. Saccoccio, C. Chen, and F. Ciucci. “Influence of the Discretization Methods on the Distribution of Relaxation Times Deconvolution: Implementing Radial Basis Functions with DRTtools”. *Electrochim. Acta* 184 (2015), 483–499.

[193] V. Wilde, H. Störmer, J. Szász, F. Wankmüller, E. Ivers-Tiffée, and D. Gerthsen. “$Gd_{0.2}Ce_{0.8}O_2$ Diffusion Barrier Layer between $(La_{0.58}Sr_{0.4})(Co_{0.2}Fe_{0.8})O_{3-\delta}$ Cathode and $Y_{0.16}Zr_{0.84}O_2$ Electrolyte for Solid Oxide Fuel Cells: Effect of Barrier Layer Sintering Temperature on Microstructure”. *ACS Appl. Energy Mater.* 1 (2018), 6790–6800.

[194] R. N. Basu, A. D. Sharma, A. Dutta, and J. Mukhopadhyay. “Processing of high-performance anode-supported planar solid oxide fuel cell”. *Int. J. Hydrogen Energy* 33 (2008), 5748–5754.

[195] A. Escardino, A. Belda, M. J. Orts, and A. Gozalbo. “Ceria-doped scandia-stabilized zirconia ($10Sc_2O_3{\cdot}1CeO_2{\cdot}89\ ZrO_2$) as electrolyte for SOFCs: Sintering and ionic conductivity of thin, flat sheets”. *Int. J. Appl. Ceram. Technol.* 14 (2017), 532–542.

[196] X. Lu, O. O. Taiwo, A. Bertei, T. Li, K. Li, D. J. Brett, and P. R. Shearing. "Multi-length scale tomography for the determination and optimization of the effective microstructural properties in novel hierarchical solid oxide fuel cell anodes". *J. Power Sources* 367 (2017), 177–186.

[197] N. H. Menzler, F. Tietz, S. Uhlenbruck, H. Peter Buchkremer, and D. Stöver. "Materials and manufacturing technologies for solid oxide fuel cells". *J. Mater. Sci.* 45 (2010), 3109–3135.

[198] F. Wang, M. Nishi, M. E. Brito, H. Kishimoto, K. Yamaji, H. Yokokawa, and T. Horita. "Sr and Zr diffusion in LSCF/10GDC/8YSZ triplets for solid oxide fuel cells (SOFCs)". *J. Power Sources* 258 (2014), 281–289.

[199] J.-H. Song, M. G. Jung, H. W. Park, and H.-T. Lim. "The Effect of Fabrication Conditions for GDC Buffer Layer on Electrochemical Performance of Solid Oxide Fuel Cells". *Nano-Micro Lett.* 5 (2013), 151–158.

[200] P. Coddet, M.-L. Amany, J. Vulliet, A. Caillard, and A.-L. Thomann. "YSZ/GDC bilayer and gradient barrier layers deposited by reactive magnetron sputtering for solid oxide cells". *Surf. Coatings Technol.* 357 (2019), 103–113.

[201] A. Tsoga, A. Gupta, A. Naoumidis, and P. Nikolopoulos. "Gadolinia-doped ceria and yttria stabilized zirconia interfaces: Regarding their application for SOFC technology". *Acta Mater.* 48 (2000), 4709–4714.

[202] J. Szász, F. Wankmüller, V. Wilde, H. Störmer, D. Gerthsen, N. H. Menzler, and E. Ivers-Tiffée. "Nature and Functionality of $La_{0.58}Sr_{0.4}Co_{0.2}Fe_{0.8}O_{3-\delta}$/ $Gd_{0.2}Ce_{0.8}O_{2-\delta}$/$Y_{0.16}Zr_{0.84}O_{2-\delta}$ Interfaces in SOFCs". *J. Electrochem. Soc.* 165 (2018), F898–F906.

[203] A. Leonide. "SOFC Modelling and Parameter Identification by means of Impedance Spectroscopy". PhD thesis. Univeristy Karlsruhe, 2010.

[204] A. Leonide, V. Sonn, A. Weber, and E. Ivers-Tiffée. "Evaluation and Modeling of the Cell Resistance in Anode-Supported Solid Oxide Fuel Cells". *J. Electrochem. Soc* 155 (2008), B36–B41.

[205] D. Papurello, D. Menichini, and A. Lanzini. "Distributed relaxation times technique for the determination of fuel cell losses with an equivalent circuit model to identify physicochemical processes". *Electrochim. Acta* 258 (2017), 98–109.

[206] H. Schichlein, A. C. Müller, M. Voigts, A. Krügel, and E. Ivers-Tiffé. "Deconvolution of electrochemical impedance spectra for the identification of electrode reaction mechanisms in solid oxide fuel cells". *J. Appl. Electrochem.* 32 (2002), 875–882.

[207] T. Jacobsen, P. V. Hendriksen, and S. Koch. "Diffusion and conversion impedance in solid oxide fuel cells". *Electrochim. Acta* 53 (2008), 7500–7508.

[208] J. Mermelstein, M. Millan, and N. Brandon. “The impact of steam and current density on carbon formation from biomass gasification tar on Ni/YSZ, and Ni/CGO solid oxide fuel cell anodes”. *J. Power Sources* 195 (2010), 1657–1666.

[209] K. Ke, A. Gunji, H. Mori, S. Tsuchida, H. Takahashi, K. Ukai, Y. Mizutani, H. Sumi, M. Yokoyama, and K. Waki. “Effect of oxide on carbon deposition behavior of CH_4 fuel on Ni/ScSZ cermet anode in high temperature SOFCs”. *Solid State Ionics* 177 (2006), 541–547.

[210] J. H. Koh, B. S. Kang, H. C. Lim, and Y. S. Yoo. “Thermodynamic analysis of carbon deposition and electrochemical oxidation of methane for SOFC anodes”. *Electrochem. Solid-State Lett.* 4 (2001), A12–A15.

[211] NASA Glenn Research Centre. *Chemical Equilibrium with Applications (CEARUN)*. URL: https://cearun.grc.nasa.gov/.

[212] C. W. Bale, E. Bélisle, P. Chartrand, S. A. Decterov, G. Eriksson, A. E. Gheribi, K. Hack, I. H. Jung, Y. B. Kang, J. Melançon, A. D. Pelton, S. Petersen, C. Robelin, J. Sangster, P. Spencer, and M. A. Van Ende. “FactSage thermochemical software and databases, 2010–2016”. *Calphad* 54 (2016), 35–53.

[213] C. Fu, S. H. Chan, Q. Liu, X. Ge, and G. Pasciak. “Fabrication and evaluation of Ni-GDC composite anode prepared by aqueous-based tape casting method for low-temperature solid oxide fuel cell”. *Int. J. Hydrogen Energy* 35 (2010), 301–307.

[214] D. R. Bhosale and S. I. Patil. “Conduction pathways and mixed ionic-electronic conductivity below 500ºC in $Ca_xY_{3-x}Fe_5O_{12-\delta}$ materials”. *Phys. Rev. Mater.* 3 (2019), 095007.

[215] X. Sun, M. Chen, S. H. Jensen, S. D. Ebbesen, C. Graves, and M. Mogensen. “Thermodynamic analysis of synthetic hydrocarbon fuel production in pressurized solid oxide electrolysis cells”. *Int. J. Hydrogen Energy* 37 (2012), 17101–17110.

[216] M. Lo Faro, S. C. Zignani, S. Trocino, V. Antonucci, and A. S. Aricò. “New insights on the co-electrolysis of CO_2 and H_2O through a solid oxide electrolyser operating at intermediate temperatures”. *Electrochim. Acta* 296 (2019), 458–464.

[217] T. L. Skafte, C. Graves, P. Blennow, and J. Hjelm. “Carbon Deposition during CO_2 Electrolysis in Ni-Based Solid-Oxide-Cell Electrodes”. *ECS Trans.* 68 (2015), 3429–3437.

[218] T. Chen, W. G. Wang, H. Miao, T. Li, and C. Xu. “Evaluation of carbon deposition behavior on the nickel/yttrium-stabilized zirconia anode-supported fuel cell fueled with simulated syngas”. *J. Power Sources* 196 (2011), 2461–2468.

[219] Y. Lin, Z. Zhan, J. Liu, and S. A. Barnett. “Direct operation of solid oxide fuel cells with methane fuel”. *Solid State Ionics* 176 (2005), 1827–1835.

[220] J.-H. Koh, Y.-S. Yoo, J.-W. Park, and H. C. Lim. “Carbon deposition and cell performance of Ni-YSZ anode support SOFC with methane fuel”. *Solid State Ionics* 149 (2002), 157–166.

[221] A. Lanzini, P. Leone, C. Guerra, F. Smeacetto, N. P. Brandon, and M. Santarelli. “Durability of anode supported Solid Oxides Fuel Cells (SOFC) under direct dry-reforming of methane”. *Chem. Eng. J.* 220 (2013), 254–263.

[222] A. L. Snowdon, Z. Jiang, and R. Steinberger-Wilckens. “Five-layer reverse tape casting of IT-SOFC”. *Int. J. Appl. Ceram. Technol.* 19 (2021), 289–298.